ELECTROSPRAY PROPULSION ENGINEERING TOOLKIT, ESPET 1.0

Underlying Theory and Basis of Confidence

Prepared by:

Rainer A. Dressler and Benjamin St. Peter
4 Fourth Avenue
Burlington, MA 01803

ESPET was Developed for:
National Aeronautics and Space Administration
NASA Glenn Research Center
21000 Brook Park Road
Cleveland, OH 44135-6000

Under Contract No. NNX16CC23C

October 2018

TABLE OF CONTENTS

ACKNOWLEDGMENTS

The authors acknowledge the excellent guidance by Dr. John Yim of the NASA Glenn Research Center. His oversight was critical in allowing ESPET to exceed the original objectives. The authors would also like to acknowledge SSI scientists Jason Quenneville and Megan Stark, SSI interns Jessica Cashman and Cameron Braunstein, Busek researchers Yu-hui Chiu, Timothy Fedkiw, Lauren Rand and Daniel Courtney, and CFD Research Corporation scientists Yi Wang and Hongjun Son for their valuable technical contributions during the course of this Phase II. The authors are also deeply indebted to Prof. Paulo Lozano of the MIT Space Propulsion Laboratory for sharing his expertise during many fruitful discussions and for his enthusiastic encouragement.

1. INTRODUCTION

High precision, high efficiency propulsion is a critical enabling technology for future space exploration missions, particularly for miniaturized spacecraft such as CubeSats. Micro-electric propulsion technologies are sought for low to high specific impulse (I_{sp}), low-thrust operations such as attitude control, precision positioning, and orbital maintenance. Electrospray propulsion (ESP) is arguably the most promising form of micro-electric propulsion. ESP uses a liquid propellant, thereby eliminating the need for bulky gas tanks. In ESP emitters, charges are extracted and accelerated with high electric fields from the liquid surface of a non-volatile, conducting liquid such as an ionic liquid (IL) or a liquid metal (LM). Because this approach does not require a discharge, ESP systems are inherently efficient and do not lose efficiency upon miniaturization, unlike plasma-based electric propulsion (EP) designs.

The main drawbacks of ESP are the low thrust (< 1 μN for high I_{sp} mode) and high mass per emitter. Consequently, extensive development has been dedicated to scaling up ESP systems to large, high density arrays of ESP emitters that can match the thrust of other EP systems. Through proper fabrication and integration technologies, the new ESP systems will offer substantial mass and volume savings. However, these developments are hampered by the complex microfluidics associated with the vast parameter space that has to be controlled in order to produce a reliable propulsion system with desired thrust, specific impulse, efficiency (electrical and propellant utilization), uniformity, and stability. Currently, ESP system development relies on an iterative approach, which includes costly build and test cycles to settle on a design. This results in long development times. Physics-based models are sought to accurately predict the performance of microfluidic ESP designs to reduce the development time and to improve system capabilities.

The *Electrospray Propulsion Engineering Toolkit (ESPET)* was designed to accelerate the development of ESP emitter array systems with practical thrust levels and high thrust densities. ESPET is *a multi-scale model that extends experimental and detailed high-level physics characterization of microfluidic and electrohydrodynamic components to full-scale ESP microfluidic network performance.* The physics underlying a microfluidic network of an ESP system covers multiple length scales that render the application of high-level computational fluid dynamics (CFD) or atomistic molecular dynamics (MD) simulations over the entire system impractical. ESPET takes an engineering model approach that breaks the ESP system down into multiple microfluidic components or domains that can be described by analytical microfluidic solutions and specific parameters of the domain.

Figure 1.1 provides an overview flow chart of ESPET, which consists of a microfluidics database, a domain modeler, and a network solver which produces the system performance outputs. Two options of network solver are provided. In the first, complex networks are solved using the Ohm’s Law – Hagen-Poiseuille analogy. We use the well known and freely available SPICE electric circuit solver where micro-fluidic components produced by the domain modeler are loaded and “wired” to others. For simple networks consisting of a reservoir, a feed system and an emitter, we offer a simpler QuickSolver, which has the added advantage of instantly being able to analyze the temperature dependence of the performance.

Our domain or component-based approach allows the combination of modeling and laboratory experiments where domain-specific empirical models are developed which are parameterized and validated by high-level physics calculations or laboratory experiments. The domain models rely on a microfluidics properties database consisting of existing propellant, substrate, and interfacial properties, as well as new parameters determined from laboratory experiments. The ESP system domain models consist of analytical microfluidic solutions of the Navier-Stokes equations, or parametric expressions developed with the help of laboratory experiments. When necessary, numerical models incorporating high-level physics can be implemented.

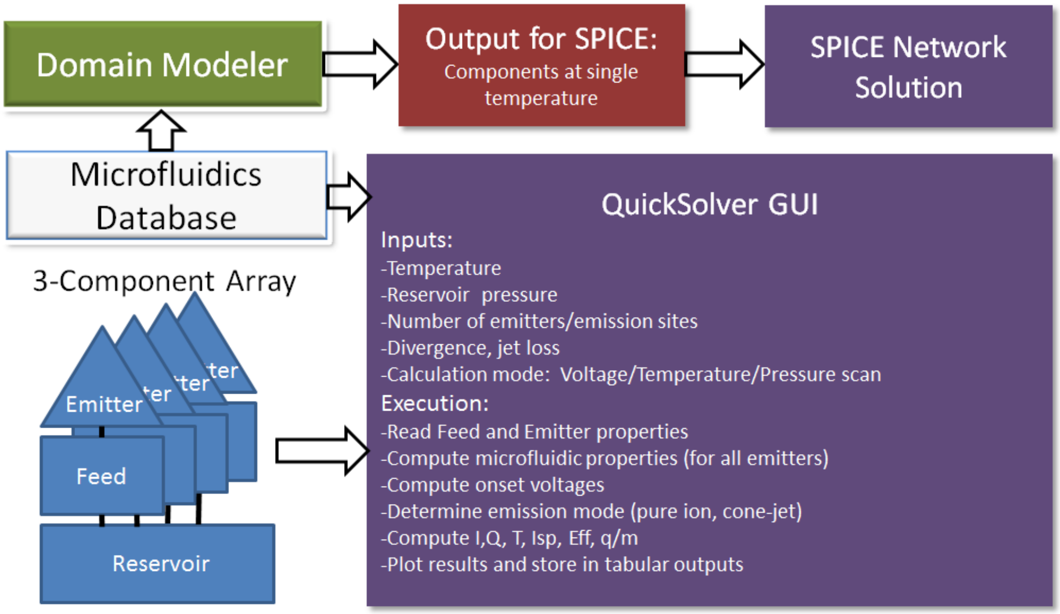

Figure 1.1 Simple ESPET flow chart with the primary software components and two network solution options.

ESPET has a user interface allowing straightforward setup of a network of microfluidic components, the assignment of properties to the individual components, and the derivation of the solution for the flow and charged spray properties of the network. The ultimate utility and accuracy of ESPET depends on user input, especially in building the database, parameterizing specific domain models, and testing the prototype software. For this and further validation purposes, SSI developed ESPET into a web app for use by ESP system developers, accessible at espet.spectral.com.

The current version of ESPET was developed at a time where there were still many gaps in our understanding of the electrospray physics. For example, a unified theory on the transition from a cone-jet configuration to a pure-ionic regime (PIR) for dielectric propellants does not yet exist. Similarly, no theory had been reported on modeling the spray from multiple emission sites in porous emitter cones, a highly promising emitter type for both dielectric and liquid metal propellants. We, therefore, had to rely on developing simple empirical expressions that matched selected experimental data retrieved from the literature, or from measurements at Busek Co. under subcontract for ESPET development. Our primary goal was to develop a platform as applicable to as many emitter designs and propellant types as possible. The software is design in such a way that upgrades to models or the addition of microfluidic properties are straightforward. We encourage the ESP development community to contact us with new data or models. We hope to assist users in integrating their contributions, which will be acknowledged in the extended ESPET metadata.

This manual/basis of confidence document is organized in the following manner. In Section 2, we describe the individual components and their underlying structure and theory. In many instances, the theory requires unknown adjustable parameters. Recommended values for these parameters are provided in Section 3, where we benchmark ESPET against laboratory data. QuickSolver input configurations for the tests in Section 3 can be accessed from the QuickSolver application. The quickest way to get up to speed using ESPET is to find a test example that most closely applies to a user's configuration of interest, loading the example configuration file, and examining the inputs that provided the favorable comparison to experiment.

2. ESPET 1.0 COMPONENTS AND UNDERLYING THEORY

2.1 Microfluidics Database

The structure of the Microfluidics Properties Database is shown in Figure 2.1. It consists of three linked databases for propellants, substrates and interfacial properties, the latter linking specific propellants and substrates. Currently, the primary interfacial property of consideration is the contact angle governing the liquid-substrate wetting. In addition, we have considered the effective pore size of a porous medium to be an interfacial property, although literature data suggests that it is purely a property of the medium. detailing the database development.

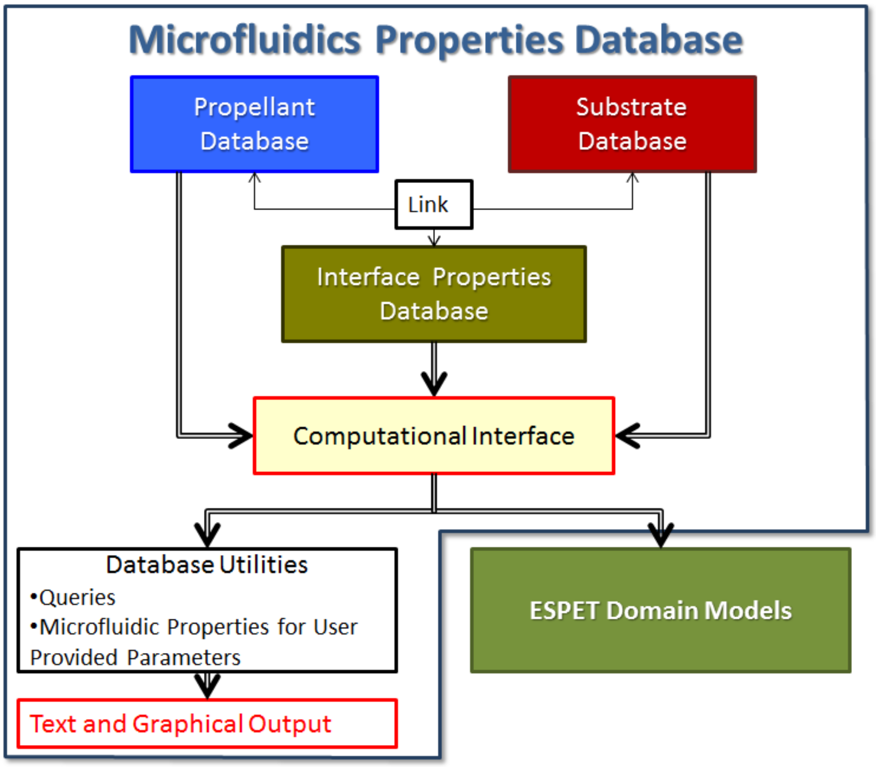

Figure 2.1. ESPET microfluidics database structure and connection to ESPET domain modeler

There are two types of propellants actively considered for ESP system development, room-temperature ionic liquids (ILs), and liquid metals (LMs). Our literature search focused on retrieving microfluidic properties of common ILs and LMs, as well as common substrates used in ESP system development. Critical was the inclusion of data for the temperature dependence of density, surface tension, viscosity, vapor pressure and conductivity. Particularly for ILs, the viscosity and conductivity can be highly temperature dependent. Table 2.1 lists the ESPET propellants for which we found literature data. For each propellant, we list references for the adopted properties. For temperature-dependent properties we derived polynomials that reflect the temperature dependent values within a valid range of temperatures. The literature references are also provided in the database metadata.

Table 2.1 Microfluidic properties references for propellants in ESPET database.

Propellant	References
Ionic Liquids:	
EMI-TFSI	[*Fröba, et al.*, 2008; *Umecky, et al.*, 2009; *Zaitsau, et al.*, 2006; *Zhang, et al.*, 2006]
EMI-BF4	[*Kolbeck, et al.*, 2010; *McEwen, et al.*, 1999; *Umecky, et al.*, 2009; *Wakai, et al.*, 2005; *Xu, et al.*, 2012; *Zhang, et al.*, 2006]
EMI-GaCl$_4$	[*Perez-Martinez*, 2016; *Yang, et al.*, 2006]
Liquid Metals:	
Indium	[*Cusack*, 1963; *Keene*, 1993; *Strauss*, 1962; *Williams and Miller*, 1950]
Gallium	[*Cusack*, 1963; *Hardy*, 1985; *Strauss*, 1962]
Caesium	[*Cusack*, 1963; *Keene*, 1993; *Lu and Jiang*, 2005; *Strauss*, 1962]

Table 2.2 lists the substrates included in the database for which interfacial properties are available for at least one propellant. The materials are either porous or "channel" conduits. Several of the materials have been characterized with respect to EMI-TFSI and EMI-BF4 wetting properties by Dandavino and coworkers [*Dandavino, et al.*, 2011]. This work did not identify significant differences between contact angles measured in a vacuum and in atmospheric pressure air. The sintered bososilicate glass designations, P0, P1, … are Robu & Schott, ISO 4793 pore size standards.

Table 2.2. List of substrates in the ESPET microfluidics database.

Substrate	Type	Description
Stainless Steel Fibermat	Porous	Metallic fiber filter
Silicon	Channel	Oxidized silicon
Borosilicate Glass	Channel	Borosilicate Glass Channel
Tungsten	Porous	
Rhenium	Porous	
Borosilicate Glass P0	Porous	Sintered porous glass
Borosilicate Glass P1	Porous	Sintered porous glass
Borosilicate Glass P2	Porous	Sintered porous glass
Borosilicate Glass P3	Porous	Sintered porous glass
Borosilicate Glass P4	Porous	Sintered porous glass
Borosilicate Glass P5	Porous	Sintered porous glass
Borosilicate Glass Fibermat	Porous	Glass fiber filter
Xerogel 1	Porous	Carbon Xerogel
Gold	Channel	
Platinum	Channel	
Aluminum	Channel	

The ESPET database software is comprised of a SQL database and a Propellant Viewer graphical user interface (GUI). Figure 2.2 shows a screen shot of the Propellant Viewer. It is set up to display a selected property over a specified temperature range for a selection of propellants specified by three filters, Type, Date and Melting Temperature (K). A bar chart is displayed if the property is not temperature-dependent or if only one temperature has been entered. The charts are interactive, allowing the operator to hover the cursor to see the precise value and to toggle plots by clicking on the legend. If no filtering is necessary, the operator can vacate the rightmost column of the Filter section or simply keep the defaults. A text area on the page is updated with available metadata in the database for the particular field and propellant(s). At the bottom of the page, there are links for downloading the current chart data in tabular format, the database in Excel format, and the SQL database itself.

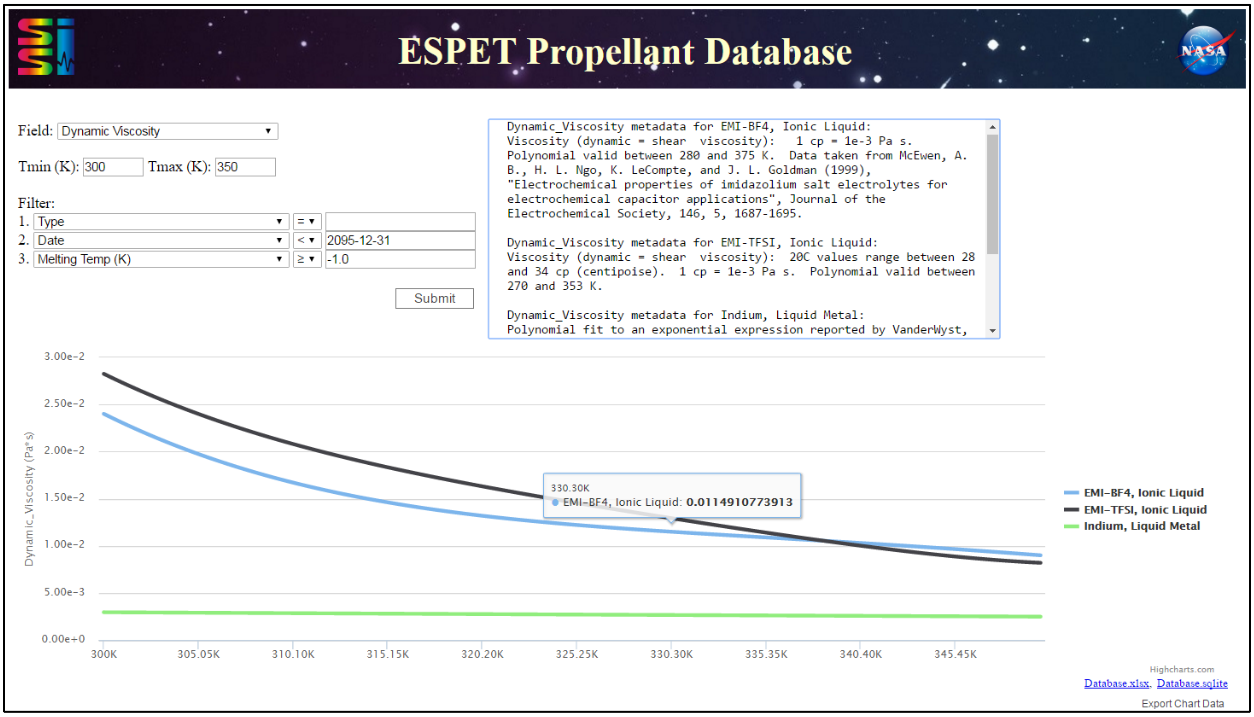

Field: Dynamic Viscosity

Tmin (K): 300 Tmax (K): 350

Filter:
1. Type =
2. Date < 2095-12-31
3. Melting Temp (K) ≥ -1.0

```
Dynamic_Viscosity metadata for EMI-BF4, Ionic Liquid:
Viscosity (dynamic = shear  viscosity):   1 cp = 1e-3 Pa s.
Polynomial valid between 280 and 375 K.  Data taken from McEwen, A.
B., H. L. Ngo, K. LeCompte, and J. L. Goldman (1999),
"Electrochemical properties of imidazolium salt electrolytes for
electrochemical capacitor applications", Journal of the
Electrochemical Society, 146, 5, 1687-1695.

Dynamic_Viscosity metadata for EMI-TFSI, Ionic Liquid:
Viscosity (dynamic = shear  viscosity):  20C values range between 28
and 34 cp (centipoise).  1 cp = 1e-3 Pa s.  Polynomial valid between
270 and 353 K.

Dynamic_Viscosity metadata for Indium, Liquid Metal:
Polynomial fit to an exponential expression reported by VanderWyst,
```

```
330.30K
● EMI–BF4, Ionic Liquid: 0.0114910773913
```

Figure 2.2. Propellant Database screenshot.

At the core of our tool is the SQL database itself, implemented in SQLite. This database has seven tables for substrates, propellants, interfaces, metadata and units. The substrate table is uniquely keyed by the combination of two fields, *Material* (e.g. silicon) and *Type* (channel or porous). The substrate properties are listed in Table 2.3.

Table 2.3. Fields of the substrate database table.

Density
Conductivity
Porosity
Roughness
Relative_Permittivity

Like the substrate table, the propellant table is also uniquely keyed by *Material* (e.g. EMI-TFSI) and *Type* (ionic liquid or liquid metal). Fields include the properties listed in Table 2.4. All temperature-dependent properties are stored as coefficients of a 5th-order polynomial. The interface table is keyed by unique pairings of the propellant and substrate keys. For example, one key is the combination of non-porous (solid) borosilicate glass with the EMI-BF4 ionic liquid. Interface properties include the contact angle and effective pore size.

There are three metadata tables, one for each of the substrate, propellant and interface tables. It is possible to enter metadata independently for each property of each key. For consistency across the application, the units (e.g. kJ/mol for dissociation energy) are consolidated into a single table.

Finally, we have written code for converting an Excel workbook to a SQLite database, where each worksheet corresponds to one of the database tables. This code also overwrites a configuration file which controls how certain options will be greyed-out in the user interface, among other things. This conversion tool makes it easy to manage both the database and the web application.

Table 2.4. Fields of the propellant database table with temperature-dependent fields in grey.

Molecular_Mass
Melting_Temp
Decomposition_Temp
Mobility
Electrochem_Window
Cathode_Limit
Anode_Limit
Dissociation_Energy
Monomer_Cation_Solvation_Energy
Monomer_Anion_Solvation_Energy
Dimer_Cation_Solvation_Energy
Dimer_Anion_Solvation_Energy
Density
Dynamic_Viscosity
Surface_Tension
Conductivity
Relative_Permittivity
Vapor_Pressure

.

Figures 2.3-2.5 show screen shots of ESPET database charts for the temperature dependence of the liquid metal viscosity, surface tension and vapor pressure. The outputs are controlled by the SQL filter 'Type = Liquid Metal'. The comparison between surface tension and vapor pressure demonstrates the close relationship between vapor pressure, heat of vaporization and surface tension. Since cesium has a low surface tension, it is more prone to evaporation.

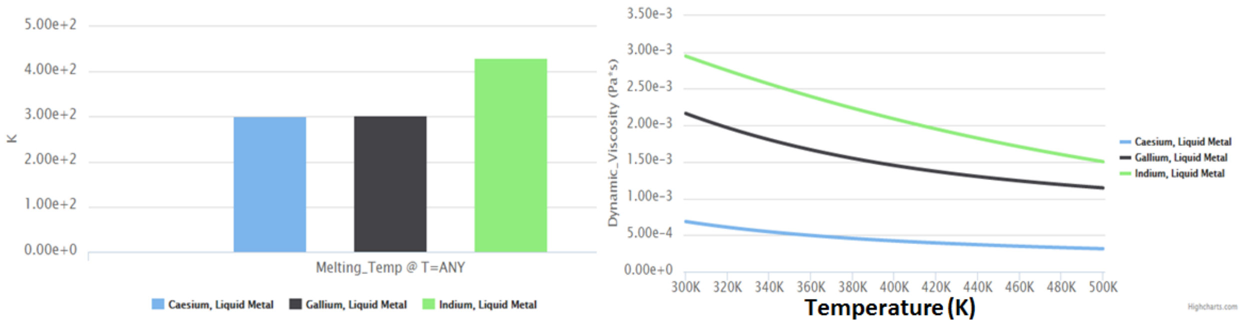

Figure 2.3. ESPET charts produced for liquid metal melting points (left chart) and dynamic viscosity (viscosity). Data are only valid above respective melting temperatures.

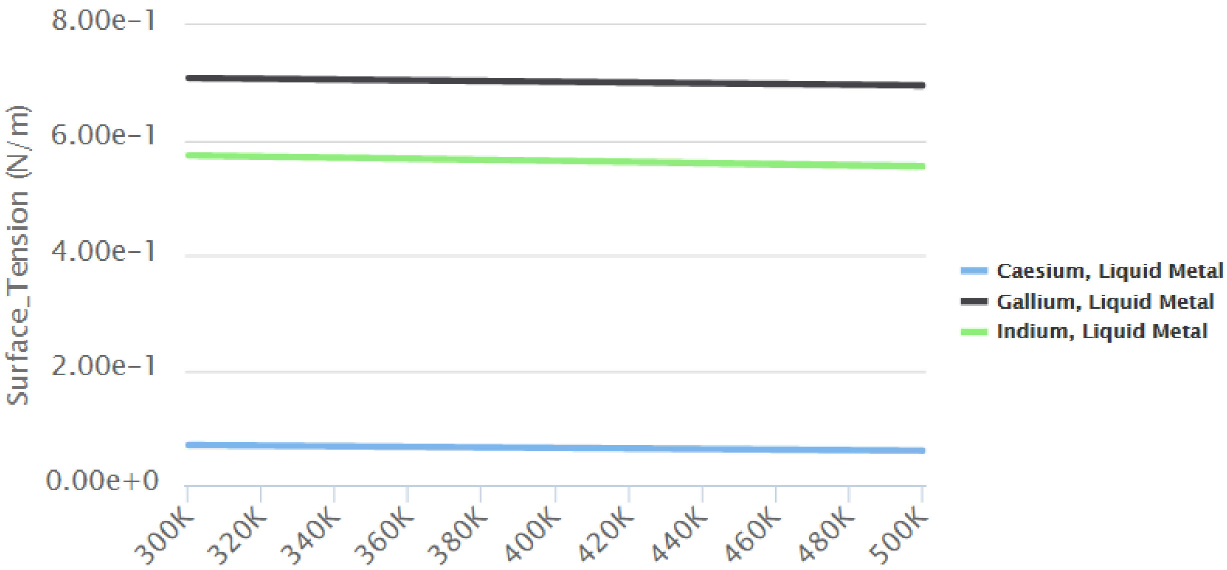

Figure 2.4. Surface tension versus temperature for liquid metals in the database. Data are only valid above respective melting temperatures (see Figure 2.3).

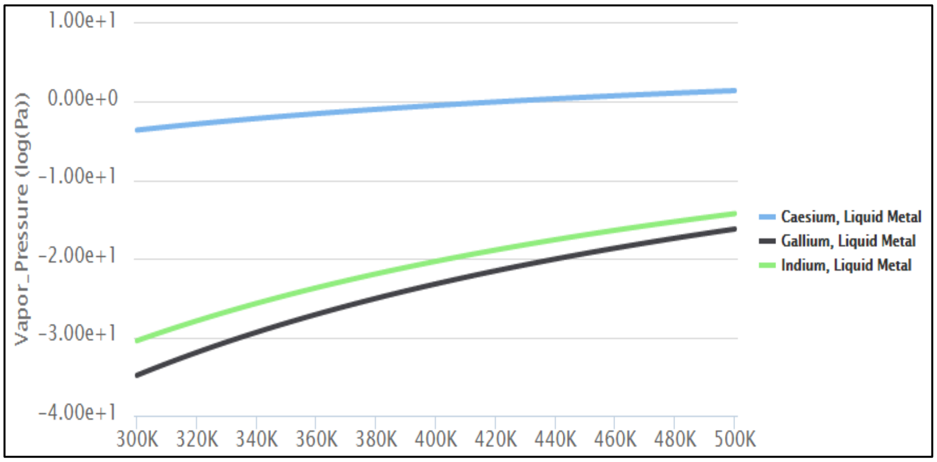

Figure 2.5. Vapor pressure (log10p) versus temperature for liquid metals in the database. Data are only valid above respective melting temperatures (see Figure 2.3).

2.2 Domain Modeler

Figure 2.6 shows a flow chart of how the domain models are organized and integrated in ESPET. The domain models are divided into feed system and emitter models. The feed system models are generally viscous flow models of specific conduits consisting of analytical solutions to the Navier Stokes equations. The models are setup so that Navier Stokes solvers or reduced-order models can readily be introduced to the code base. The emitter models consist of electrohydrodynamic Taylor Cone physics models. Currently, we have implemented analytical expressions and parametric models obeying known scaling laws.

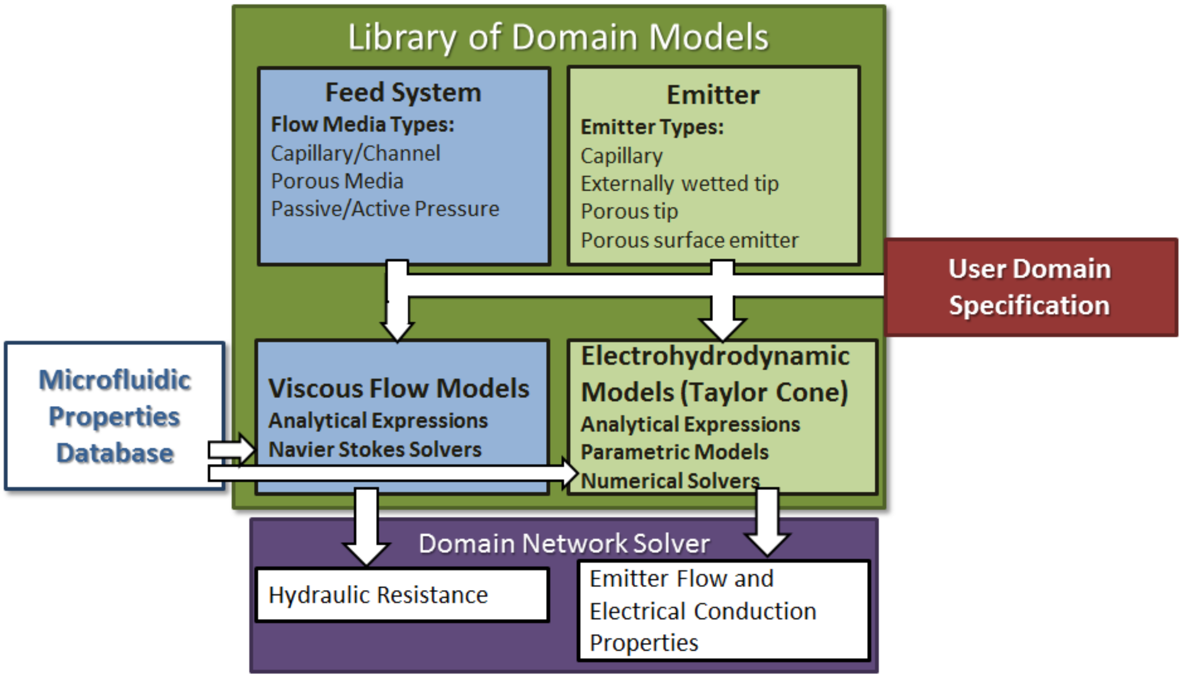

Figure 2.6. Flow chart of domain model library and its connection to other ESPET components.

2.2.1 Viscous Flow

2.2.1.1 <u>Overview</u>

A summary of viscous flow analytical expressions derived from the Navier-Stokes and Darcy equations is shown in Table 2.5. The most important property of a feed channel for ESPET is its hydraulic resistance, which will depend on the viscosity of the propellant, which itself depends on the temperature. The expressions in Table 2.5 apply to closed channels most of which have been retrieved from the excellent text by Bruus [*Bruus*, 2007]. Open channels or grooves are treated in a first approximation as having a hydraulic resistance that is twice that of the corresponding closed channel.

When filling a microfluidic network with propellant, the Laplace or capillary force pressure is important. For non-porous media (channels), the contact angle, retrieved from the interfacial properties database, is of importance in addition to the surface tension. For porous media, the Laplace pressure is given by the surface tension and effective pore size. Simple analytical expressions for wicking time of a specific conduit are also integrated in the domain model library.

Table 2.5. Viscous flow analytical expressions for cylindrical and rectangular channels, and porous media.

Property	Capillary/Channel Relations		Porous Media Relations	Definitions
	Cylindrical	Rectangular		
Hagen-Poiseuille Flow: $\Delta P = R_{hyd} Q$	$\Delta P = C\mu L Q$, $R_{hyd} = C\mu L$		$\Delta P = \frac{\mu L}{\kappa A} Q, \quad R_{hyd} = \frac{\mu L}{\kappa A}$	ΔP: Pressure drop R_{hyd}: Hydraulic resistance Q: Volume flow rate A: Porous medium area normal to flow κ: permeability
Hydraulic Resistance: $R_{hyd} = C\mu L$	$C = \frac{8}{\pi r^4}$	$C = \frac{12}{\left\{1 - 0.63(h/w)\tanh\left(\frac{\pi h}{2w}\right)\right\} h^3 w}$ $w >> h: C = \frac{12}{h^3 w}$	$C = \frac{1}{\kappa A}$ $\kappa = \frac{\phi D^2}{32}$	μ: Dynamic viscosity L: Domain length r: Channel radius h: Channel height w: Channel width ϕ: Porosity D: Effective pore size
Capillary Pressure Drop (Surface Pressure Drop)	$\Delta P = 2\gamma \cos\theta / r$	$\Delta P = 2\gamma \cos\theta \left(\frac{1}{h} + \frac{1}{w}\right)$ $w >> h: \Delta P = 2\gamma \cos\theta / h$	$\Delta P = 4\gamma / D$	θ: Contact angle γ: Surface tension
Passive Flow $\dot{m} = Q\rho$	$Q = \frac{\pi r^3}{4\mu L} \gamma \cos\theta$	$w >> h: Q = \frac{1}{6} \frac{\gamma \cos\theta h^2 w}{\mu L}$	$Q = \frac{wh}{8\mu L} \gamma D \phi$	$\dot{m}$: Mass flow ρ: Density
Wicking	$L(t) = r\sqrt{\frac{\gamma \cos\theta}{2\mu r}}\, t^{1/2}$	$w >> h: L(t) = h\sqrt{\frac{\gamma \cos\theta}{3\mu h}}\, t^{1/2}$	$L(t) = \frac{1}{2}\sqrt{\frac{\gamma D}{\mu}}\, t^{1/2}$	t: time

2.2.1.2 Thin Film Models

Externally wetted objects without grooves have significantly higher hydraulic resistances that depend strongly on the film thickness. Here we use the expressions reported by Mair [*Mair*, 1997] for a cylindrical (e.g., wire) conduit:

$$R_{hyd} = \frac{3\mu L}{2\pi r \delta^3} \tag{2.1}$$

where r is the conduit radius and δ is the film thickness. For a cone with half angle α and height H, the expression is:

$$R_{hyd} = \frac{3\mu \ln(1 + H \tan\alpha / R_c)}{2\pi \delta^3 \tan\alpha} \tag{2.2}$$

where R_c is the radius of curvature of the cone tip.

2.2.1.3 Porous Cone and Prism Model

Table 2.5 lists only expressions for axially symmetric porous conduits. The emitter structures in ESPET include porous cone and porous prism shaped edge emitters. The hydraulic resistance of a ***porous conical tip*** can be computed using the expression derived by Courtney [*Courtney*, 2006]:

$$R_{hyd} = \frac{\mu}{2\pi\kappa} \frac{1}{1 - \cos\alpha} \left[\frac{\tan\alpha}{R_c} - \frac{\cos\alpha}{h} \right], \tag{2.3}$$

where κ is the permeability of the porous medium (see Fig. 2.21). For a pillar geometry ($\alpha = 0$), the hydraulic resistance is given by the well-known expression derived from Darcy's law:

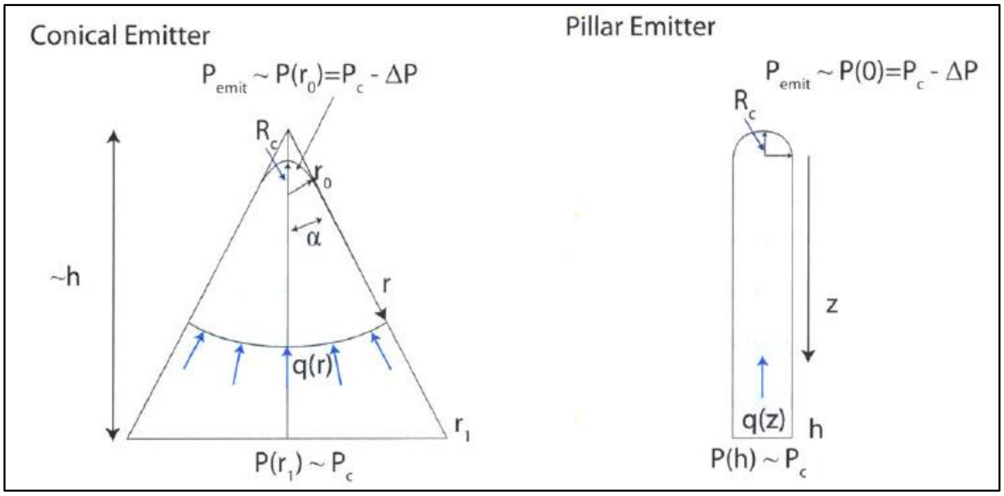

Figure 2.7. Geometric parameters of porous conical and pillar emitters (taken from Courtney [*Courtney*, 2006]).

$$R_{hyd} = \frac{\mu}{\pi R_c^2 \kappa} h \tag{2.4}$$

For a ***porous triangular or prismatic edge emitter,*** we follow the derivation of Eq. 2.3 by Courtney. Here the surface area with equal volume flow rate would be described by a cylinder surface segment, $A = sG$, where s is the circular segment subtended by 2α and G is the edge length (perpendicular to the triangular cross-section):

$$\boldsymbol{R_{hyd} = \frac{\mu}{2\alpha G\kappa} ln\left(\frac{R_c\ cos(\alpha)}{h\, tan(\alpha)}\right)} \tag{2.5}$$

This hydraulic resistance, however, assumes a uniform flow from the base of the prism structure to the edge with curvature, R_c. However, a porous edge emitter does not emit an "edge spray". The edge is the base of multiple emission sites consisting of Taylor cones. As we discuss under emitter models, the hydraulic resistance required for the computation of the microfluidics of the entire system must be associated with the flow to these individual emission sites. Thus, in much of the volume of the emitter near the edge, the flow could be significantly suppressed.

2.2.1.4 Viscous Flow Domain Model Graphical User Interface

Figure 2.8 shows a screen snapshot of the Domain Modeler for viscous flow domains. It is a web application accessed through http://espet.spectral.com/espet/domainModeler/espdm. The user selects an available conduit type (porous, external or internal), substrate material and propellant, and then sets the conduit dimensions. The domain modeler then computes desired properties for a selected temperature range. In order to compute the desired quantity, the domain modeler accesses the ESPET database. After selecting a domain, a graphic description appears with different prompts for fields including spatial dimensions, porosities, flow rates and contact angles. Whenever possible, the default values are read or calculated using the database.

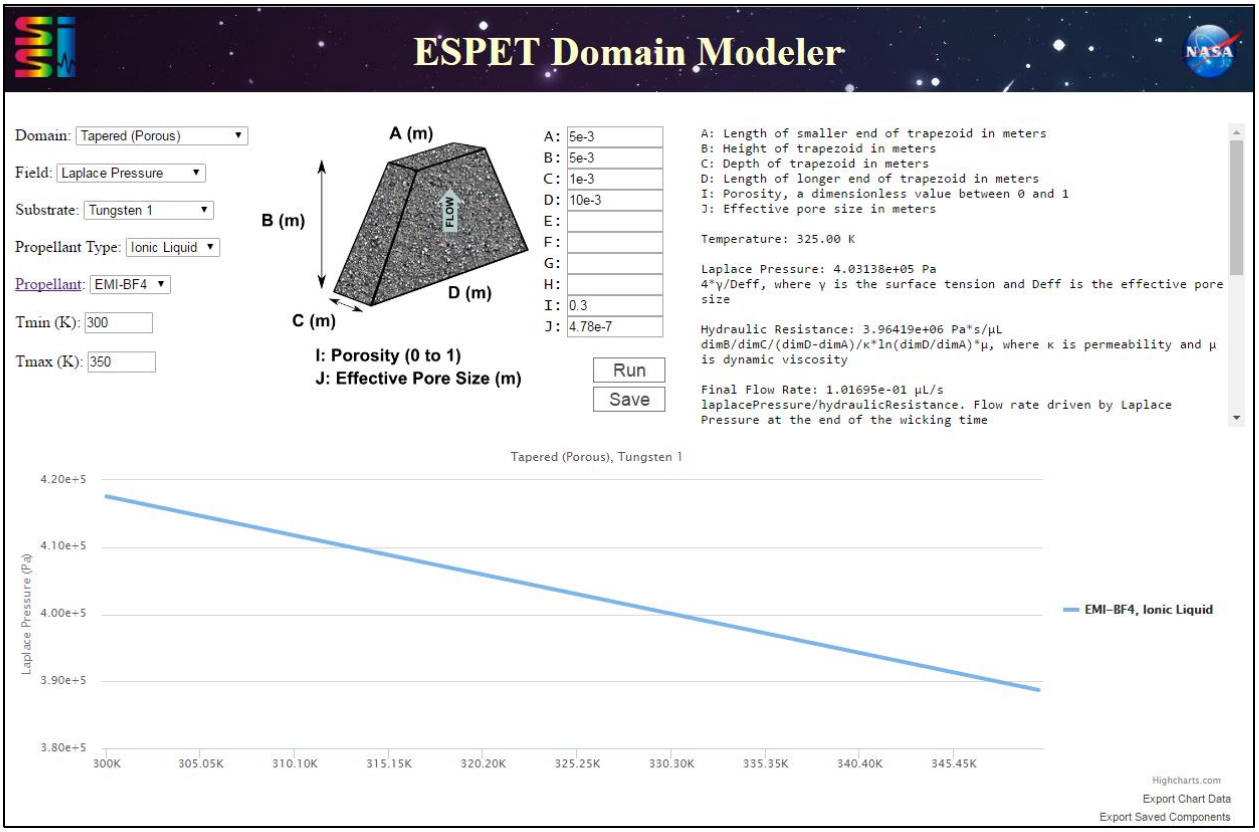

Domain: Tapered (Porous)
Field: Laplace Pressure
Substrate: Tungsten 1
Propellant Type: Ionic Liquid
Propellant: EMI-BF4
Tmin (K): 300
Tmax (K): 350

A: 5e-3
B: 5e-3
C: 1e-3
D: 10e-3
E:
F:
G:
H:
I: 0.3
J: 4.78e-7

```
A: Length of smaller end of trapezoid in meters
B: Height of trapezoid in meters
C: Depth of trapezoid in meters
D: Length of longer end of trapezoid in meters
I: Porosity, a dimensionless value between 0 and 1
J: Effective pore size in meters

Temperature: 325.00 K

Laplace Pressure: 4.03138e+05 Pa
4*γ/Deff, where γ is the surface tension and Deff is the effective pore
size

Hydraulic Resistance: 3.96419e+06 Pa*s/µL
dimB/dimC/(dimD-dimA)/κ*ln(dimD/dimA)*µ, where κ is permeability and µ
is dynamic viscosity

Final Flow Rate: 1.01695e-01 µL/s
laplacePressure/hydraulicResistance. Flow rate driven by Laplace
Pressure at the end of the wicking time
```

Figure 2.8. Domain Modeler screenshot.

Depending on the domain and the availability of information, it might not be possible to calculate certain properties. When this is the case, the operator sees those properties as greyed-out. For example, interfacial properties between silicon and EMI-TFSI are currently not available in the database, and so EMI-TFSI will be greyed-out after silicon is selected. When the Domain Modeler runs, the numerical values, applied equations and other metadata are displayed in the text area. Under Domain, the user can also select emitter domains, which are discussed below.

Table 2.6. Viscous Flow Domain Modeler properties.

Final Flow Rate
Hydraulic Resistance
Laplace Pressure
Mass Flow
Reynolds Number
Wicking Time

2.2.2 Electrohydrodynamic Flow

The electrohydrodynamic flow models compute the spray properties which are a critical for the performance of the propulsion system. They are undoubtedly the most complex domain models of ESPET. These models connect the purely fluidic conduction regions of the network with the electric conduction region of the emission sites consisting of Taylor cones and the emitted spray. We refer to the emitter domains as Taylor cone domains. Figure 2.9 summarizes the Taylor cone domain model inputs and the domain outputs to be generated by the database utilities submodel for a single Taylor cone emitter. The emitter type selection needs to occur first, which then enables options in the subsequent inputs. Similarly, the propellant type will invoke different physics for dielectric and liquid metal systems.

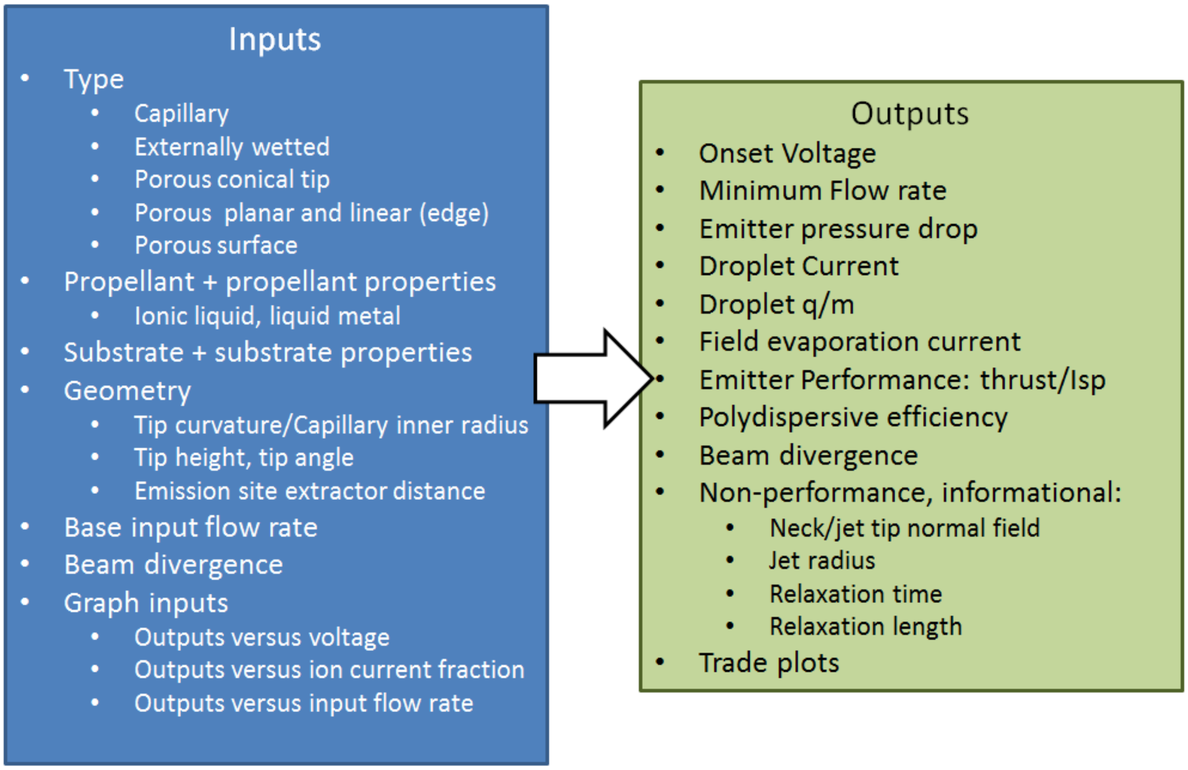

Figure 2.9. Overview of domain model inputs and outputs.

2.2.2.1 <u>Electrospray Modes</u>

In electrospray propulsion, a high electric field is applied to the vacuum-liquid interface of a low vapor pressure liquid contained within a capillary or porous orifice, or wetted on a substrate tip. When strong enough, the field deforms the liquid-vacuum interface into a convex meniscus. When the meniscus is hemispherical, the counter-acting pressures due to electric field and surface tension are balanced:

$$\frac{1}{2}\varepsilon_0 E^2 = \frac{2\gamma}{R_c} \tag{2.6}$$

where ε_0 is the vacuum permittivity, E is the electric field strength, γ is the surface tension and R_c is the meniscus. For a hemisphere, R_c could also be the radius of a capillary supporting the meniscus at its end. At slightly higher fields, the meniscus becomes a cone, a more stable shape which experiences a maximum field strength at its tip. Taylor demonstrated theoretically that this so-called Taylor cone has a half angle of $\alpha_T = 49.3°$, and this has been verified experimentally [*Taylor*, 1964]. From Eq. 2.6 we can conclude that the field strengths to generate Taylor cones are much higher for liquid metals due to their substantially higher surface tension.

Several scenarios can happen if the electric field is further increased to produce charge and bulk flow. This is illustrated in Figure 2.10. A critical property in the electrohydrodynamics of electrospray is the interfacial charge relaxation time given by:

$$\tau_{el} = \varepsilon_0 \varepsilon / K \, , \tag{2.7}$$

where K is the liquid conductivity and ε is the relative permittivity. For metals, the charge relaxation time is exceedingly short due to the high conductivity, and essentially the entire cone is an equipotential surface. For dielectric liquids with low conductivities, it is substantially longer, and thus where motion of bulk liquid occurs tangentially on the cone towards the tip, eventually, charge relaxation no longer has time to occur. At the apex, where the flow velocities are highest, an unstable volume can be identified given by the field-induced volume flow rate, Q:

$$V_{apex} = Q\varepsilon_0\varepsilon / K = \frac{2\pi}{3} r^{*3} (1 - \cos\alpha_T) \quad \textbf{(2.8)}$$

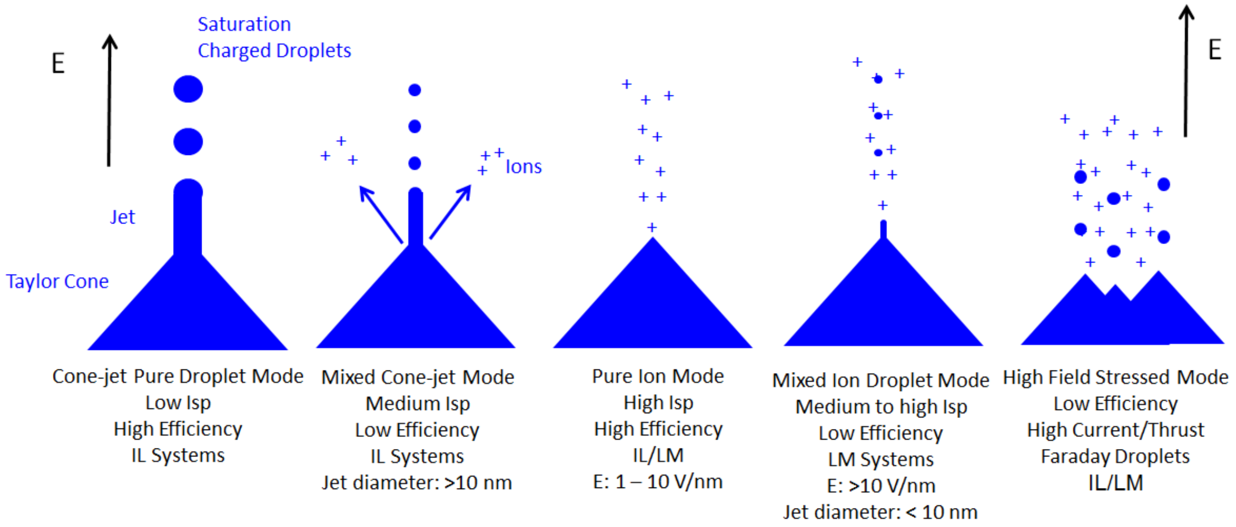

Figure 2.10. Schematic representation of different electrospray emission modes.

where r* is the distance from the apex along the cone surface to where the instability starts. The unstable volume forms a liquid jet with a radius approximately given by r_{jet} = r* sinα_T, and the combination of Taylor cone and jet is referred to as a cone-jet (see left most structure in Figure 2.10). Instabilities in the jet leads to its breakup into droplets that are charged near the saturation limit, i.e., the pressure associated with the surface charge is comparable or slightly lower than the pressure due to surface tension, $2\gamma/r$, where r is the radius of the droplet.

Fernandez de la Mora and Loscertales [*Fernández de la Mora and Loscertales*, 1994] have identified the minimum flow rate at which a Taylor cone-jet can be sustained given by:

$$Q_{\min} = \frac{\gamma\varepsilon\varepsilon_0}{4\rho K} \quad \textbf{(2.9)}$$

Using Eq. (2.9), we find that for dielectrics like ILs, the jet radius is close to ~5 nm at the minimum flow rate. At these conditions, the electric field strengths at the surface near the cone-to-jet transition region are very high on the order of 1 V/nm. This leads to field evaporation of ions near this neck region. This condition is referred to as a mixed cone-jet mode. A combination of droplets and ions is an inefficient mode of emission, as we point out more quantitatively later. Sprays with high flow rates don't exhibit ion field evaporation in the transition region. However, these sprays also produce ions which are either emitted from droplets or the end of the jet [*Gamero-Castano*, 2010].

For LM systems, due to the higher charge relaxation rates, lower flow rates can be sustained. Small jets with dimensions of ~1 nm can form. Near the onset voltage for Taylor cone formation and emission, pure ionic emission is the primary mode of operation. At higher field strengths, small charged droplets can also be emitted (see Figure 2.10). At very high fields, prior to electrical breakdown, the Taylor cones of both liquid metal and dielectric systems break up into multiple Taylor cones that emit both ions and droplets. This mode is very inefficient. The preferred modes of operation are stable cone-jets for ILs and pure ionic mode for both ILs and LMs.

2.2.2.2 ***Electrospray Propulsion Performance Relations***

The critical performance parameters, thrust, F, and specific impulse, I_{sp}, are governed by the charge-to-mass distributions of the spray and can be computed from:

$$F = \dot{m} v_{ex} = Q \rho \, v_{ex} = I_{tot} \sqrt{2V_{acc}(m/q)} \tag{2.10}$$

$$I_{sp} = \frac{v_{ex}}{g} = (1/g)\sqrt{2V_{acc}(q/m)} \tag{2.11}$$

where ρ is the liquid density, v_{ex} is the average exhaust velocity, I_{tot} is the total current, V_{acc} is the total acceleration voltage, q/m is the average charge-to-mass ratio, and g is Earth's gravitational acceleration at sea-level.

A third performance parameter is the efficiency, η, given by:

$$\eta = \frac{F^2}{2\dot{m}P}, \tag{2.12}$$

where P is the applied electrical power, $P = VI_{tot}$. Eq. (2.12) consists of the ratio between the power associated with the thrust and the input power. There are a number of sources of efficiency including dissipative losses in the jet, spray divergence, and general electrical efficiencies. As mentioned above, important efficiencies are also introduced through broad charge-to-mass distributions in the spray. This is referred to as the polydisperse efficiency, η_{poly}. For a distribution of charge-to-mass ratios, the thrust is given by:

$$F = \sum_i I_i \sqrt{2V_{acc}(m/q)_i} \tag{2.13}$$

And $\dot{m}$ in Eq. (2.12) is computed from:

$$\dot{m} = \sum_i I_i (m/q)_i \tag{2.14}$$

where I_i is the current associated with emitted charged species with mass-to-charge ratio $(m/q)_i$,. Combining equations (2.12) through (2.14), we get the polydisperse efficiency that is independent of V_{acc} if we assume that V and V_{acc} are close to identical:

$$\eta_{poly} \approx \frac{\left(\sum_i I_i \, (m/q)_i\right)^2}{\sum_i I_i (m/q)_i I_{tot}} \;. \tag{2.15}$$

2.2.2.3 ***Emitter Types***

Figure 2.11 shows schematically four emitter types that have been reported for electrospray propulsion systems. We differentiate between internally (capillary) and externally wetted emitters, and porous emitters. These types can have different geometries, such as circular capillaries, conical externally wetted and porous emitters, and ridge/edge emitters. The right-most design is a porous surface emitter first introduced by Busek. Each emitter type supports a different numbers of Taylor cones and emission sites and requires a separate domain model.

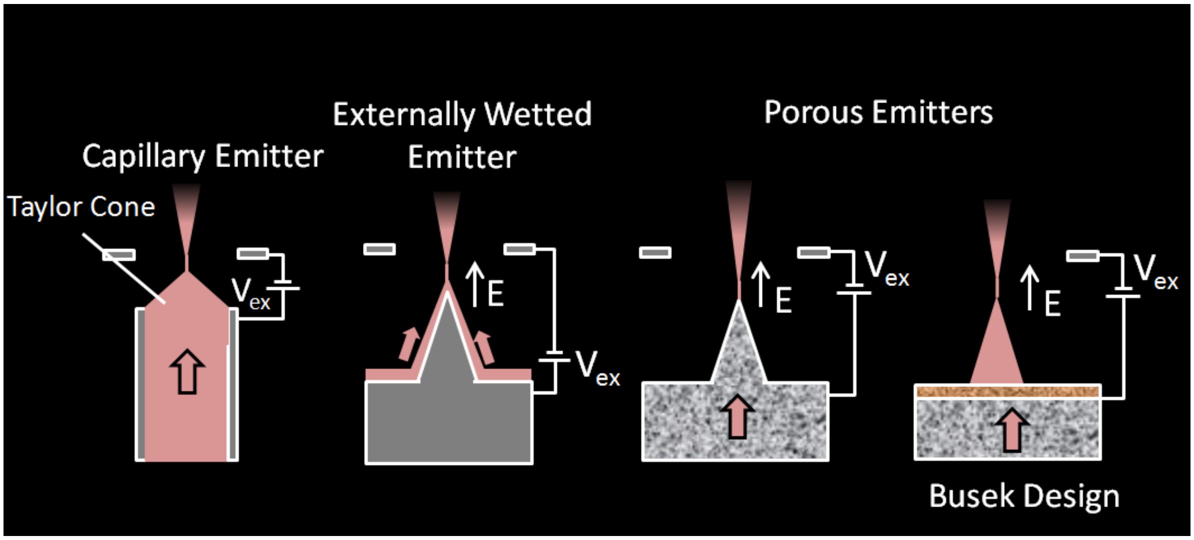

Figure 2.11. Electrospray emitter types.

2.2.2.4 ***Onset Voltage***

The onset voltage is defined as the voltage that generates the field at which the liquid surface in a capillary, emission pore, or on an emitter tip becomes unstable, and forms a Taylor cone. This voltage is very close to the voltage corresponding to the field that balances a hemispherical meniscus (Eq. 2.6). Martinez-Sanchez derive an analytical expression that relates the onset voltage, V_0, to the surface electric field strength assuming a hyperboloidal tip or meniscus for which analytical solutions of the Laplace equation exist [*Martinez-Sanchez,* 2007]:

$$E = \frac{V_0}{\tanh^{-1}(\eta_0)} \frac{1}{1-\eta_0^2} \frac{\eta_0}{d} \tag{2.16}$$

where η_0 is given by:

$$\eta_0 = (1 + R_c / D)^{-1/2} \tag{2.17}$$

where D is the tip-extractor distance, R_c is the capillary inner radius for an internally wetted emitter, or the tip curvature radius for a porous cone or externally wetted conical emitter. For edge emitters, R_c is well represented by the sharp curvature of the edge. Solving for the onset voltage, we get for non-porous emitters:

$$V_0 = \tanh^{-1}(\eta_0)(1-\eta_0^2)\sqrt{\frac{a^2\gamma}{\varepsilon_0 R_c}} \tag{2.18}$$

where a is given by:

$$a = 2D\sqrt{1 + R_c / D} = 2D / \eta_0 \tag{2.19}$$

For porous tips, Eq. (2.18) is modified by a simple square-root ratio between the tip curvature and the Taylor cone base radius, r_{base}, which is related to the pore size:

$$V_0 = \tanh^{-1}(\eta_0)(1-\eta_0^2)\sqrt{\frac{a^2\gamma}{\varepsilon_0 r_{base}}} = \tanh^{-1}(\eta_0)(1-\eta_0^2)\sqrt{\frac{a^2\gamma}{\varepsilon_0 R_c}}\sqrt{\frac{R_c}{r_{base}}} \tag{2.20}$$

After emission onset, flow is induced, and a pressure drop at the Taylor cone occurs given by QR_h, where R_h is the hydraulic resistance of the combined emitter-feed system. This results in a negative internal pressure, P_{int}, that needs to be overcome by the electric field in addition to the capillary force. The onset voltage is then given by:

$$V_0 = \tanh^{-1}(\eta_0)(1-\eta_0^2)\sqrt{\frac{a^2}{\varepsilon_0}\left(\frac{\gamma}{r_{base}} - \frac{P_{\mathrm{int}}}{2}\right)} \tag{2.21}$$

For positively pressurized systems (actively pressurized), we revert to Eq. 2.18.

2.2.2.5 Theory of Dielectric Propellant Cone-jets (ILs)

2.2.2.5.1 Actively Pressurized Cone-jet Model

Actively pressurized systems control the volume flow rate, $Q = p/R_h$. An example of an actively pressurized system is the Busek LISA pathfinder thruster [*Gamero-Castaño*, 2004; *Gamero-Castaño and Hruby*, 2001]. In these systems, the voltage is set at a point where high Taylor cone stability is observed, and the thrust is controlled through the mass flow, $Q\rho$. The droplet current can then be obtained from the empirical expression derived by Gañán-Calvo *et al.* [*Ganan-Calvo, et al.*, 1997]:

$$I_{droplet} = \sqrt{\frac{\varepsilon_0\gamma^2}{\rho}}\left[6.2\sqrt{\frac{Q\rho K}{\gamma\varepsilon_0\sqrt{\varepsilon-1}}} - 2\right] = I_0\left[6.2\sqrt{\frac{Q}{Q_0\sqrt{\varepsilon-1}}} - 2\right]$$
$$Q_0 = \frac{\gamma\varepsilon_0}{\rho K}, I_0 = \sqrt{\frac{\varepsilon_0\gamma^2}{\rho}} \tag{2.22}$$

Equation (2.22) is sufficient to compute the performance for a high-flow rate system where the spray is dominated by charged droplet emission. A small error is introduced by ion emission from droplets and the tip of the jet, where droplets break off. At low flow rates, the error can become more significant due to ion evaporation, which needs to be taken into account. For this purpose, we need to know the highest electric field strengths at the surfaces of the cone-jet. The flow rate determines the size of the jet which is controlled by the region at the Taylor cone apex where flow rates are too high for charge relaxation to occur. This consideration leads to an expression for the maximum normal surface electric field at the cone-jet surface, which is located at the neck of the jet (cone-jet transition region):

$$E_n^v = \frac{\gamma^{1/2}K^{1/6}}{\varepsilon_0^{2/3}Q^{1/6}} \quad . \tag{2.23}$$

The dependence of the ion evaporation current on the applied electric field, E_n^v, can be computed from the well know expression for the field evaporation current density, j_e, and the approximate area available for evaporation, A:

$$\boldsymbol{I(E_n^v) = A(E_n^v)\cdot j_{\mathrm{e}}(E_n^v)} \tag{2.24}$$

where j_e is given by:

$$\boldsymbol{j_{\mathrm{e}}(E_n^v) = \sigma(E_n^v)\frac{k_{\mathrm{B}}T}{h}\exp\left[-\frac{\Delta G - G(E_n^v)}{k_{\mathrm{B}}T}\right]}, \tag{2.25}$$

where k_B is the Boltzmann constant, h is Planck's constant, and T is the temperature. The area in Eq. (2.24) is estimated by:

$$A(E_n^v) = \pi r_e^2, \, r_e = \frac{4\gamma}{\varepsilon_0 E_n^{v2}} \tag{2.26}$$

In (2.25), *ΔG* is the solvation energy of the evaporated ions, and $G(E_n^v)$ is given by:

$$\boldsymbol{G(E_n^v) = \sqrt{\frac{q^3 E_n^v}{4\pi\epsilon_0}}}. \qquad \textbf{(2.27)}$$

The surface charge density, $\sigma(E_n^v)$, is the critical unknown and varies with the field and the emission current. It can be computed by assuming a steady state and setting its change with time to zero. It is then given by the build-up through convection and conduction current densities and the reduction by field evaporation:

$$\boldsymbol{\frac{d\sigma}{dt} = j_{\mathrm{conv}} + j_{\mathrm{cond}} - j_{\mathrm{e}}}. \qquad \textbf{(2.28)}$$

The conduction current is given by:

$$j_{cond} = KE_n^l \qquad \textbf{(2.29)}$$

where E_n^l is the field inside the liquid, and is related to the surface charge through:

$$\sigma = \varepsilon_0 (E_n^v - \varepsilon E_n^l) \qquad \textbf{(2.30)}$$

Coffman [*Coffman*, 2016] demonstrates that for typical ionic liquids, the convection current, j_{conv}, can be neglected. We, therefore, can set:

$$j_e = KE_n^l, \qquad \textbf{(2.31)}$$

which directly demonstrates that dielectric liquid field evaporation is limited by the conduction of the propellant. This is in contrast to liquid metals, where the emission currents are limited by space charge.

By combining equations (2.25), (2.29), and (2.30), we can derive the field inside the liquid:

$$E_n^l = \frac{E_n^v}{\varepsilon\left(1 + \frac{hK}{\varepsilon_0 \varepsilon k_B T} \exp\left[-\frac{1}{k_B T}\{\Delta G - G(E_n^v)\}\right]\right)} \qquad \textbf{(2.32)}$$

With Eq. (2.32), we can compute *σ*, and the ion field evaporation current density can then be obtained from either (2.31) or (2.25).

Although not necessary for computing the ion evaporation current, we can also get a good estimate of the jet radius, r_{jet}, which can be related to the point, *r**, along the Taylor cone apex beyond which charge relaxation has insufficient time to occur:

$$r_{jet} = r^* \sin(\alpha_T). \qquad \textbf{(2.33)}$$

where α_T is the Taylor cone apex half angle (49.3°). *r** is given by:

$$r^* = \left(\frac{3}{2}\frac{Q\varepsilon_0\varepsilon}{\pi K(1-\cos\alpha_T)}\right)^{1/3} \qquad \textbf{(2.34)}$$

where *ε* is the relative permittivity of the propellant. The minimum jet radius of a cone-jet is around ~5 nm, below which the jet becomes unstable. We will consider r_{jet} at the minimum flow rate as a metric for determining pure ion evaporation.

Figure 2.12 compares non-dimensional scaled values of the field evaporation ion current, the current density, and the charge density computed for EMI-BF4 as a function of non-dimensional field scaled by

E_n^{v*}, the field at which the exponent in Eq. (2.25) is zero. As is seen, the charge at the cone-jet builds up with increasing field until ion evaporation depletes it. The model breaks down at higher fields where a maximum is predicted, however, laboratory results show that the current continues to rise when the field increases. It is possible that neglecting the convection term is the source of inaccuracy.

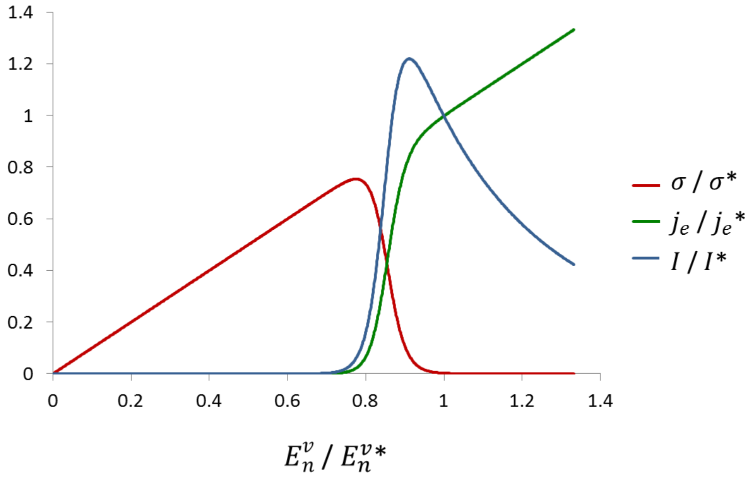

Figure 2.13. The surface charge, evaporative current density, and ion evaporation current, each scaled in non-dimensional units as defined by Higuera [*Higuera*, 2008]. The results were obtained using the IL EMI-BF4.

We, therefore, have the means for computing both the charged-droplet current, where the charge-to-mass ratio of droplets is given by the ratio of droplet current and droplet mass flow rate, and the ion evaporation current. Figure 2.14 shows droplet and ion currents computed for positive extraction currents (positive polarity) of EMI-TFSI and EMI-BF4 as a function of volume flow rate. The curves also show the evolution of the jet radius, which, as expected, is ~5 nm at the minimum cone-jet flow rate. It is seen that the field evaporation current represents a larger fraction of the total current at the minimum flow rate for EMI-BF4, consistent with the greater ease with which pure ion emission can be achieved with EMI-BF4. For this IL, the field evaporation current saturates at ~50 nA. However, substantially higher currents have been observed for single emitters [*Guerra-Garcia, et al.*, 2016] when in a pure ionic mode.

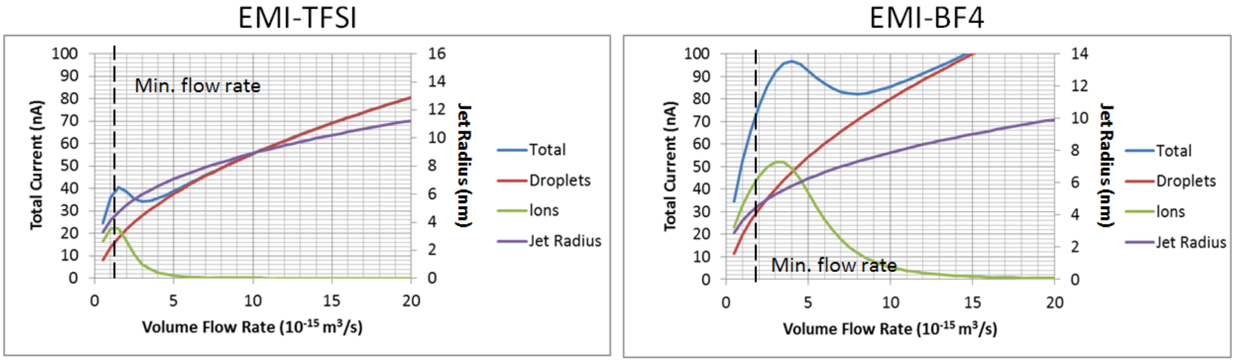

Figure 2.14. Droplet and ion currents, and jet radius versus volume flow rate computed for EMI-TFSI and EMI-BF4.

2.2.2.5.2 Passively Pressurized Cone-jet Model

In passively pressurized emitters, the electric field induces the propellant flow. In a first approximation we can relate the electric-field induced pressure drop at the meniscus through the relation:

$$\Delta p = \frac{1}{2}\varepsilon_0 {E_n}^2 \tag{2.35}$$

where E_n is the external surface normal electric field. From the onset voltage expressions (Section 2.3.2.4), we then obtain:

$$\Delta p \approx p_{scale}\frac{2\varepsilon_0(V^2-V_0^2)}{a^2\text{atanh}^2(\eta)(1-\eta^2)^2} = p_{scale}\,p_0(V^2-V_0^2),\; p_0 = \frac{2\varepsilon_0}{a^2\text{atanh}^2(\eta)(1-\eta^2)^2} \tag{2.36}$$

where p_{scale} is an adjustable parameter that we must benchmark through comparison to experiment. Once Δp is determined, Q can be computed from the hydraulic resistance and the cone-jet theory introduced in Section 2.2.2.5.1 can be applied.

2.2.2.5.3 Model for Pure-Ionic Regime

We base the model for the pure-ionic regime on recent excellent work by Coffman [*Coffman*, 2016] and Coffman *et al.* [*Coffman, et al.*, 2016] that have provided new insights to conditions for this mode. These authors derived following expression for the pure ionic mode:

$$I_{ion} = I_{\min}^{ion} + \xi\frac{V-V_0}{C_R}, \tag{2.37}$$

where $I_{\min}^{ion}$ is the minimum onset current, ξ is a slope parameter, and C_R is a dimensionless form of the hydraulic resistance:

$$C_R = \frac{KE_{tip}r_{base}^3R_{feed}}{2\gamma\rho(q/m)}, \tag{2.38}$$

E_{tip} is the electric field strength at the tip of the emitter, r_{base} is the base Taylor cone radius, and R_{feed} is the hydraulic resistance of the feed system. Coffman [*Coffman*, 2016] explored the complex phase space of E_{tip}, R_{feed}, and r_{base} and identified a new high R and E regime of stable cones that are flattened with respect to the standard Taylor cone. The theory, however, is insufficiently mature for inclusion in ESPET. Because the most critical parameter appears to be C_R, we proposed to benchmark ESPET to identify a mode-switching limit, C_R^{Limit}, for C_R above which the system enters a pure-ionic regime.

In Eq. (2.37), we determine $I_{\min}^{ion}$ from the field evaporation current determined for a minimum flow rate. The parameter ξ needs to be benchmarked. Coffman *et al.* [*Coffman, et al.*, 2016] suggested the parameter, ξ, is universal, i.e., applicable to all dielectric propellants.

For ILs, we assume that half of the pure ion current consists of monomer ions and the other half of dimers, i.e., $A^+(AB)$ or $B^-(AB)$ complex ions. The polydisperse efficiency for a mixed cone-jet mode assuming the electric voltage equals the acceleration voltage is then given by:

$$\eta_{poly} \approx \frac{\left(I_{Droplet}\sqrt{(m/q)_{Droplet}} + 0.5I_{Ion}\left(\sqrt{(m/q)}_{monomer} + \sqrt{(m/q)}_{\dim er}\right)\right)^2}{\left\{I_{Droplet}(m/q)_{Droplet} + 0.5I_{Ion}\left[(m/q)_{monomer} + (m/q)_{\dim er}\right]\right\}I_{tot}} \tag{2.39}$$

With $(m/q)_{Droplet} = Q_{Droplet}\rho/I_{Droplet}$, we get

$$\eta_{poly} = \frac{\left(I_{Droplet}\sqrt{(m/q)_{Droplet}} + 0.5 I_{Ion}\left(\sqrt{(m/q)}_{monomer} + \sqrt{(m/q)}_{\mathrm{dimer}}\right)\right)^2}{\left\{Q_{droplet}\rho + 0.5 I_{Ion}\left[(m/q)_{monomer} + (m/q)_{\mathrm{dimer}}\right]\right\} I_{tot}}$$
$$= \frac{\left(I_{Droplet}\sqrt{(m/q)_{Droplet}} + 0.5 I_{Ion}\left(\sqrt{(m/q)}_{monomer} + \sqrt{(m/q)}_{\mathrm{dimer}}\right)\right)^2}{\left\{Q_{droplet}\rho + 0.5 I_{Ion}\left[(m/q)_{monomer} + (m/q)_{\mathrm{dimer}}\right]\right\} I_{tot}} \qquad \mathbf{(2.40)}$$

Through the introduction of the ion current fraction, f_{ion}, we obtain an expression that does not depend on I_{tot}:

$$\eta_{poly} = \frac{\left((1-f_{ion})\sqrt{(m/q)_{Droplet}} + 0.5 f_{ion}\left(\sqrt{(m/q)}_{monomer} + \sqrt{(m/q)}_{\mathrm{dimer}}\right)\right)^2}{\left\{(1-f_{ion})(m/q)_{Droplet} + 0.5 f_{ion}\left[(m/q)_{monomer} + (m/q)_{\mathrm{dimer}}\right]\right\}} \qquad \mathbf{(2.41)}$$

2.2.2.6 Electrospray Theory of Liquid Metals (LMs)

Unlike ILs, LM system output currents are limited by space charge and, therefore, follow different physics. Furthermore, LM systems can only operate in a positive polarity since a negative polarity would result in an electron beam with essentially no thrust. For LM systems, ESPET 1.0 follows the work of Mair who derived a current-voltage expression for "low-impedance" liquid metal capillaries or low-impedance, grooved externally wetted emitters or emitters with roughened surfaces [*Mair*, 1997]:

$$I_{emitter} = 3\pi\sqrt{\frac{2e}{M}}\,\frac{r_{base}\gamma\cos\alpha_T}{2V^{1/2}}\left(\left(\frac{V}{V_0}\right)^2 - 1\right) \qquad \mathbf{(2.42)}$$

where *M* is the metal atomic mass, *e* is the unit charge, α_T is the Taylor cone half angle (49.3°). For $V/V_0 < 1.1$, Equation (2.42) reduces to

$$I_{emitter} = 3\pi\sqrt{\frac{2e}{M}}\,\frac{r_{base}\gamma\cos\alpha_T}{V_o^{1/2}}\left(\left(\frac{V}{V_0}\right) - 1\right) = (V - V_0)/Z$$
$$1/Z = 3\pi\sqrt{\frac{2e}{M}}\,\frac{r_{base}\gamma\cos\alpha_T}{V_o^{3/2}} \qquad \mathbf{(2.43)}$$

where *Z* is the ***electrical*** impedance (units of Ohm). Equation (2.43) predicts a linear I-V relationship with slope given by 1/*Z* at currents below extraction voltages $V/V_0 = 1.1$. Note that this is very similar to the pure-ionic regime in dielectric systems.

For high-impedance liquid metal Taylor cones (smooth externally wetted tips, or small capillaries), a flow-impedance (hydraulic resistance) factor is introduced:

$$I_{emitter} = 3\pi\sqrt{\frac{2e}{M}}\,\frac{r_{base}\gamma\cos\alpha_T}{2V^{1/2}}\left(\left(\frac{V}{V_0}\right)^2 - 1\right) \times \left[1 + \frac{3\pi r_{base}^2 R_{hyd}}{4\rho V^{1/2}(e/2M)^{1/2}}\right]^{-1}$$
$$\approx 3\pi\sqrt{\frac{2e}{M}}\,\frac{r_{base}\gamma\cos\alpha_T}{V_o^{1/2}}\left(\left(\frac{V}{V_0}\right) - 1\right) \times \left[1 + \frac{3\pi r_{base}^2 R_{hyd}}{4\rho V^{1/2}(e/2M)^{1/2}}\right]^{-1} \qquad \mathbf{(2.44)}$$
$$1/Z \approx 3\pi\sqrt{\frac{2e}{M}}\,\frac{r_{base}\gamma\cos\alpha_T}{V_o^{3/2}}\left[1 + \frac{3\pi r_{base}^2 R_{hyd}}{4\rho V_o^{1/2}(e/2M)^{1/2}}\right]^{-1}$$

The inclusion of the hydraulic resistance becomes important when the additional factor in square brackets is significantly above 1. As demonstrated by Tajmar and Genovese [*Tajmar and Genovese*, 2003], for a given emitter current, the droplet fraction declines dramatically when the square bracket term becomes significantly greater than 1 and the emitter current is limited by the flow impedance.

The current-voltage expressions do not allow us to estimate the mass efficiency, which is necessary to determine thrust and specific impulse. Tajmar [*Tajmar*, 2005] derived an empirical expression for the mass efficiency as a function of Taylor cone base radius for low-impedance systems that follow Eqs. 2.42 and (2.43). The mass efficiency is given by:

$$\eta = \frac{\dot{m}_{atomic}}{\dot{m}} = \left(\frac{I}{I_c}\right)^{\alpha} \tag{2.45}$$

where $\dot{m}_{atomic}$ is the mass flow for a spray consisting only of singly charged indium ions, and $\dot{m}$ is the actual volume or mass flow that we are attempting to retrieve. α is an empirical parameter and I_c is a critical current below which $\eta = 1$ and is parameterized for indium to be:

$$I_c = 0.0005 r_{base}^2 - 0.1085 r_{base} + 10.121 \quad [\mu A]. \tag{2.46}$$

Tajmar provides an empirical formula for the exponent parameter, α, as a function of r_{base}. The formulae, as published, are flawed. The main problem is that η is computed in units of %, however, Eq. (2.45) only works when the maximum efficiency is 1. Even with this realization, the expression as given for $r_{\text{base}} <$ 5.8 µm does not make sense. Consequently, we digitized the Tajmar data that produced the parameter function and conducted a fit to Tajmar's functional form ourselves. This results in following expressions (r_{base} in µm):

$$\begin{array}{l} I \le I_c : \eta = 1 \\ I > I_c \begin{cases} \eta = \left(\dfrac{I}{I_c}\right)^{-0.1569 r_{base} + 0.0579} & r_{base} < 5.8 \mu m \\ \eta = \left(\dfrac{I}{I_c}\right)^{-0.01 r_{base} - 0.87} & r_{base} \ge 5.8 \mu m \end{cases} \end{array} \tag{2.47}$$

From these parameterizations we can get $\dot{m}$ from:

$$\dot{m} = \dot{m}_{atomic} / \eta = \frac{MI}{q\eta}, \tag{2.48}$$

where I is determined using the theory of Mair [*Mair*, 1997]. The droplet mass flow rate is then obtained from:

$$\dot{m}_{drop} = (1-\eta)\dot{m} \tag{2.49}$$

and the atomic ion and droplet currents are computed from:

$$I_{ion} = \eta \dot{m} \frac{q}{m} \tag{2.50}$$

$$I_{drop} = I - I_{ion} \tag{2.51}$$

2.2.3 Emitter Domain Models

The emitter domain models provide an opportunity for the user to examine various properties of an emitter, with initial estimates of performance properties at specified flow rates. They also provide a means to generate components that become parts of a network that can be analyzed with the SPICE solver.

2.2.3.1 Internally Wetted (Capillary) Model

Figure 2.15 shows a screenshot of the ESPET domain modeler screen that pops up once "Emitter Capillary" is chosen in the "Domain" dropdown menu. The onset voltage is computed using a simplified expression which holds when $D >> R_c$:

$$V_0 = \ln(GD / R_c)\sqrt{\gamma R_c / \varepsilon_0} \tag{2.52}$$

where the user needs to set G = 4 to have the closest correspondence to Eq. (2.18). Figure 2.16 shows outputs produced when "Run" is clicked. This is only a fraction of the total outputs where expressions used to compute the various properties are also provided (including Eq. 2.52 for the onset voltage). If a temperature range is desired for properties selected in the "Field" dropdown menu, a plot is generated of the temperature dependence of this property. Figure 2.17 shows the temperature dependence of the onset voltage obtained in this way. The observed temperature dependence is a consequence of the temperature dependent surface tension.

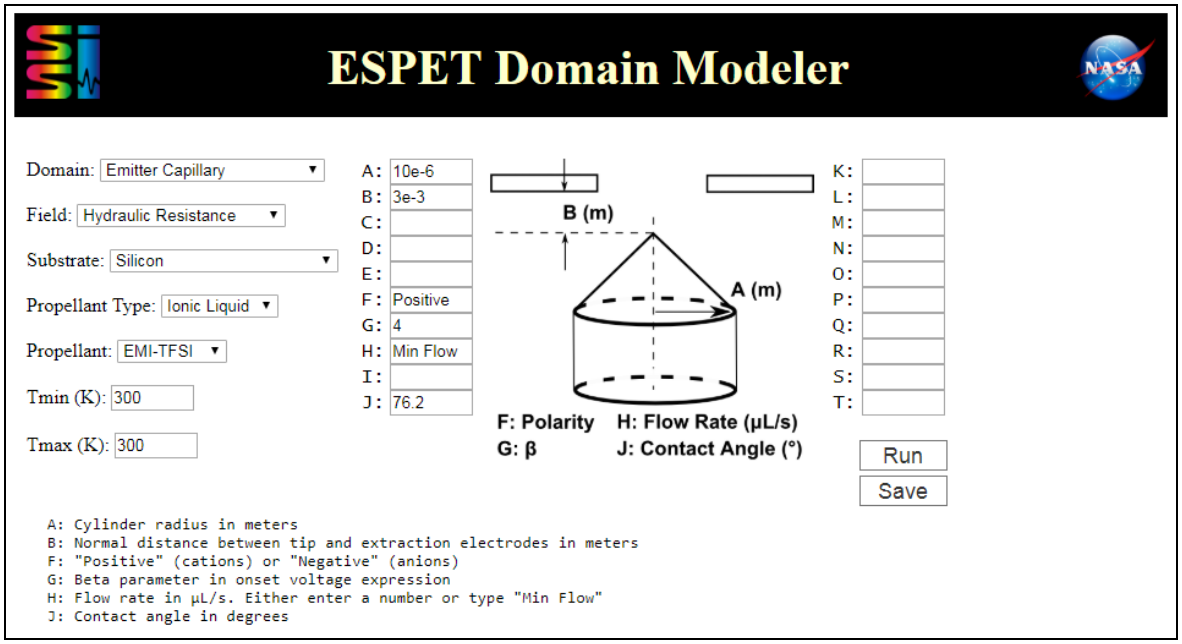

Domain: Emitter Capillary
Field: Hydraulic Resistance
Substrate: Silicon
Propellant Type: Ionic Liquid
Propellant: EMI-TFSI
Tmin (K): 300
Tmax (K): 300

A: 10e-6
B: 3e-3
C:
D:
E:
F: Positive
G: 4
H: Min Flow
I:
J: 76.2

K:
L:
M:
N:
O:
P:
Q:
R:
S:
T:

```
A: Cylinder radius in meters
B: Normal distance between tip and extraction electrodes in meters
F: "Positive" (cations) or "Negative" (anions)
G: Beta parameter in onset voltage expression
H: Flow rate in μL/s. Either enter a number or type "Min Flow"
J: Contact angle in degrees
```

Figure 2.15. Screen capture of capillary emitter domain model.

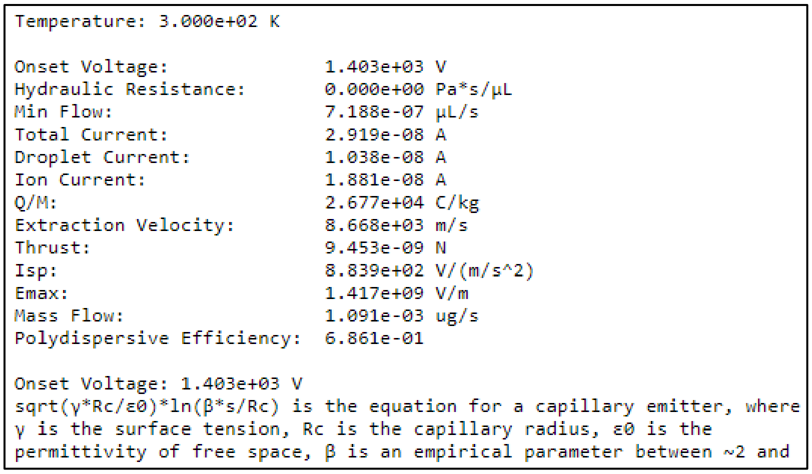

```
Temperature: 3.000e+02 K

Onset Voltage:              1.403e+03 V
Hydraulic Resistance:       0.000e+00 Pa*s/μL
Min Flow:                   7.188e-07 μL/s
Total Current:              2.919e-08 A
Droplet Current:            1.038e-08 A
Ion Current:                1.881e-08 A
Q/M:                        2.677e+04 C/kg
Extraction Velocity:        8.668e+03 m/s
Thrust:                     9.453e-09 N
Isp:                        8.839e+02 V/(m/s^2)
Emax:                       1.417e+09 V/m
Mass Flow:                  1.091e-03 ug/s
Polydispersive Efficiency:  6.861e-01

Onset Voltage: 1.403e+03 V
sqrt(γ*Rc/ε0)*ln(β*s/Rc) is the equation for a capillary emitter, where
γ is the surface tension, Rc is the capillary radius, ε0 is the
permittivity of free space, β is an empirical parameter between ~2 and
```

Figure 2.16. Screen capture of outputs for configuration in Figure 2.15. This is only a partial output of what is produced.

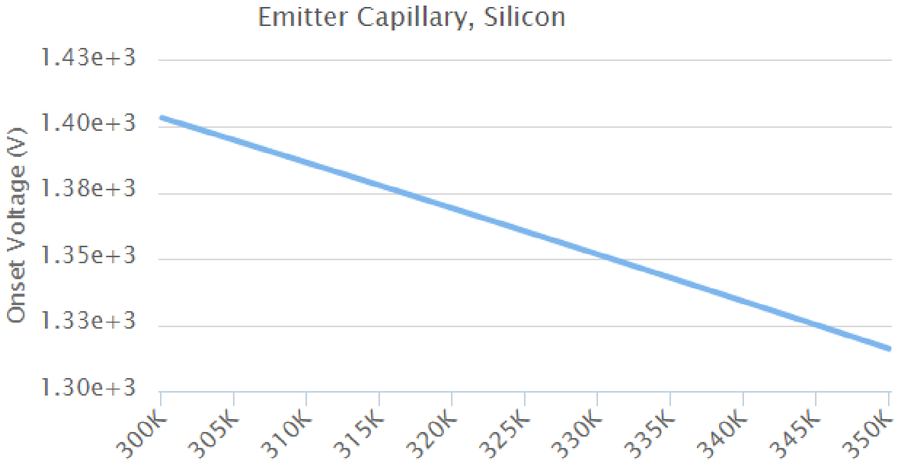

Figure 2.17. Capillary emitter domain model output for the temperature dependence of the onset voltage.

All properties listed in Figure 2.16 can be selected in the "Field" menu for graphical examination. For capillary emitter models, we assume a zero hydraulic resistance associated with the emitter structure. In a network, the length of the capillary would have to be specified, which would then allow the definition of a feed resistance. The performance properties are computed assuming the onset voltage is the acceleration voltage.

The domain model is set up for an actively pressurized system where the user sets the flow rate. The default flow rate is the minimum flow rate (Eq. 2.9). The current and spray properties are computed with the expressions introduced in Section 2.2.2.5.1.

For metal systems, the interface is run in the same way, but the physics is taken from Section 2.2.2.6, where the base radius is given by the capillary inner diameter.

2.2.3.2 __Externally Wetted Model__

Figure 2.18 shows a screen snapshot of the domain modeler when selecting an externally wetted emitter cone domain. This model has the additional critical parameter, the tip curvature, which replaces the Taylor cone base. Otherwise it is set up the same way as the internally wetted model above. The user controls the flow rate. The domain model does not compute the passively generated flow. As in the internally wetted case, performance parameters are computed assuming the extraction voltage is equivalent to the onset voltage. The same set of performance parameters are computed as those shown for the internally wetted emitter in Figure 3.16.

In the QuickSolver, for externally wetted emitters of liquid metals we assumed a single emission site, and we allowed for grooved or smooth surface liquid conductance. Eq. (2.2) is then used to compute the hydraulic resistance of the cone for which a film thickness has to be specified.

For the dielectric model, we allow for multiple emission sites. However, we assume a negligible hydraulic resistance of the emitter tip, the hydraulic resistance of which has to be included as part of the feeding network. Figure 2.19 provides a schematic of how we model the externally wetted dielectric emitter in the QuickSolver. The emitter is defined by its curvature of a roughened surface where we specify a roughness parameter which defines normal distribution of curvatures of protruding emission sites on which Taylor cones form due to localized higher surface field strengths. The individual emission sites have onset voltages given by the same formula for porous emitters (Eq. 2.20), where the Taylor cone base is not provided by pore radii, but the radii given by the roughness sites. The model then determines for each site the onset voltage, which determines the sequence in which the individual sites are turned on. Here the model assumes that the hydraulic resistance is independent of the number of sites that are active on an emitter. We find this is not the case for the porous emitters, where the hydraulic resistance is lower.

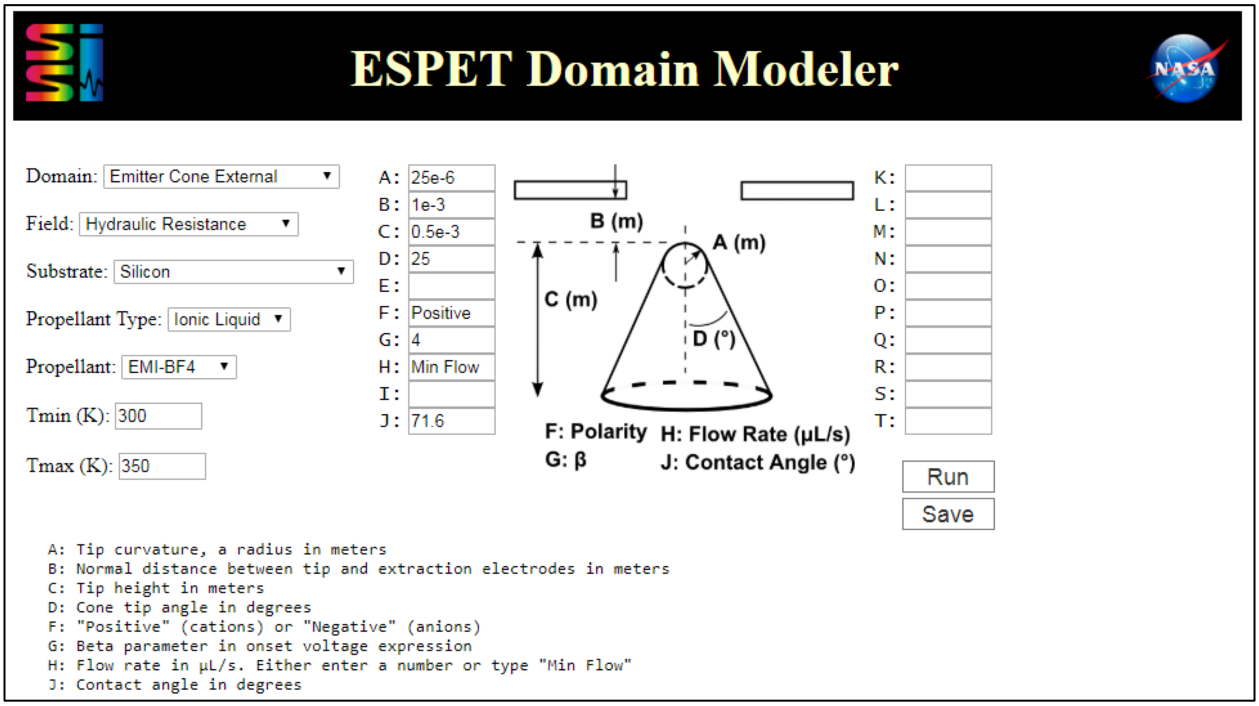

Domain: Emitter Cone External
Field: Hydraulic Resistance
Substrate: Silicon
Propellant Type: Ionic Liquid
Propellant: EMI-BF4
Tmin (K): 300
Tmax (K): 350

A: 25e-6
B: 1e-3
C: 0.5e-3
D: 25
E:
F: Positive
G: 4
H: Min Flow
I:
J: 71.6

```
A: Tip curvature, a radius in meters
B: Normal distance between tip and extraction electrodes in meters
C: Tip height in meters
D: Cone tip angle in degrees
F: "Positive" (cations) or "Negative" (anions)
G: Beta parameter in onset voltage expression
H: Flow rate in μL/s. Either enter a number or type "Min Flow"
J: Contact angle in degrees
```

Figure 2.18. Screen capture of capillary emitter domain model.

The user can also choose an externally wetted edge emitter. The primary difference in this model is the calculation of the hydraulic resistance. Note that edge emitters have high uncertainty in the number of emission sites, and the computation of an effective hydraulic resistance to the individual emission sites may ultimately require a numerical solver.

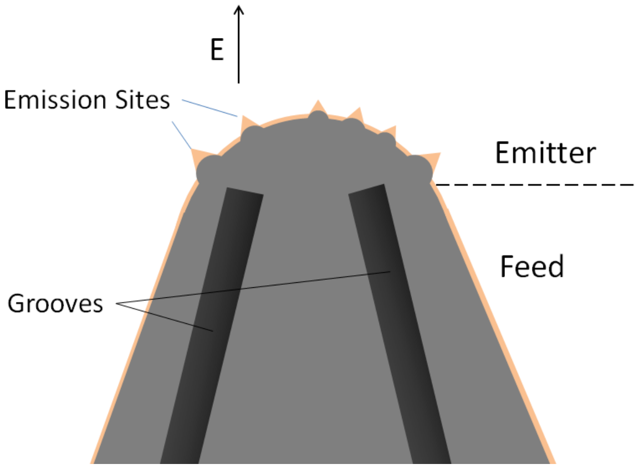

Figure 2.19. Schematic of the emission tip for the baseline model of externally wetted emitters for dielectric propellants.

2.2.3.3 Porous Emitter Model

Figure 2.20 shows a screen snapshot of the domain modeler when selecting a porous emitter cone domain. As for the externally wetted cone, the domain modeler assumes a single emission site per emitter. The domain modeler retrieves the effective pore size and porosity of the substrate. The domain modeler for this domain computes also the permeability of the porous medium.

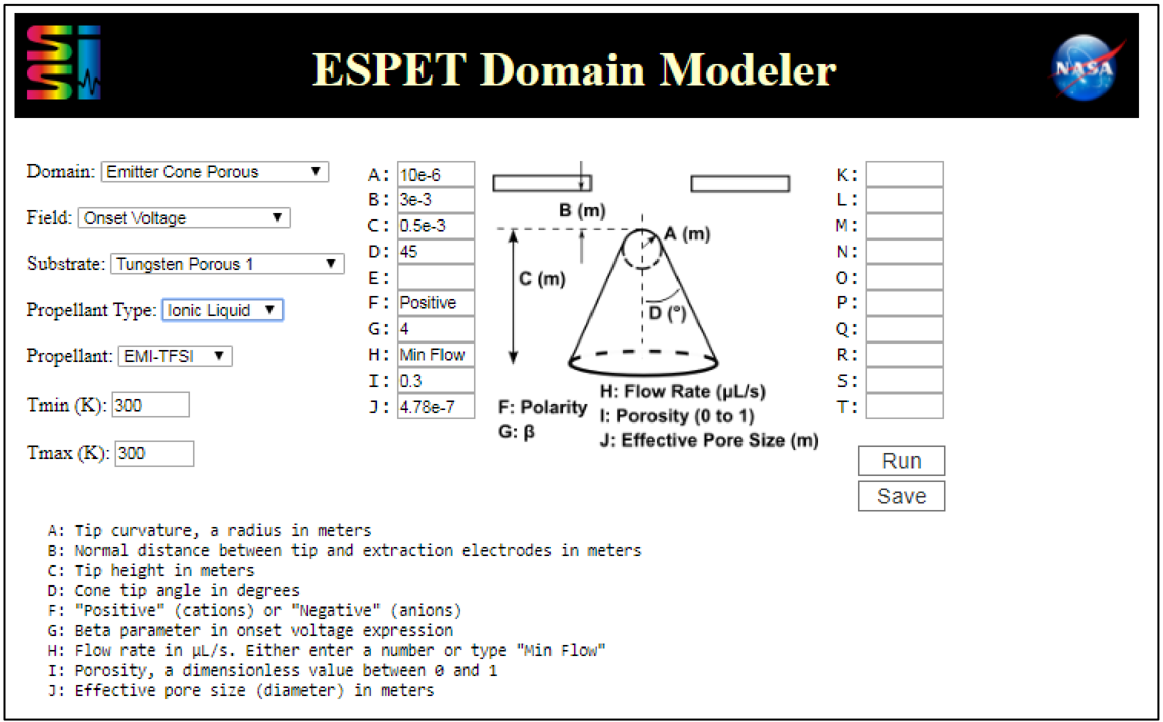

ESPET Domain Modeler

Domain: Emitter Cone Porous
Field: Onset Voltage
Substrate: Tungsten Porous 1
Propellant Type: Ionic Liquid
Propellant: EMI-TFSI
Tmin (K): 300
Tmax (K): 300

A: 10e-6
B: 3e-3
C: 0.5e-3
D: 45
E:
F: Positive
G: 4
H: Min Flow
I: 0.3
J: 4.78e-7
K:
L:
M:
N:
O:
P:
Q:
R:
S:
T:

```
A: Tip curvature, a radius in meters
B: Normal distance between tip and extraction electrodes in meters
C: Tip height in meters
D: Cone tip angle in degrees
F: "Positive" (cations) or "Negative" (anions)
G: Beta parameter in onset voltage expression
H: Flow rate in μL/s. Either enter a number or type "Min Flow"
I: Porosity, a dimensionless value between 0 and 1
J: Effective pore size (diameter) in meters
```

Figure 2.20. Screen capture of porous cone emitter domain model.

The emitter models incorporated in the QuickSolver are more sophisticated than the domain modeler models. For liquid metals, we assume a single emission site for porous emitters. The excellent benchmarking data provided to us by Busek for ILs (see Section 3.6.1) have allowed us to develop a more detailed model of a porous cone accounting for multiple emission sites. Two refinements of the base emitter domain model have been added: an emission site hydraulic resistance that is proportional to the number of active sites of the emitter, and propellant pooling at emission site pores. A critical aspect of both current models is the hydraulic resistance associated with each emission site. For the hydraulic resistance we assume that the total hydraulic resistance is given by Eq. (2.3), which consists of the sum of the resistances associated with each emission site. Thus, assuming equal resistances for each site, the hydraulic resistance of an individual site is $NR_{hyd},$ where N is the number of active sites. Thus, with each emission site, the microfluidic path involves a smaller volume within the tip and thus a higher hydraulic resistance.

The propellant pooling also depends on the number of active emission sites of an emitter. We use following empirical function to determine the Taylor cone base radius, b_i, as a function of emission site i:

$$b_i = b_0\left[1-\left(\frac{i-1}{N_{\max}-1}\right)^{1/4}\right]+r_0 \tag{2.53}$$

where r_0 is the pore size of the medium, b_0 is the initial pool radius, and N_{max} is an adjustable parameter that corresponds to the maximum number of emission sites governed by Taylor cone base enlargement over the nominal average pore size. For $i = N_{max}$, b equals r_0.

Similarly to the externally wetted emitter model, the porous model also has an edge emitter option. Contrary to the externally wetted emitter model, there is an additional option to compute properties of an array of porous cone or porous edge emitters. Figure 2.21 shows the screen snapshot for the porous emitter cone array domain modeler. Here the user has the opportunity to specify the number of emission sites per emitter in addition to the total number of emitters. Furthermore, the standard deviation of effective pore size, tip curvature and extractor-tip distance can be specified, resulting in a random selection of these parameters based on a normal probability distribution. The domain modeler, however, does not compute emission site specific onset voltages, i.e., all sites turn on at the same voltage. This occurs, however, within the network solver using a component generated with the porous emitter cone array domain modeler. Note also that in this model, the user can specify the extraction voltage, where the onset voltage is the default value.

In the porous IL emitter models of the QuickSolver, we provide an estimate for the number of emission sites through the simple expression:

$$N_{sites} = \frac{A_{emission}}{A_{Taylor}} \tag{2.54}$$

where A_{Taylor} is the Taylor cone base area and $A_{emission}$ is the effective emission are of the cone. The Taylor cone area is not straightforward to estimate because in our model, it changes with the number of emission sites (Eq. 2.53) with the varying Taylor cone base radius from r_{pool} + r_{pore} to r_{pore}, where r_{pool} is the pooling radius and r_{pore} is the pore size. In the benchmarking phase of this work, we found that for conical porous emitters, the number of emission sites is underestimated if the average initial Taylor cone base size is used. We start with an expression that provides an improved comparison by giving the final Taylor cone radius a higher weight:

$$A_{Taylor} = \pi\left\{(r_{pool}+2r_{pore})/3\right\}^2 \tag{2.55}$$

$A_{emission}$ is obtained from:

$$A_{emission} = 2\pi R_c^2\{1-\cos(90-\alpha)\} \tag{2.56}$$

where R_c is the cone radius of curvature and α is the cone half angle in degrees. Eq. (2.55) is merely the cone half angle subtended surface given by the solid angle $2\pi\{1\text{-}\cos(90\text{-}\alpha)\}$.

For porous edge emitters, we take the same approach but we assume that there are many more sites and that the Taylor cone area is less dependent of the number of active sites and is given by:

$$A_{Taylor} = \pi r_{pool}^2 \tag{2.57}$$

The emission area is a composite of the conical emission area (representing the two edge end caps) and the ridge area between the caps:

$$A_{emission} = 2\pi R_c^2\{1-\cos(90-\alpha)\} + 2\frac{\pi}{180}(90-\alpha)R_c L \tag{2.58}$$

where *L* is the edge length. These are only estimates to get the user started. In the QuickSolver, the user can scale the ESPET estimated number of emission sites through a scaling factor, where the default scaling factor is 1.

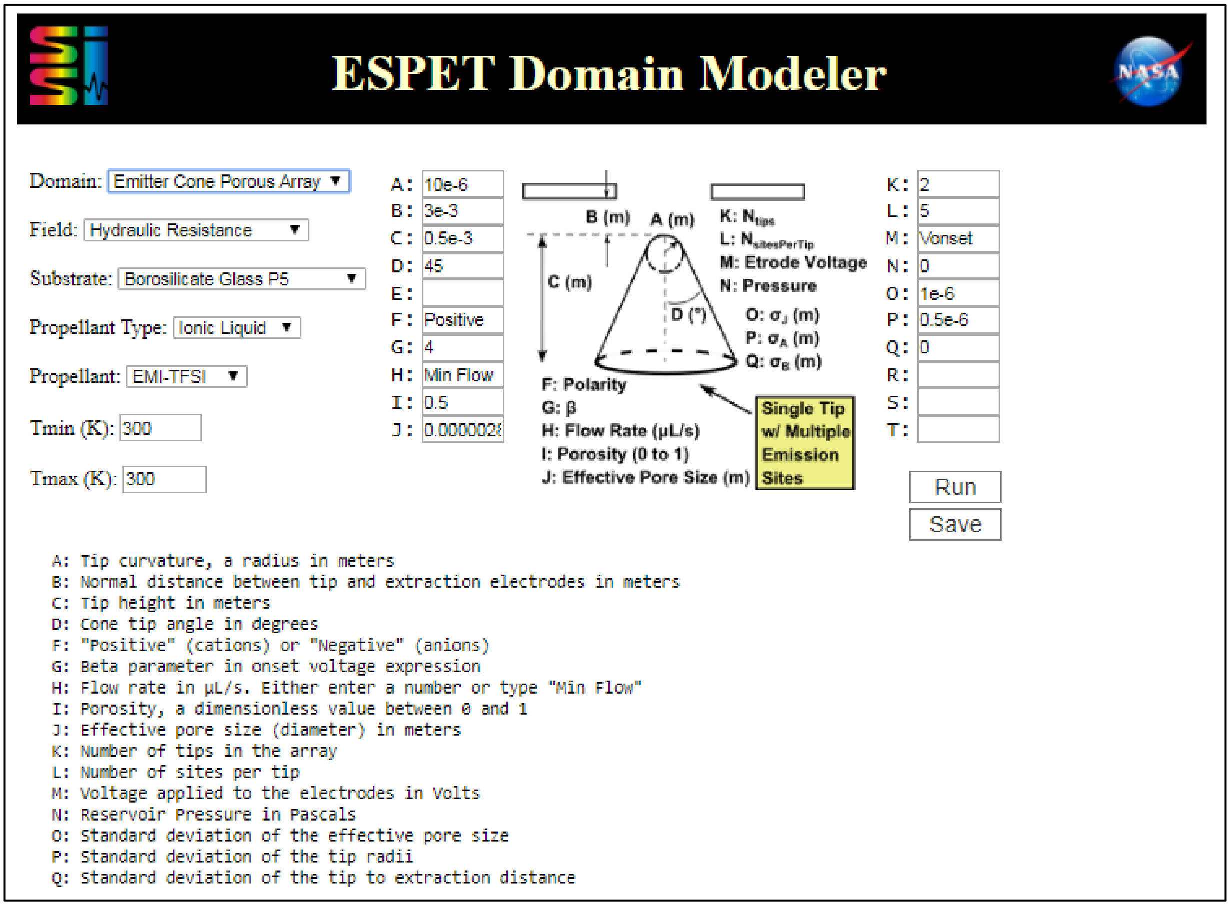

Domain: Emitter Cone Porous Array ▼
Field: Hydraulic Resistance ▼
Substrate: Borosilicate Glass P5 ▼
Propellant Type: Ionic Liquid ▼
Propellant: EMI-TFSI ▼
Tmin (K): 300
Tmax (K): 300

A: 10e-6
B: 3e-3
C: 0.5e-3
D: 45
E:
F: Positive
G: 4
H: Min Flow
I: 0.5
J: 0.000002

K: 2
L: 5
M: Vonset
N: 0
O: 1e-6
P: 0.5e-6
Q: 0
R:
S:
T:

```
A: Tip curvature, a radius in meters
B: Normal distance between tip and extraction electrodes in meters
C: Tip height in meters
D: Cone tip angle in degrees
F: "Positive" (cations) or "Negative" (anions)
G: Beta parameter in onset voltage expression
H: Flow rate in µL/s. Either enter a number or type "Min Flow"
I: Porosity, a dimensionless value between 0 and 1
J: Effective pore size (diameter) in meters
K: Number of tips in the array
L: Number of sites per tip
M: Voltage applied to the electrodes in Volts
N: Reservoir Pressure in Pascals
O: Standard deviation of the effective pore size
P: Standard deviation of the tip radii
Q: Standard deviation of the tip to extraction distance
```

Figure 2.21. Screen capture of porous cone emitter array domain model.

2.3 Network Solver

Two ESPET 1.0 options exist for the network solver. In the first we use SPICE electric circuit simulator software to compute the network solution with components produced by the ESPET domain modeler and in the second, simple three-component networks consisting of a reservoir, a feed system and a single or an array of emitters are solved with a QuickSolver fully integrated in the ESPET software. The SPICE solution allows for sophisticated networks including time-dependent solutions, while the QuickSolver has the advantage of rapid solutions without the requirement of network design, easy implementation of effects due to tolerances, and instant analysis of temperature effects.

2.3.1 SPICE Network Solver

The SPICE network solver produces a solution for the microfluidic circuit for a given list of domains, their connectivity and microfluidic properties including hydraulic resistances, compliances, Laplace (capillary force) pressure differentials, or active pressure sources. Theoretically, there is no limit to the complexity that the network can have. However, complex networks require considerable skill with the SPICE graphical user interface. We recommend the freely downloadable LTSpice software from Linear Technologies [*LTspice*, 2017].

2.3.1.1 SPICE Interface

2.3.1.1.1 General Interface

When the save button is pressed in the Domain Modeler, the active configuration is saved to the internet session in the same way that online shoppers have their choices saved to a virtual cart. When all components have been saved, the user activates a link under “Manage, export and download saved models from the Component Selector/Download tool”. This leads to the Component Selector/Downloader (http://espet.spectral.com/espet/domainModeler/espsp), where the configurations are displayed alongside checkboxes for a final selection before export. This selection screen is shown in Figure 2.22. When the “SPICE Export” button is pressed, a SPICE model is generated for each selected component. The models are then downloaded through the web browser to the user download folder as a single zipped file. The components then need to be extracted to a folder where SPICE can find them when pointing to a folder containing a component library. With LTSpice, this is best accomplished by generated a new schematic and saving it to a specific folder. This folder will then be an option for component libraries and should be used for the ESPET generated components.

Figure 2.23 shows an LTSpice GUI screenshot with a circuit wired using the three components generated by the domain modeler and listed in the Component Selecor/Downloader in Figure 2.22. The circuit represents a system with a propellant reservoir, a capillary conduit and a capillary emitter. While the capillary conduit is associated with a hydraulic resistance computed by the domain modeler for the selected propellant and temperature, the emitter model is far more complex due to the necessity of reconciling both the microfluidic and electric aspects of the Taylor cone electrohydrodynamics.

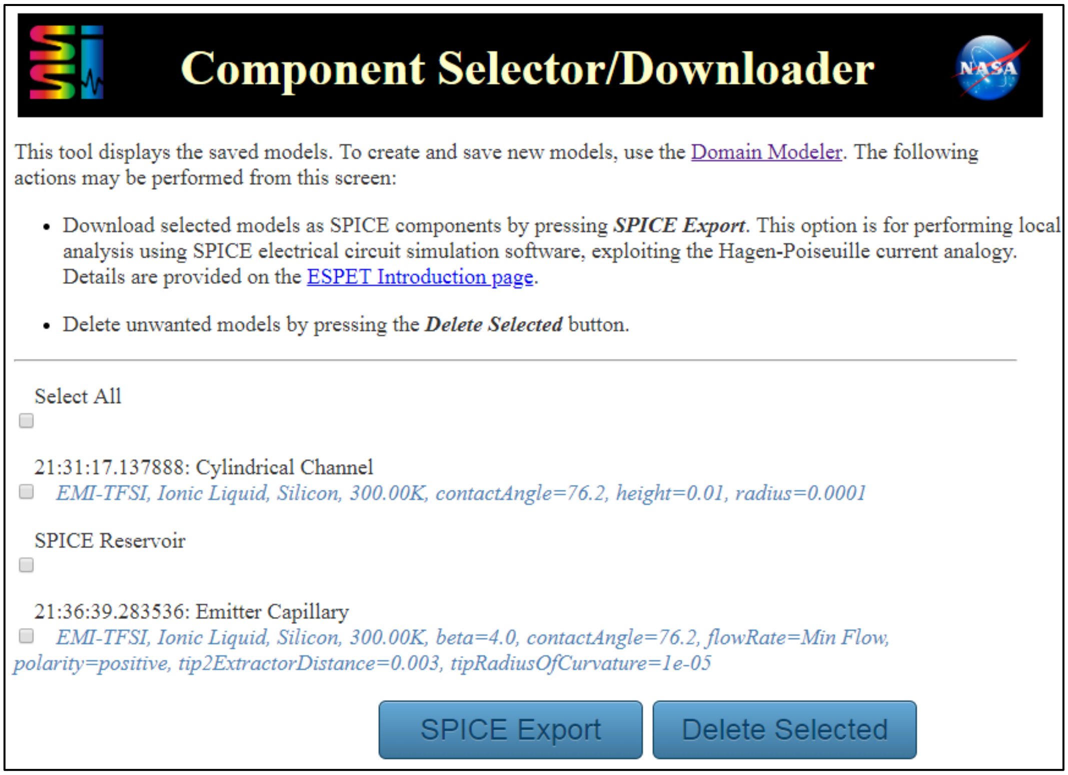

This tool displays the saved models. To create and save new models, use the Domain Modeler. The following actions may be performed from this screen:

- Download selected models as SPICE components by pressing ***SPICE Export***. This option is for performing local analysis using SPICE electrical circuit simulation software, exploiting the Hagen-Poiseuille current analogy. Details are provided on the ESPET Introduction page.
- Delete unwanted models by pressing the ***Delete Selected*** button.

Select All
☐

21:31:17.137888: Cylindrical Channel
☐ *EMI-TFSI, Ionic Liquid, Silicon, 300.00K, contactAngle=76.2, height=0.01, radius=0.0001*

SPICE Reservoir
☐

21:36:39.283536: Emitter Capillary
☐ *EMI-TFSI, Ionic Liquid, Silicon, 300.00K, beta=4.0, contactAngle=76.2, flowRate=Min Flow, polarity=positive, tip2ExtractorDistance=0.003, tipRadiusOfCurvature=1e-05*

Figure 2.22. SPICE Component Selector/Downloader screenshot.

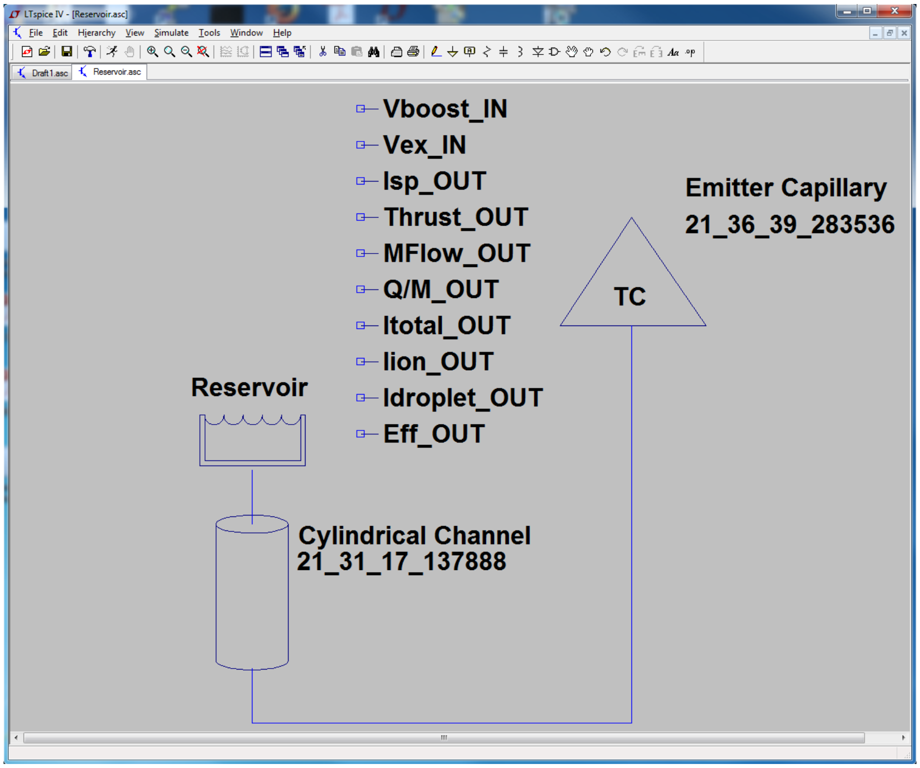

Figure 2.23. Screen snapshot of LTSpice window displaying simple electrospray propulsion system “wired” using components listed in Figure 2.134.

2.3.1.1.2 Basic Emitter Components

Here we describe the development of the methodology for setting up a Taylor cone emitter component in the SPICE network solver. The key challenge is to have SPICE solve a microfluidic circuit, where the Ohmic current and voltage are replaced by volume flow rate and pressure, and to simultaneously solve for the output electrical current as a function of an applied extraction voltage and the network microfluidic volume flow rate. We demonstrate the combined microfluidic/electrohydrodynamic solution on a simple actively pressurized capillary system.

Our approach is to program custom physics directly into the components using the arbitrary waveform generator capability of SPICE. This approach provides for flexibility and the means to rapidly upgrade the physics. Using this waveform generator technique, we designed a flow-controlled Taylor cone and incorporated the cone-jet physics detailed in Section 2.2.2.5. We then succeeded in introducing this Taylor Cone component into a SPICE network solver that computes estimates of mass flow, thrust, I_{sp}, and q/m within a network. Thus, the component provides directly the performance output of an individual emitter.

Figure 2.24 shows a schematic of our first simple actively pressurized capillary Taylor cone component as it appears in the SPICE schematic. The component represents an actively pressurized capillary emitter in a high, pure droplet emission mode. It is terminated at ground, which represents the reference pressure of vacuum. There are 8 tabs to this component consisting of 3 inputs and 5 outputs. The inputs consist of the circuit flow input on the triangular Taylor cone (TC) component symbol, and the extraction and accelerator (boost) voltages. The component outputs consist of I_{sp}, electrical output current, thrust, mass flow and spray q/m.

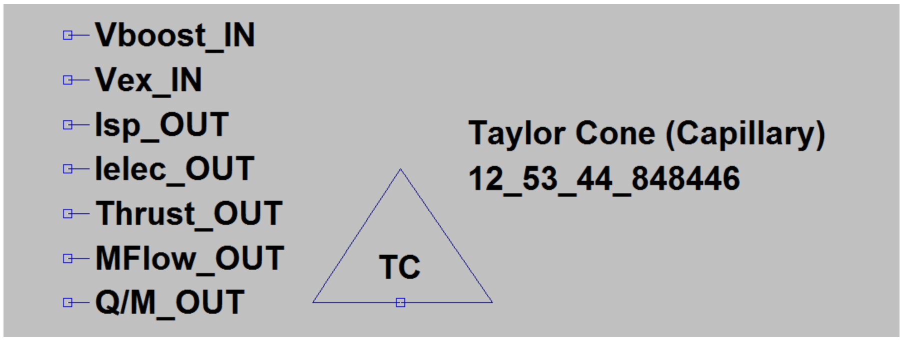

Figure 2.24. First Taylor cone component developed for SPICE network solver. The component represents an actively pressurized capillary emitter in a high, pure droplet emission mode.

In Figure 2.25, we demonstrate the use of this component on the simplest possible ESP circuit in which we model a single capillary electrospray thruster similar to the one used on the ST-7 Lisa Pathfinder mission. The actively pressurized thruster operates at a single extraction voltage at which Taylor cone stability and emission is optimized. Thrust is adjusted with the acceleration voltage and the mass flow as controlled by the pressure applied to the propellant reservoir. The Taylor cone is modeled in an on-off mode, where the spray properties are constant with extraction voltage above the onset voltage computed for the capillary/extractor geometry defined in the domain modeler (right side of figure). We apply a negative 200 V boost voltage which represents the estimated energy lost by droplets in the jet.

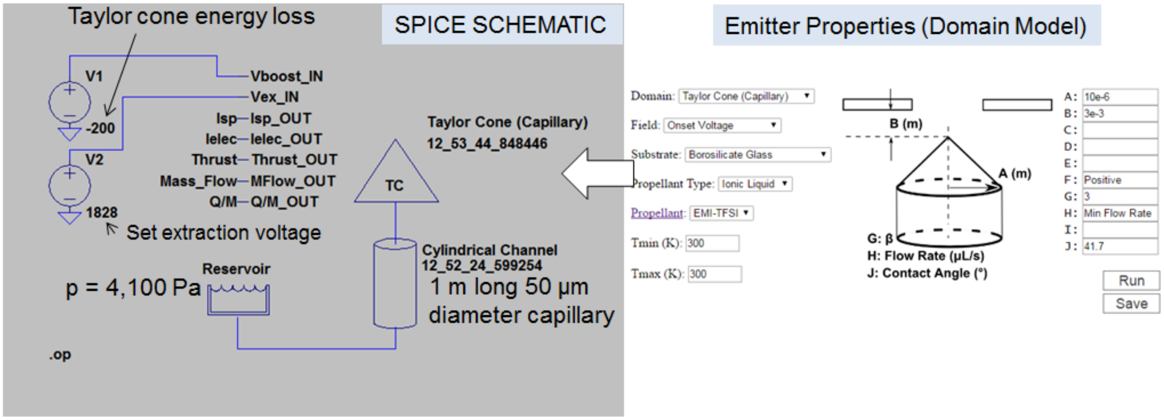

Domain: Taylor Cone (Capillary)
Field: Onset Voltage
Substrate: Borosilicate Glass
Propellant Type: Ionic Liquid
Propellant: EMI-TFSI
Tmin (K): 300
Tmax (K): 300

A: 10e-6
B: 3e-3
C:
D:
E:
F: Positive
G: 3
H: Min Flow Rate
I:
J: 41.7

Figure 2.25. Single capillary emitter thruster schematic in SPICE and domain modeler screenshot showing values used to generate the component.

Figure 2.25 also shows a screenshot of the domain modeler with inputs that produced the SPICE component. The voltages are applied to the inputs using existing voltage source components. The feed system consists of custom components for a reservoir and a capillary. These components are also generated with the domain modeler that is linked to the microfluidics database. Alternatively, the reservoir can be replaced by a voltage source, which is the equivalent of a pressure source in the microfluidic realm. For both options, the user enters pressure in units of Pascal.

Table 2.7 shows the output results for two input pressures that produced mass flows equivalent to those used when testing the Busek capillary colloid thruster with an EMI-TFSI propellant [*Gamero-Castaño and Hruby*, 2001]. The pressure was adjusted to match the quoted mass flow by Gamero-Castaño and Hruby who did not specify accurately the length of their capillary feed system. The only substantial discrepancy is observed in the predicted thruster efficiency, where the ESPET inefficiency is only based on the 200 V loss of extraction voltage due to Ohmic losses in the jet. This 200 V value is a typical value as seen in past work by the principal investigator [*Chiu, et al.*, 2005; *Luedtke, et al.*, 2008], but not necessarily the true energy loss of the accelerated droplets at the specific high current conditions. Additional inefficiency is introduced through beam divergence, fragmentation of ions in the acceleration region, and through the polydisperse inefficiency. The higher experimental inefficiency is consistent with the lower thrust and I_{sp} observed in the experiments. Overall, however, the agreement produced by this simplest of Taylor cone component model is very satisfactory.

Table 2.7. Comparison between ESPET predictions and Busek measurements for EMI-TFSI propelled single capillary thruster.

Property	ESPET	Busek	ESPET	Busek
Pressure (Pa)	4,100		1,600	
Thrust (μN)	0.78	0.63	0.38	0.35
Isp (s)	147	126	185	171
q/m (C/kg)	636	625	1008	820
Mass flow (mg/s)	0.54	0.54	0.21	0.21
I (mA)	0.34	0.31	0.21	0.22
Extraction Voltage (V)	1,828	1,828	1,828	1,828
Efficiency (%)	89	68	89	68

The user has access to all of SPICE's output modes. Figure 2.26 shows the capture of an LTSpice output plot showing the extraction voltage to thrust relationship. The voltages on the output pins of the Taylor cone component (I_{sp}, thrust, etc.) should be interpreted as having the same physical units as in the domain modeler. So, the thrust in Figure 2.26, although displayed in volts, represents a force in Newtons. The plot provides the expected behavior, with a jump to full mass flow at ~1.4 kV, and then a rise due to the increasing acceleration of the charged droplets. The maximum thrust at 2 kV extraction is 800 nN.

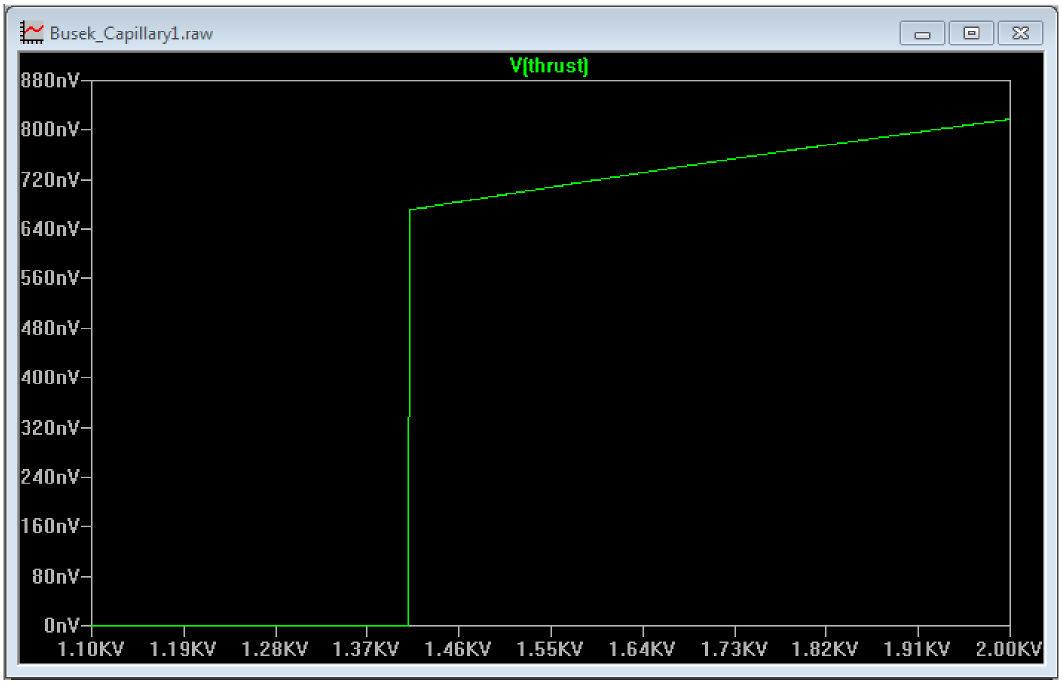

Figure 2.26. LTSpice output for a thrust versus extraction voltage scan for the 4,100 Pa reservoir pressure experiment (Table 2.7). Actual units of thrust are in nN (not nV).

The capillary, flow-controlled Taylor cone component model above has since been upgraded to include an ion evaporation model detailed in Section 2.2.2.5. This makes the component applicable to both high and low flow rate limits. The enhanced component is shown as it appears in an LTSpice schematic in Figure 2.27. The component has the same number of inputs (3), but now includes three output currents, I_{total}, I_{ion}, and $I_{droplet}$. In the process, we have also changed the Taylor cone models in the domain model utility to require specification of the emission polarity. The output current thus correctly reflects the polarity of the emitted charges.

The component in Figure 2.27 is attached to a constant current source (I1) with flow units of µl/s. Figure 2.28 shows the network solver output of the evolution of total spray current while scanning the flow rate to a capillary emitter with EMI-TFSI propellant. The lower flow rate limit is close to the stability limit and the increase with decreasing flow is due to ion evaporation. The units for current are nA (although LTSpice notes it as nV) and the units for flow is µl/s (10^{-9} m^3/s), which appears as µA in the output. Since Figure 2.27 was created, the polydisperse efficiency was added as an additional output of the circuit.

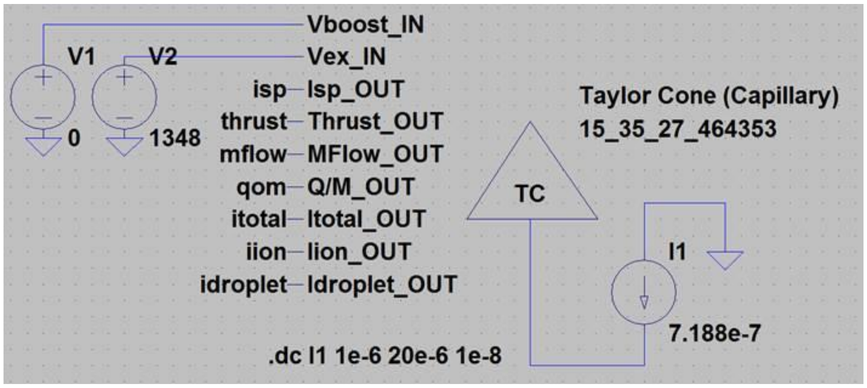

Figure 2.27. Revised actively pressurized capillary emitter component for both high and low flow rates.

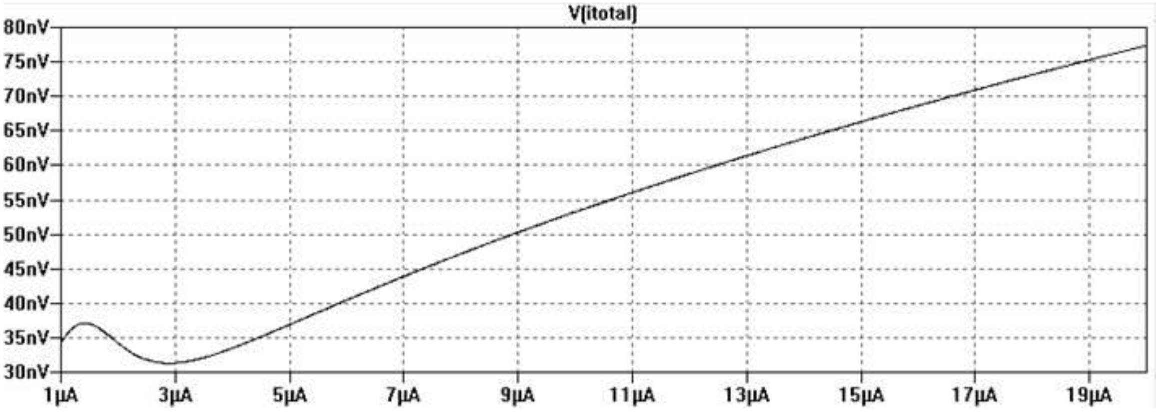

Figure 2.28. LTSPICE output for emitter current versus flow rate for a capillary emitter with EMI-TFSI. Units of current are in nA and of flow rate is in µl/s.

Considerable programming was necessary in order to have the Domain Modeler produce a complex Taylor cone component. Each component consists of two text files with extensions .asy and .asc. Figure 2.29 shows a screen shot of the internal schematic of the Taylor cone component shown in Figure 2.27. The outputs and inputs consist of voltage sources. Parameters and analytical functions are entered as text in the component. This schematic is represented by a text file following SPICE logic, where the parameters and function are entered through a 'TEXT' directive.

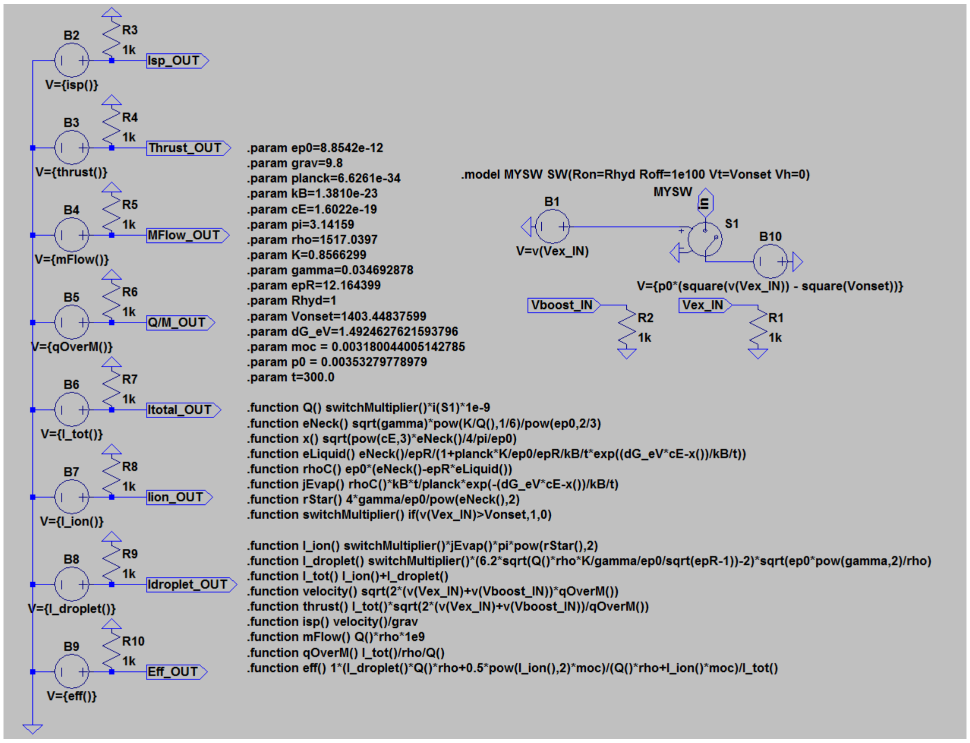

```
.model MYSW SW(Ron=Rhyd Roff=1e100 Vt=Vonset Vh=0)
```

```
.param ep0=8.8542e-12
.param grav=9.8
.param planck=6.6261e-34
.param kB=1.3810e-23
.param cE=1.6022e-19
.param pi=3.14159
.param rho=1517.0397
.param K=0.8566299
.param gamma=0.034692878
.param epR=12.164399
.param Rhyd=1
.param Vonset=1403.44837599
.param dG_eV=1.4924627621593796
.param moc = 0.003180044005142785
.param p0 = 0.00353279778979
.param t=300.0

.function Q() switchMultiplier()*i(S1)*1e-9
.function eNeck() sqrt(gamma)*pow(K/Q(),1/6)/pow(ep0,2/3)
.function x() sqrt(pow(cE,3)*eNeck()/4/pi/ep0)
.function eLiquid() eNeck()/epR/(1+planck*K/ep0/epR/kB/t*exp((dG_eV*cE-x())/kB/t))
.function rhoC() ep0*(eNeck()-epR*eLiquid())
.function jEvap() rhoC()*kB*t/planck*exp(-(dG_eV*cE-x())/kB/t)
.function rStar() 4*gamma/ep0/pow(eNeck(),2)
.function switchMultiplier() if(v(Vex_IN)>Vonset,1,0)

.function I_ion() switchMultiplier()*jEvap()*pi*pow(rStar(),2)
.function I_droplet() switchMultiplier()*(6.2*sqrt(Q()*rho*K/gamma/ep0/sqrt(epR-1))-2)*sqrt(ep0*pow(gamma,2)/rho)
.function I_tot() I_ion()+I_droplet()
.function velocity() sqrt(2*(v(Vex_IN)+v(Vboost_IN))*qOverM())
.function thrust() I_tot()*sqrt(2*(v(Vex_IN)+v(Vboost_IN))/qOverM())
.function isp() velocity()/grav
.function mFlow() Q()*rho*1e9
.function qOverM() I_tot()/rho/Q()
.function eff() 1*(I_droplet()*Q()*rho+0.5*pow(I_ion(),2)*moc)/(Q()*rho+I_ion()*moc)/I_tot()
```

Figure 2.29. Schematic of Taylor cone component shown in Figure 2.139.

2.3.1.1.3 LTSpice Monte Carlo Analysis

The use can apply the LTSpice Monte Carlo capability to an electrospray network. Here we demonstrate this on a capillary array where component properties are specified with variances. Figure 2.30 shows a three-emitter array. It would have been trivial to add any number of additional emitters, however, the chart would have been less legible. In Figure 2.30 we show the total thrust and Isp of the system as a function of the acceleration voltage. The extraction voltage is held at a fixed value of 1,828 V, a value where we assume stable Taylor cone operation. The system is operated at a 4,100 Pa reservoir pressure with a feed hydraulic resistance of 1.15×10^{17} Pa/m^3. The acceleration voltage is scanned from 0 to 500 V, while keeping the extraction voltage constant at 1,828 V. We assume a -200 V potential drop in the jet.

ESPET is designed so component parameters can be associated with tolerances, and the actual parameter value is then set through a random number generator reflecting the 1σ tolerance. To demonstrate this, we associate the hydraulic resistances of the feed capillaries in the network of Figure 2.30 with a 10% tolerance. The user can then choose a number of Monte Carlo “trajectories” to compute the distribution of possible performance outcomes. In Figure 2.31 we show total thrust and I_{sp} and in Figure 2.32, we show the thrust versus acceleration voltage curves of the three individual emitters in Figure 2.30 for a single trajectory where the hydraulic resistance of each capillary was randomly selected once. The figure shows that the thrust of individual emitters vary by approximately 10%.

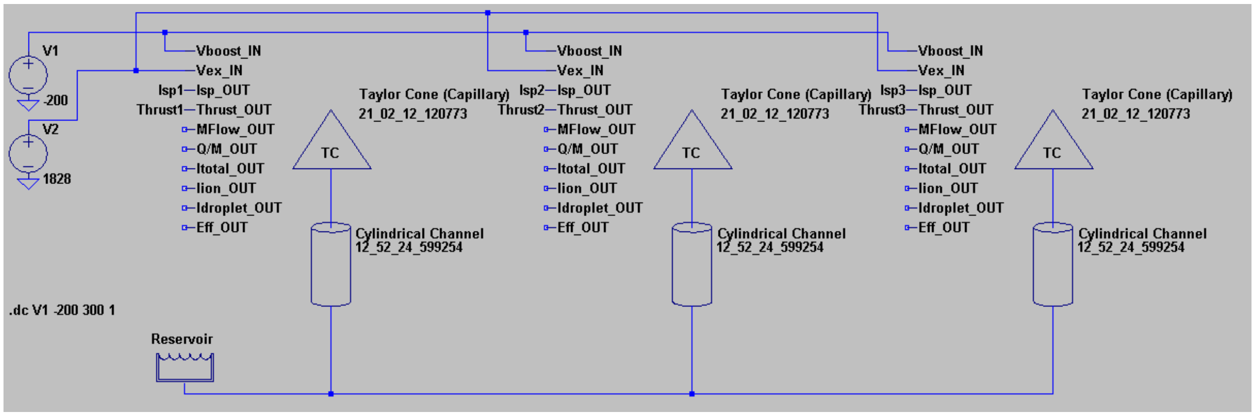

Figure 2.30. Schematic of three emitter array microfluidic network.

In addition to a Monte Carlo analysis, LTspice can be used to create a “worst-case” analysis, where the network performance is computed at the extremes of component values specified with a tolerance. This provides for a more direct way of extracting quantitative information on the range of outputs of emitter components.

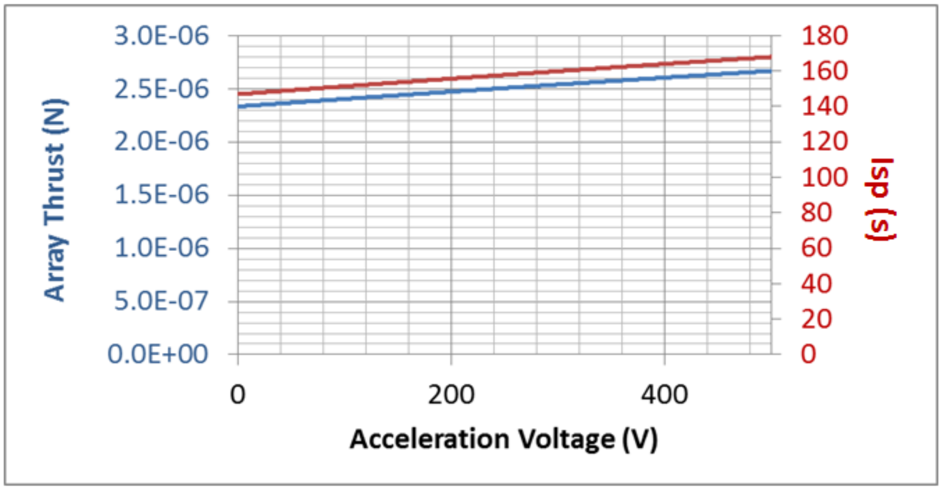

Figure 2.31. Total thrust and I_{sp} versus acceleration (boost) voltage for 3 emitter array shown in Figure 2.30.

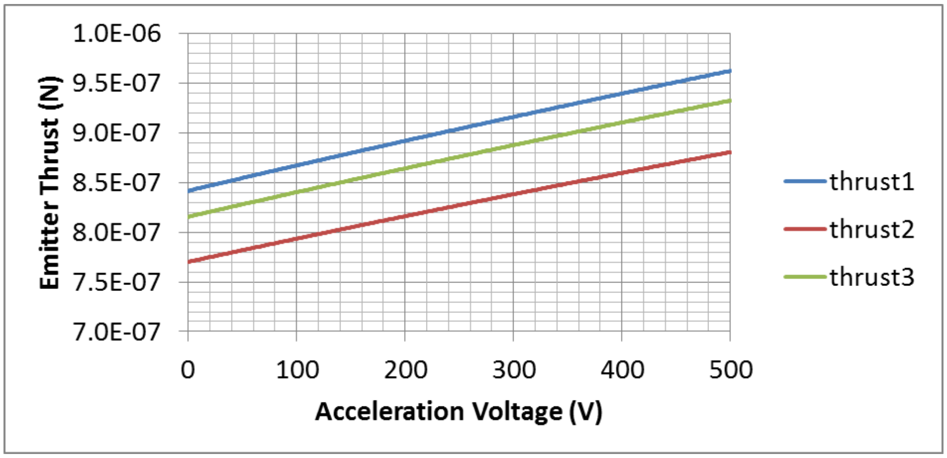

Figure 2.32. Results from an LTspice Monte Carlo run of the microfluidic network in Figure 2.30.

2.3.1.1.4 Porous Emitter Array Component Model for SPICE

The Domain Modeler produces components that with every execution have slightly different extractor distances, tip curvatures, and pore sizes in accordance with the user-specified variances. When the SPICE component is downloaded from the Domain Modeler, those properties are frozen. In other words, every time a particular porous emitter Taylor Cone component is simulated in SPICE, the output will be the same as long as the circuit schematic doesn't change. For a porous tip array, the user has the option of selecting a single tip with multiple emission sites, or an array of tips each with multiple emission sites. The former case provides the option of different feed systems for each emitter as "wired" in SPICE, while the latter assumes the feed systems is identical for all tips of the array. The porous edge emitter is for a single edge and multiple emission sites, each site associated with a separate curvature and pore size based on a specified standard deviation.

When a Taylor Array is downloaded from the Domain Modeler, the domain model SPICE files (*.asc and *.asy) are accompanied by three "piecewise linear function" (PWL) files (*CR_short.txt, onsetVoltage.txt* and *p0_allIndices.txt*) that contain arrays derived from the radii and extractor distances for C_R, V_0 and p_0. The generation of these outputs ensures that the majority of the computational load can be handled beforehand in the Domain Modeler. The extraction voltage, however, is set in SPICE, and there is, therefore, a limit to how much can be precalculated by the Domain Modeler. SPICE wasn't designed to evaluate sophisticated physical models such as the theory in the previous section. SPICE is an electrical circuit simulator and doesn't have vectorized arithmetic, array mathematics or even general for-loops. Here we describe a few tricks and associated compromises which allow SPICE to solve for such an array of emission sites while scanning the extraction voltage to produce I-V data.

Each emission site in the emission site array (or grid) has different properties and must be evaluated independently. We regard the properties of each emission site as voltages in time-dependent waveforms, which are a SPICE feature. The total simulated time is the number of emission sites times the number of discrete extraction voltages under evaluation. The number of entries in each waveform file is equal to the total number of emission sites in the array (or grid). The waveform must therefore be repeated for each voltage, accomplished by specifying an optional parameter in the SPICE file-import command:

PWL time_scale_factor={dt()} repeat for {Nvoltages} (file=onsetVoltage.txt) endrepeat **(2.59)**

where *dt* is a time interval. The import line reads the onset voltages from the specified file produced by the domain modeler and repeats the waveform Nvoltages times. The waveform files have both x (time) and y values, and the time values are scaled by *dt* on import. Since a time-dependent signal is processed, SPICE is run in transient analysis mode and the output plots are functions of time. However, using a special scaling technique, we can make it seem as though the x-axis is displaying voltage instead of time. Along with the number of discrete extraction voltages (*Nvoltages*), the SPICE user specifies a maximum extraction voltage, *Vmax*. To show voltage on the x-axis, we define a sampling time interval of

*dt = Vmax/(Nvoltages*Ntips*NsitesPerTip-1)* **(2.60)**

For the scaling to work as intended, the Domain Modeler must have times that start at 1 second and that are incremented by 1s for each sample. Note that there are a few limitations of this technique. 1) Although we can alter the numbers to appear to be voltages instead of times, we cannot change the unit of "s" on the x-axis. 2) It is not possible to specify a minimum value of extraction voltages; this value is inherently zero. This limitation is due to the fact that SPICE time plots are relative, always beginning at zero regardless of the times in the waveform files or the start time for the data recording. 3) The final plots should have *Nvoltages* number of points, but in fact they will have *Ntips*NsitesPerTip*Nvoltages* number of points. This requires some special interpretation on the part of the user. Specifically, only the last value in any Ntips*NsitesPerTip grouping has the meaningful final result. Figure 2.33 illustrates this point with the final result for each extraction voltage encircled. The scan is from 0 to 1 kV, which on the SPICE GUI appears as seconds. The current is shown as a voltage (actual unit is mA). Here we note that all output data displayed in SPICE are readily exported where it can be processed separately.

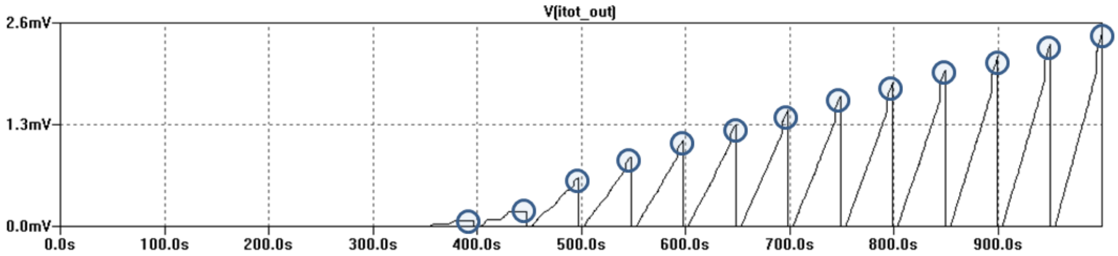

Figure 2.33. SPICE plot for 20 discrete extraction voltages from 0 to 1 kV. The user must interpret the plot as having meaningful values only at the last element of each integration block; those values have been encircled. The x axis provides the extraction voltage in Volts (not seconds) and the y axis provides the total current in mA (not mV).

Most porous emitter properties are the sums of the contributions of the individual emission sites. For example, to calculate total mass flow, it is necessary to add the calculated flow for each individual emission site. SPICE does not have a sum function for waveforms. Instead, it has a signal integrator. Integration occurs for each discrete extraction voltage and resets when the next voltage is encountered. Figure 2.34 shows the integration and triggering for a basic example.

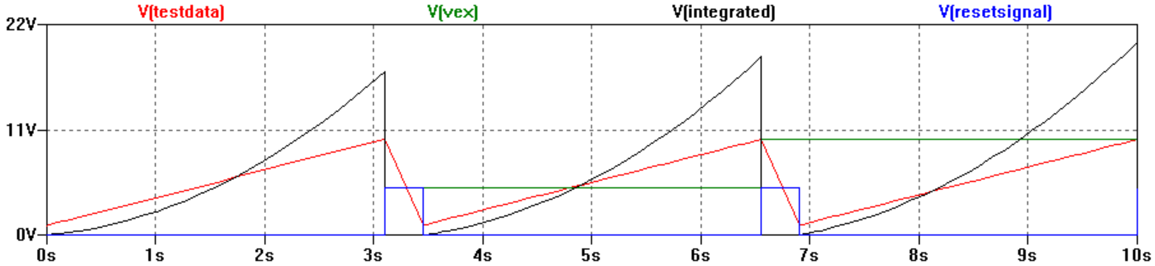

Figure 2.34. An illustration of how the extraction voltage is stepped and how the signal integrator is reset. There are three discrete extraction voltages from 0 to 10 V, plotted in green. The testdata (red signal) is integrated (black signal), with the integrator resetting in accordance with the blue reset signal. In this illustrative test example, the integrated signal is also a function of Vex (Vintegrated = integratedValue+0.1*Vex), which is why the integrated result reaches successively higher peaks. The duration of the reset pulse is the smallest resolvable time increment, *dt*. The width of each of the three integration periods is 10**dt* because this particular porous emitter has 10 emission sites.

The extraction voltage step in Figure 2.34 (5V) is constrained by our method for getting voltage values on the x-axis,

$$dV = Vmax/(Nvoltages-1) \quad \textbf{(2.61)}$$

The reset trigger is generated by performing integer division on the global time variable of SPICE, creating a makeshift modulus function:

$$resetSignal = if(TIME-(Ntips*NsitesPerTip*dt())*int(TIME/(Ntips*NsitesPerTip*dt())) <dt(), 1, 0) \quad \textbf{(2.62)}$$

The extraction voltage waveform *Vex* was synthesized by exploiting the SPICE global time variable and the properties of integer division, similar to the reset trigger:

$$Vex = dV*INT(time/(dt*Ntips*NsitesPerTip)) \quad \textbf{(2.63)}$$

A small inaccuracy is introduced by SPICE integration because there is a difference between the desired summation of outputs and the signal integration performed by the SPICE integrator. Figure 2.35 shows three arbitrary points as stars. The summation should be the sum of the areas of the rectangles, *dt**P1 + *dt**P2 + *dt**P3, after which the property will be divided by *dt*. But, the signal integrator instead reports the area of the 5-sided polygon outlined in black. The desired area is larger by P1**dt*/2 + P3**dt*/2.

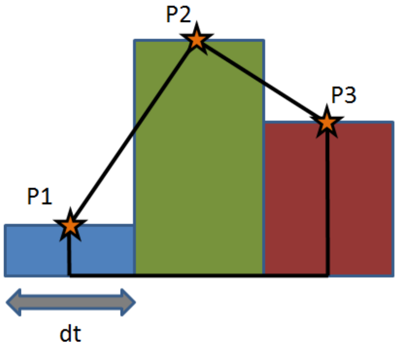

Figure 2.35. Two ways of integrating three points.

Figure 2.35 could represent the evaluation of a property for all emission sites at a particular extraction voltage, in other words, for dt*Ntips*NsitesPerTip seconds, where P1 would be the first emission site and Pn would be the last. The correction is applied by having two versions of the property signal, the original and one that has been delayed by Ntips*NsitesPerTip. Another periodic trigger is synthesized, to signal when point Pn is being processed. At that time, dt*P1 and dt*Pn are combined and added to the integration result. This correction is apparent in Figure 2.33, where, looking closely, you'll see a bias applied under each of the circled tips.

Finally, some of the algorithms of the model contain ratios that can have small values in the denominator for short time periods. This is particularly the case for I_{sp} and Q/M:

$$I_{sp} = thrust/massFlow/gravitationalConstant \tag{2.64}$$

$$Q/M = electricCurrent/massFlow/propellantDensity \tag{2.65}$$

When, for example, both the massFlow and thrust are virtually infinitesimal, but with thrust value larger than the massFlow value, there will be a spike that can compromise the Isp result. To produce cleaner output, the Isp and Q/M output waveforms are passed through an RC lowpass filter with a modest time constant of *dt*/2, shown in Figure 2.36.

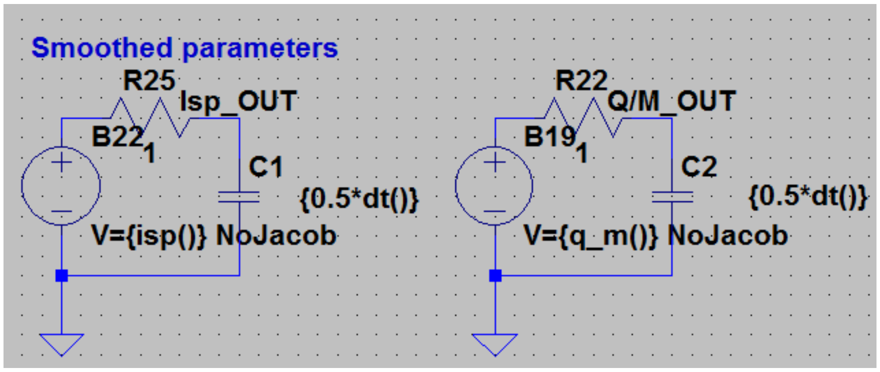

Figure 2.36. Low-pass filters to account for finite numerical precision, applied to I_{sp} and Q/M

The above demonstrates the complexity of programming intricate emitter structures with multiple emission sites into SPICE, and clearly exposes limitations in this approach. Future development of a complex network solver should, therefore, aspire to incorporating a numerical network solver integrated in ESPET. This realization led to the development of the three-component QuickSolver model where the network solution is trivial, but where more complex emitter models can be implemented and tested. Nevertheless, we believe this Section demonstrates how future developers of complex networks and solution can exploit SPICE capabilities even for complex emitter models.

2.3.2 QuickSolver

Key drawbacks when using the SPICE network solver are the time required for setting up a large array, complications associated with DC voltage scans for porous systems with stochastic distributions of pore sizes (see previous Section), and the requirement to generate new components for every specified temperature. The advantages of using SPICE are that there are no limits to the complexity of a microfluidic network, and that many features of SPICE can be used such as the graphing interface, the ability to apply tolerances and conduct Monte Carlo and worst-case scenario analysis of performance. The benchmarking examples investigated so far with ESPET, however, all can be described by simple three component electrospray systems consisting of a reservoir, a feed system and the emitter. For this purpose, we have decided to develop an alternative solver for simple three-component systems not requiring solutions for complex coupled fluidics. Figure 1.1 shows a schematic of the integration of this solver, referred to as "QuickSolver," in the overall ESPET architecture. The QuickSolver is accessed from the existing web user interface, and then is run from a separate GUI fully independent from the Domain Modeler.

The QuickSolver has several advantages. By accessing the database polynomials for the temperature dependence of propellant properties, it can instantaneously compute new performance parameters after changing the temperature. With the SPICE solver, a new network needs to be designed with new components since every component (feed and emitter) has a fixed temperature. The QuickSolver is also capable of incorporating tolerances by randomly choosing specific geometric parameters based on quoted tolerances.

The QuickSolver organization is similar to that of the other ESPET pages. The modeling equations have been segregated into a single file for easy reference and modification. The code is written and organized in a way that new emitter models can easily be introduced. By using Python and a 4-dimensional baseline matrix logic, we take advantage of extensive libraries such as routines for array data sorting. This is particularly important when treating multi-emission site emitters where the hydraulic resistance changes with the onset of new emission sites as described for porous emitters in Section 2.2.3.3. In this case, the emission sites need to be sorted according to their onset voltages, to allow for computing the hydraulic resistance of each emission site according to the number of active sites at a particular voltage.

2.4 <u>User Interface/Introduction Page</u>

2.4.1 Overview

The ESPET software is currently a web application hosted by Amazon Web Services (AWS), accessible through http:/espet.spectral.com. The public accesses an introductory page, a screenshot of which is shown in Figure 2.37. An account is necessary to access the Domain Modeler, the QuickSolver, and The Propellant Visualization Utility. SSI distributes authorized usernames and passwords to vetted customers. Clicking on "QuickSolver," "Domain Modeler" and "Propellant Visualization Utility" leads to the respective utility applications for domain modeling and the propellant property database.

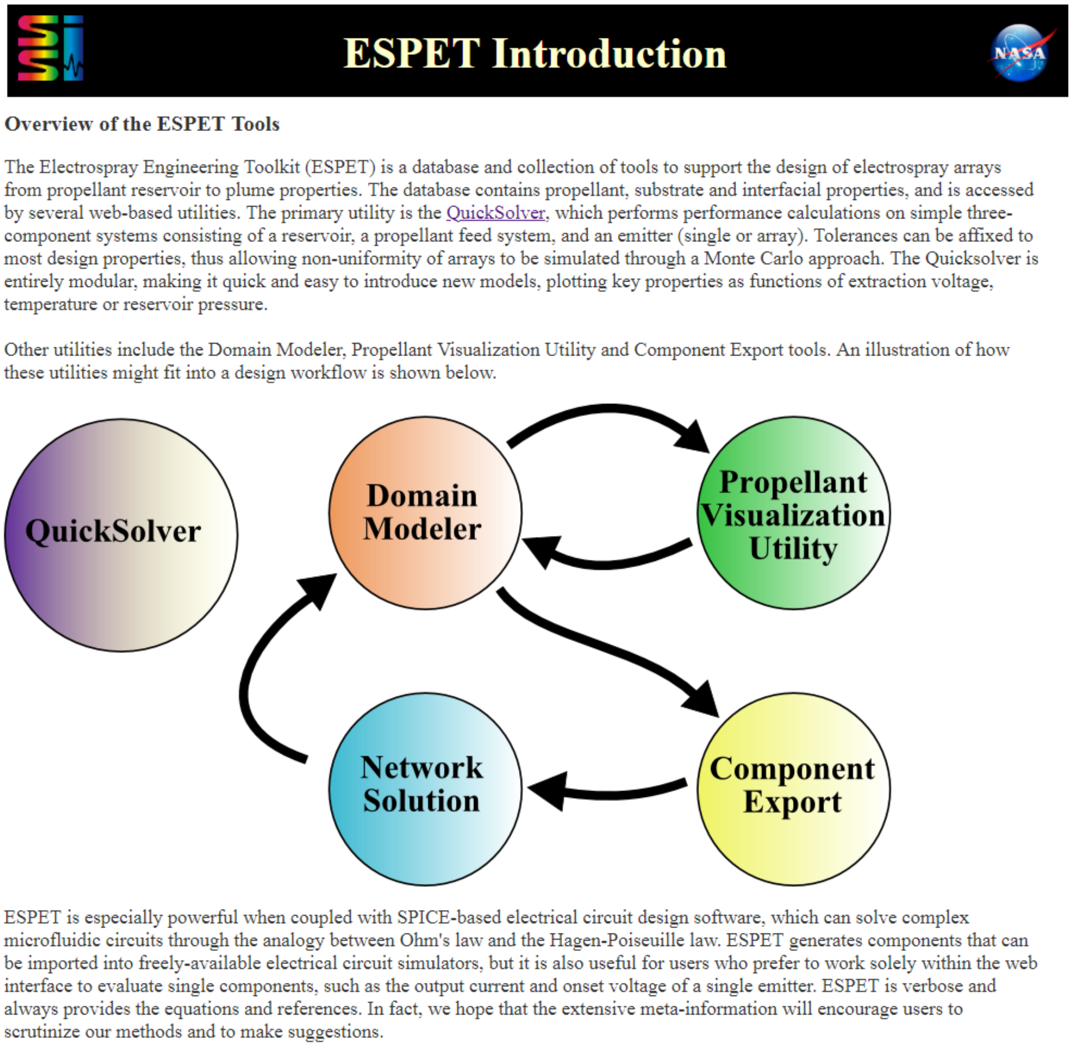

Overview of the ESPET Tools

The Electrospray Engineering Toolkit (ESPET) is a database and collection of tools to support the design of electrospray arrays from propellant reservoir to plume properties. The database contains propellant, substrate and interfacial properties, and is accessed by several web-based utilities. The primary utility is the QuickSolver, which performs performance calculations on simple three-component systems consisting of a reservoir, a propellant feed system, and an emitter (single or array). Tolerances can be affixed to most design properties, thus allowing non-uniformity of arrays to be simulated through a Monte Carlo approach. The Quicksolver is entirely modular, making it quick and easy to introduce new models, plotting key properties as functions of extraction voltage, temperature or reservoir pressure.

Other utilities include the Domain Modeler, Propellant Visualization Utility and Component Export tools. An illustration of how these utilities might fit into a design workflow is shown below.

ESPET is especially powerful when coupled with SPICE-based electrical circuit design software, which can solve complex microfluidic circuits through the analogy between Ohm's law and the Hagen-Poiseuille law. ESPET generates components that can be imported into freely-available electrical circuit simulators, but it is also useful for users who prefer to work solely within the web interface to evaluate single components, such as the output current and onset voltage of a single emitter. ESPET is verbose and always provides the equations and references. In fact, we hope that the extensive meta-information will encourage users to scrutinize our methods and to make suggestions.

Figure 2.37. ESPET Introductory web page providing access to the different ESPET tools.

2.4.2 Network Solution User Interface

Once components have been generated, the user can enter the Component Selector/Downloader page, where a listing of save components is presented. The user selects the components of choice and then exports them in the form of a zip file. The content of the zip file needs to be extracted to a folder where SPICE can load them as components. The QuickSolver is independent of the Domain Modeler and the user enters reservoir (pressure), feed and emitter parameters in the QuickSolver GUI shown in Figure 2.38. In the example below, we see the QuickSolver input section including an output chart for the selected field, the electric output current. The example is for an IL impregnated porous borosilicate system where the feed and emitter have different porosities. A critical feature for such a complex case is the ability to save the configuration by clicking on the “Save Config” button at the bottom right. This generates an XML file, which can then be reloaded by clicking “Load Config” and cutting and pasting the XML file content into the text window that pops up.

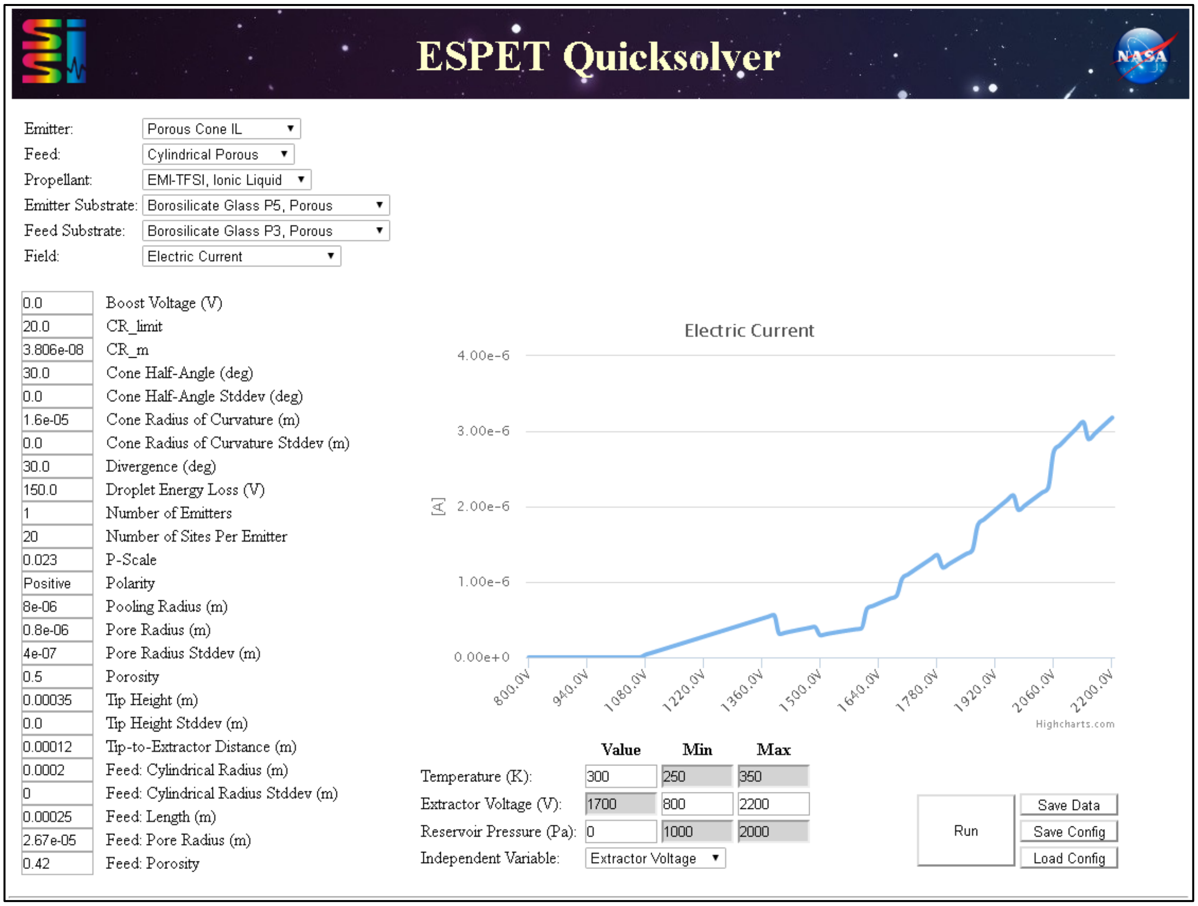

Emitter: Porous Cone IL
Feed: Cylindrical Porous
Propellant: EMI-TFSI, Ionic Liquid
Emitter Substrate: Borosilicate Glass P5, Porous
Feed Substrate: Borosilicate Glass P3, Porous
Field: Electric Current

0.0	Boost Voltage (V)
20.0	CR_limit
3.806e-08	CR_m
30.0	Cone Half-Angle (deg)
0.0	Cone Half-Angle Stddev (deg)
1.6e-05	Cone Radius of Curvature (m)
0.0	Cone Radius of Curvature Stddev (m)
30.0	Divergence (deg)
150.0	Droplet Energy Loss (V)
1	Number of Emitters
20	Number of Sites Per Emitter
0.023	P-Scale
Positive	Polarity
8e-06	Pooling Radius (m)
0.8e-06	Pore Radius (m)
4e-07	Pore Radius Stddev (m)
0.5	Porosity
0.00035	Tip Height (m)
0.0	Tip Height Stddev (m)
0.00012	Tip-to-Extractor Distance (m)
0.0002	Feed: Cylindrical Radius (m)
0	Feed: Cylindrical Radius Stddev (m)
0.00025	Feed: Length (m)
2.67e-05	Feed: Pore Radius (m)
0.42	Feed: Porosity

	Value	Min	Max
Temperature (K):	300	250	350
Extractor Voltage (V):	1700	800	2200
Reservoir Pressure (Pa):	0	1000	2000

Independent Variable: Extractor Voltage

Figure 2.38. QuickSolver screen shot.

In the bottom center of Figure 2.38, the user chooses the independent variable with choices between temperature, extractor voltage and reservoir pressure. For the active independent variable, the user selects a range of values to plot. Clicking the “Save Data” button exports a csv file with all of the available data listed in the “Field” menu versus the independent variable. In this case, the “Field” data plotted are: Electric current, mass flow, thrust, I_{sp}, mass flow, average C_R, number of active sites, and number of sites in pure-ionic mode. The user is also assisted by an appended graphic description of the selected emitter system with an explanation of some of the required parameters. This is shown in Figure 2.39 for the example above.

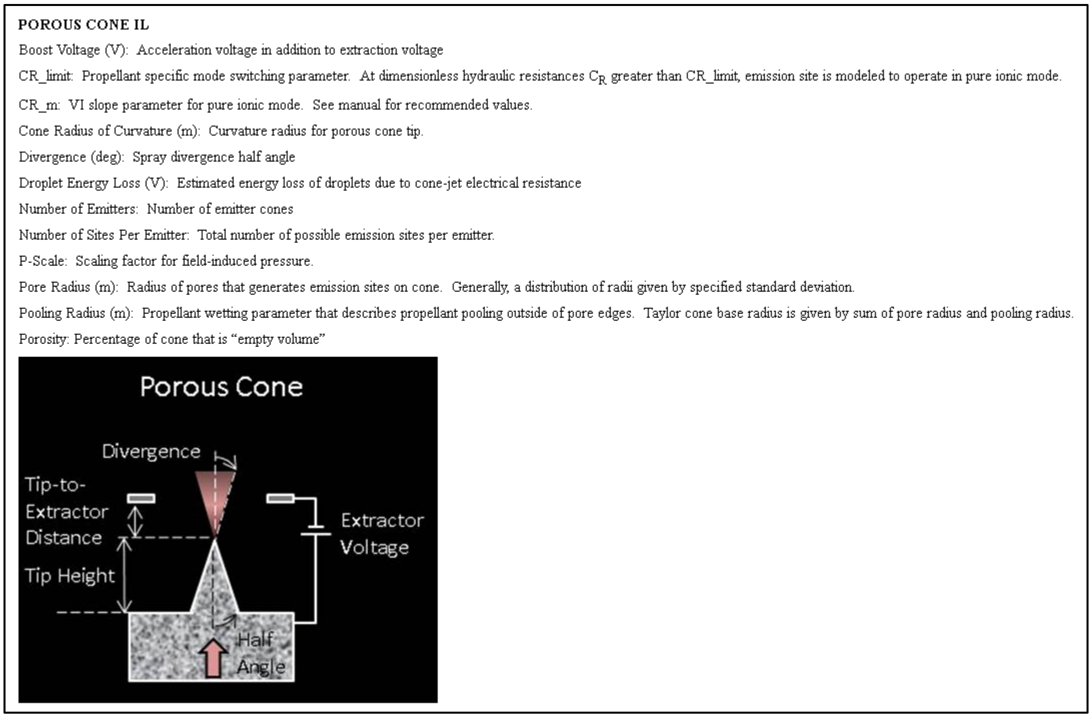

POROUS CONE IL

Boost Voltage (V): Acceleration voltage in addition to extraction voltage

CR_limit: Propellant specific mode switching parameter. At dimensionless hydraulic resistances C_R greater than CR_limit, emission site is modeled to operate in pure ionic mode.

CR_m: VI slope parameter for pure ionic mode. See manual for recommended values.

Cone Radius of Curvature (m): Curvature radius for porous cone tip.

Divergence (deg): Spray divergence half angle

Droplet Energy Loss (V): Estimated energy loss of droplets due to cone-jet electrical resistance

Number of Emitters: Number of emitter cones

Number of Sites Per Emitter: Total number of possible emission sites per emitter.

P-Scale: Scaling factor for field-induced pressure.

Pore Radius (m): Radius of pores that generates emission sites on cone. Generally, a distribution of radii given by specified standard deviation.

Pooling Radius (m): Propellant wetting parameter that describes propellant pooling outside of pore edges. Taylor cone base radius is given by sum of pore radius and pooling radius.

Porosity: Percentage of cone that is "empty volume"

Figure 2.39. QuickSolver description of porous ionic liquid inputs.

3. ESPET PERFORMANCE BASIS OF CONFIDENCE

In this section we compare ESPET outputs to reported experimental data. Since the models implemented in ESPET still require parameterization, we take the approach of adjusting these parameters in order to optimize the agreement with the observed performance. Most of the benchmarking was conducted using the QuickSolver. Given the ease with which models can be upgraded within the QuickSolver software structure, and the ease with which large arrays or emitters with a significant number of emission sites can be modeled, the QuickSolver physics has outpaced the development of the SPICE component physics. At the current stage of development, we recommend using the QuickSolver. However, further development of the SPICE concept is warranted for time-dependent problems, and for networks requiring components in addition to feed conduits and emitters (for example compliances). A SPICE solution is demonstrated in the first example. For all QuickSolver solutions, we list the XML input files in the Appendix A.

3.1 Passively Driven Capillary Array of Dandavino *et al*., Ionic Liquid Propellant

3.1.1 SPICE Solution

ESPET coupled with LTSpice was tested on results reported by the group of Shea at Ecole Polytechnique Federal de Lausanne (EPFL) using a micro-machined capillary array and the ionic liquid, EMI-BF4 [*Dandavino, et al.*, 2014]. A schematic of individual emitters is shown in Figure 3.1. The array has a total of 127 emitters. The paper provides all necessary details to model the array. The propellant was EMI-BF4 and the thruster array was operated passively, i.e., the reservoir pressure was zero, and the flow was induced by the electric field. We started with a comparison of average emitter performance reported by Dandavino *et al.* to the outputs of a SPICE circuit for a single emitter shown in Figure 3.2. The passive capillary emitter SPICE component did not include switching to a pure ionic regime (PIR). A later version of the Domain Modeler, however, allows entering this parameter directly into the component schematic. The physics of mode switching was developed and benchmarked with the much more flexible QuickSolver (see next Section).

Two feed components are shown in Figure 3.2. The overall feed hydraulic resistance is dominated by the emitter inner diameter which produces a much higher hydraulic resistance than the larger diameter capillary connecting the reservoir to the emitter section. The inner diameter of the emitter is quoted to be 7.9±0.5 µm. We adjusted the emitter extractor gap to match the onset voltage, and then adjusted a scaling factor, p_{scale}, in Eq. 2.36 to match the quoted mass flow. This resulted in $p_{scale} = 0.0085$.

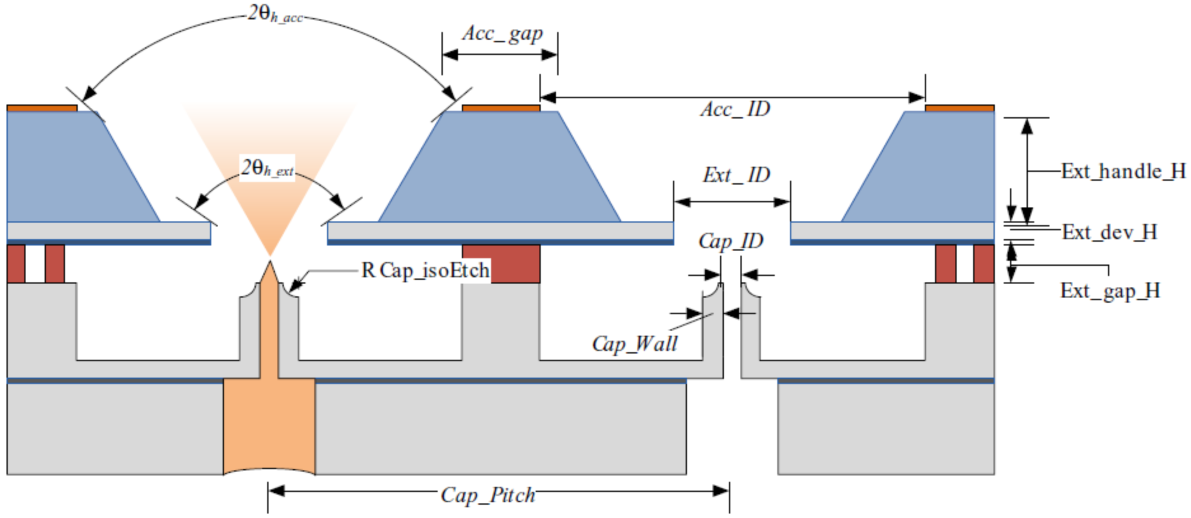

Figure 3.1. Schematic representation of capillary emitters constructed and tested by Dandavino [*Dandavino, et al.*, 2014].

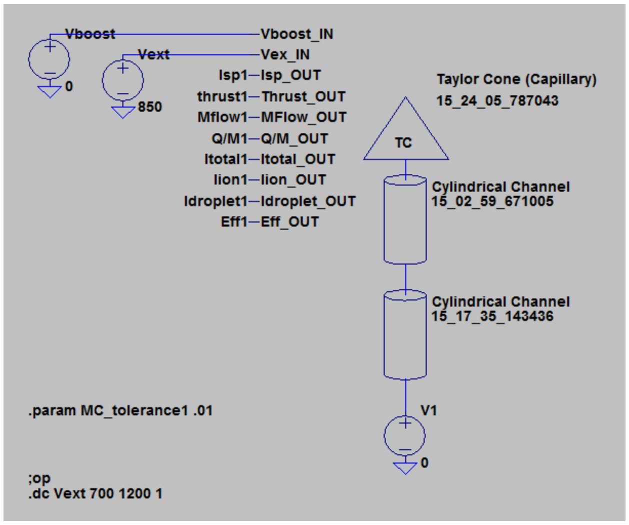

```
.param MC_tolerance1 .01

;op
.dc Vext 700 1200 1
```

Figure 3.2. SPICE schematic for a single emitter in the array developed by Dandavino [*Dandavino, et al.*, 2014].

The results are tabulated in Table 3.1 for an extraction voltage of 850 V, which is ~90 V above onset. The comparison to data reported by Dandavino *et al.* (EPFL) clearly shows that ESPET underestimates the current and q/m, while overestimating the efficiency, thrust, and I_{sp}. Figure 3.3 shows the modeled voltage-current behavior for droplets and ions based on the cone-jet model incorporated in the passive capillary emitter component. The dashed line identifies the voltage at which Dandavino *et al.* report their average emitter performance data. As is seen, this falls in the regime below the current maximum, where the ion current fraction is high, and where there is the possibility of switching to a pure ionic regime. We, therefore conclude that the reason for the discrepancy between the modeled and measured emitter performance is that some emitters operated in a cone-jet mode while others operated in the pure ionic regime. We postulate that such a non-uniformity of emission across the array is primarily caused by the tolerances assigned to the capillary inner diameter which determines the feed resistance. The hydraulic resistance is proportional to the inverse fourth power of the radius, thus a ~6% tolerance should have a marked effect on the distribution of hydraulic resistances.

Table 3.1. Comparison between emitter averages of the EPFL array and single emitter outputs computed by ESPET for cone-jet only mode (no emitters in pure-ionic regime). The extraction voltage was set to 850 V. f_{ion} is the ion current fraction.

Property	EPFL	ESPET
I (nA)	250	92.7
Thrust (nN)	16.5	23.7
I_{sp} (s)	474	678
$\dot{m}$ (kg/s)	3.55e-12	3.56e-12
q/m (C/kg)	70,423	26,020
Efficiency, η_T	0.18	0.29
Power, P (μW)	212	79
f_{ion}	0.95	0.57

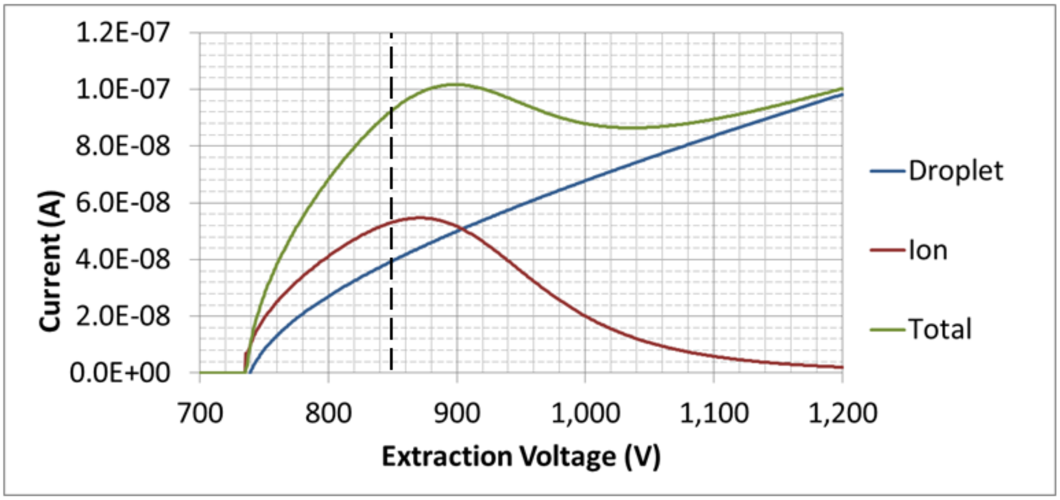

Figure 3.3. VI curves for ions and droplets computed with the circuit shown in Figure 3.2. Dashed line identifies extraction voltage at which performance parameters in Table 3.1 were computed.

Nevertheless, this case shows that the SPICE simulation was able to identify that a single capillary in the array of Dandavino *et al.* will operate in a borderline cone-jet regime where the physics as implemented in the ESPET component is no longer fully applicable, and pure-ionic regime may be reached by some emitters. The results would change significantly, if the model allowed the ion current to further increase with decreasing extraction voltage and volume flow rate. Here we note that the minimum Taylor cone sustaining mass flow rate of this propellant at room temperature conditions is ~10^{-12} kg/s at 850 V, only a factor of ~4 below the quoted average flow rate per emitter.

3.1.2 QuickSolver Solution

We compare the same results obtained by Dandavino *et al.* for the MEMS capillary array to QuickSolver results using the “Capillary IL” emitter model. Table 3.2 compares the emitter-averaged values at an extraction voltage of 850 V to the data listed by Dandavino and coworkers (EPFL). Figure 3.4 shows the comparison to the experimental VI curve of the array (total current). The computed red curve was computed for 127 emitters and is close to an average computed for a substantially larger number of emitters (>1,000). The shaded area reflects the QuickSolver solution space for a large number of 127 emitter runs. The statistics is entirely attributable to the variance of the emitter capillary radius, introduced by the tolerance listed in Table 3.3 along with other input parameters.

Table 3.2. Comparison between QuickSolver results and the laboratory measurements by Dandavino *et al.* for a 127 emitter capillary array operated on EMIMBF4. Single emitter averages are shown.

Property	**EPFL**	**ESPET**
I (nA)	250	246
Thrust (nN)	16.5	23.1
I_{sp} (s)	474	520
$\dot{m}$ (kg/s)	3.55e-12	4.54e-12
q/m (C/kg)	70,423	54,185
Efficiency, η_T	0.18	0.28
Power, P (µW)	212	209

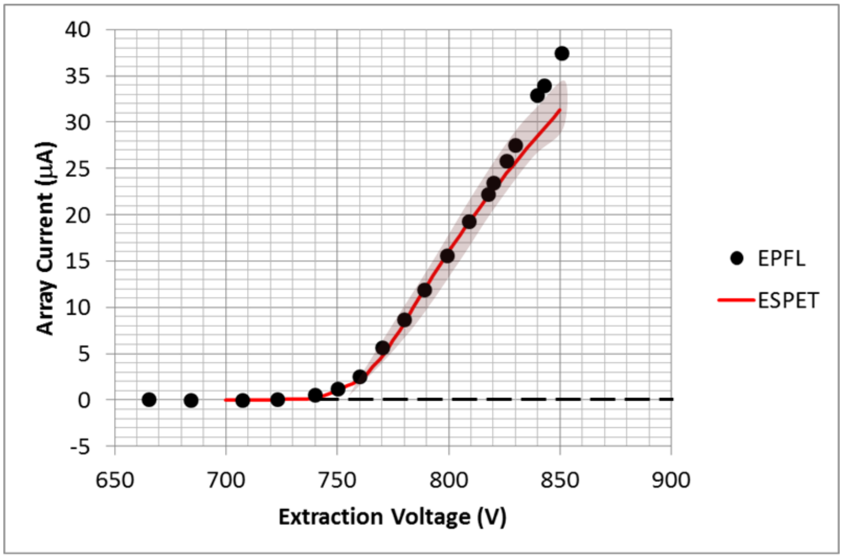

Figure 3.4. Comparison of VI total current for 127 capillary emitter array by Dandavino *et al.* (experimental data: EPFL) and ESPET QuickSolver results. Dashed area reflects the statistical variance introduced by emitter radius tolerance.

The critical benchmarking parameters are The C_R mode switching limit, p_{scale}, and ξ, the pure ionic model voltage-current slope parameter. These parameters were adjusted to optimize the comparison in Table 3.2. The pure ionic mode slope parameter ξ is set to $1.8\times10^{-8}\ \Omega^{-1}$ which is lower than what we find for other emitter models (~$3.8\times10^{-8}\ \Omega^{-1}$, see subsequent benchmarking). p_{scale} is higher than what we found in the SPICE model. In subsequent benchmarking efforts (see ensuing Sections), we no longer adjusted this value. The QuickSolver model predicts that 46% of emitters are in pure ionic mode. The remaining emitters are in mixed cone-jet mode. The full set of inputs leading to the results in Figure 3.4 can be found in the Appendix A.

Table 3.3. Benchmarking parameters for results in Table 3.2 and Figure 3.4.

Input Parameters	
Emitter Inner Radius (µm)	**3.95±0.25**
C_R (average)	3.2
C_R mode limit	3.25
ξ (Ω^{-1})	1.8e-8
p_{scale}	0.023
Droplet energy loss (V)	150
Beam divergence	30°
Tip-to-Extractor Distance (µm)	175
Output Parameters	
Fraction of emitters in PIR	0.46

ESPET predicts the curvature of the onset, a direct consequence of the variance in onset voltages introduced again by the tolerance of the emitter radius (and thus the Taylor cone base radius). The experiments by Dandavino *et al.* included several IV curves for different acceleration (boost) voltages. We plot only the curve for zero boost voltage. The other curves exhibit a variance comparable to the statistical variance of the model shown in Figure 3.4.

3.2 Actively Pressurized Capillary, Ionic Liquid Propellant

Here we only report on the QuickSolver solution. We first tested the QuickSolver on the capillary emitter reported by Gamero-Castaño and Hruby [*Gamero-Castaño and Hruby*, 2001]. We assumed a 1 cm long capillary emitter with a 22 μm inner diameter, a 1 m long capillary feed with 100 μm inner diameter, and an extractor-tip distance of 5 mm. We accounted for a 150 V droplet kinetic energy deficit and a divergence of 30°. Table 3.4 compares the ESPET outputs to experimental results obtained for two actively pressurized mass flows. The pressure is adjusted so that the mass flow results in a close match to the Busek experiment. The extraction voltage is also set to that of the experiment. The experimental data comparison to the QuickSolver outputs is very satisfactory with the largest discrepancy a 28% overestimation of q/m for the lower flow rate.

Table 3.4. Comparison between ESPET QuickSolver Outputs and data acquired by Gamero-Castaño and Hruby for an EMI-TFSI propelled single capillary thruster [*Gamero-Castaño and Hruby*, 2001].

Property	**ESPET**	**Busek**	**ESPET**	**Busek**
Pressure (Pa)	21,200		8,000	
Thrust (μN)	0.675	0.63	0.33	0.35
I_{sp} (s)	129	126	164	171
q/m (C/kg)	641	625	1050	820
Mass flow (µg/s)	0.53	0.54	0.20	0.20
I (µA)	0.34	0.31	0.21	0.22
Extraction Voltage (V)	1,828	1,828	1,828	1,828
Efficiency (%)	69	68	69	74

Figure 3.5 is a QuickSolver screen shot of a Current-Reservoir Pressure scan. The current shows a minimum at ~150 Pa. At lower pressures and flow rates, similar to the behavior in Figure 3.3., ion field evaporation becomes an important contributor to the total current. The maximum near 50 Pa is an artifact

of the model. As mentioned earlier, at these low flow-rate (~10^{-12} kg/s) conditions, cone-jets are unstable, and the assumptions of the model break down.

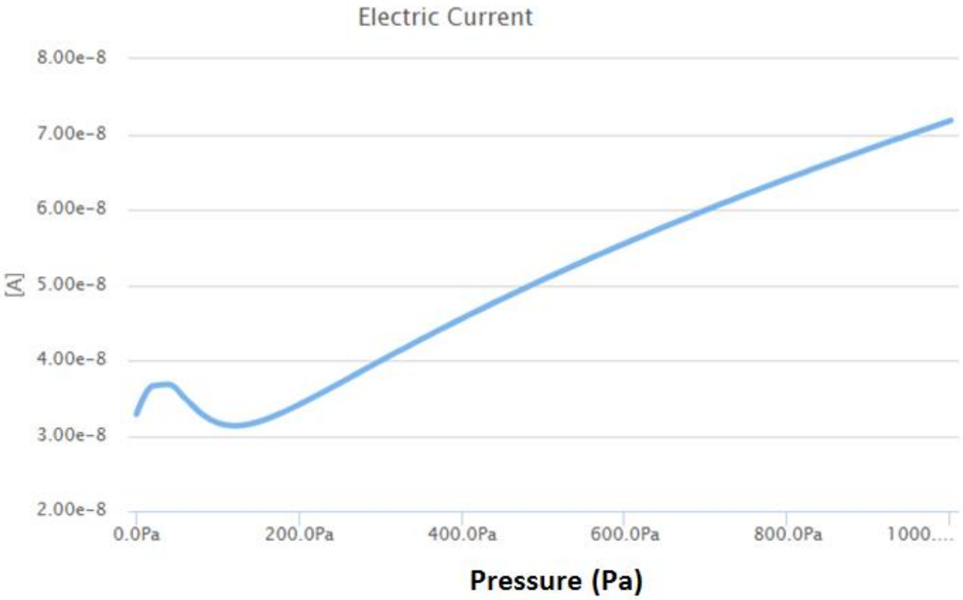

Figure **3.5.** Emitter current obtained from a pressure scan near the minimum flow limit (~10^{-12} kg/s).

3.3 Passively Fed Capillary, Liquid Metal Propellant

The LM capillary model was tested on the indium-fed capillary FEEP data reported by Tajmar [*Tajmar*, 2004]. Figure 3.6 shows voltage-current curves computed with the QuickSolver and compared to Tajmar's data for two emitters designated high and low Z, the latter referring to the combined emitter and feed hydraulic resistance (R_{hyd}). Table 3.5 lists the parameters used in the two simulations. The full QuickSolver input deck can be found in the Appendix A. Only the emitter extractor distance of 0.7 mm was not provided by Tajmar and we adjusted it to meet the onset voltage. In the high R_{hyd} experiment, a wire was run through the capillary to increase the hydraulic resistance. Tajmar provides a formula for the hydraulic resistance of this configuration along with the necessary parameters. We simulated the wire configuration using a capillary with a smaller inner diameter having the equivalent hydraulic resistance. As is seen in Figure 3.6, the predicted slope at the low R_{hyd} conditions agrees nicely with the experimental results. The slope is significantly lower for the high R_{hyd} case where the poorer agreement suggests that the formula and parameters provided by Tajmar underpredicts the hydraulic resistance of their capillary-wire configuration.

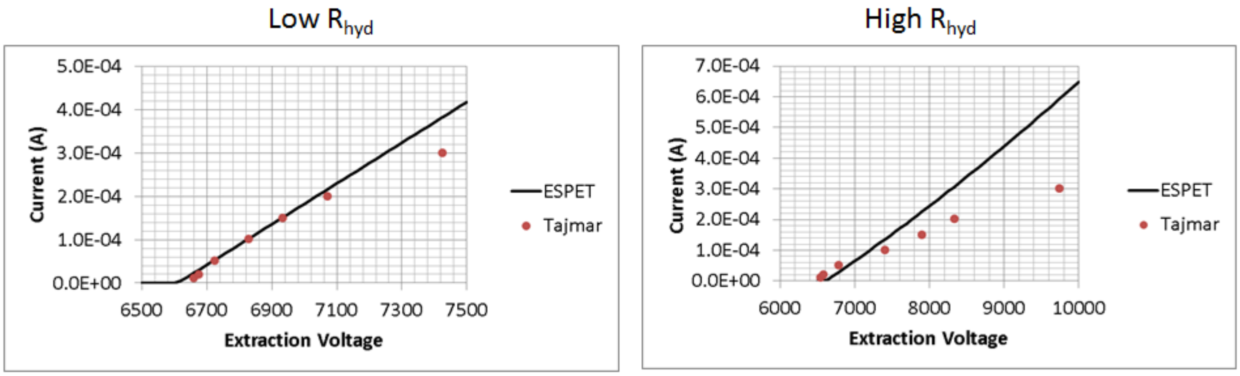

Figure 3.6. Comparison of ESPET results to data reported by Tajmar [*Tajmar*, 2004].

Table 3.5. Input parameters for FEEP testing by comparison to data reported by Tajmar [*Tajmar*, 2004].

Input Parameters	
Capillary Inner Radius (μm)	**35**
Capillary Length (mm)	3.5
Taylor Cone Base Radius (μm)	40
Beam Divergence	30°
Tip-Extractor Distance (mm)	0.7

Figure 3.7. compares the current to the computed thrust over a narrower extraction voltage range. Figure 3.8 shows voltage scan plots of the mass efficiency (see Section 2.2.2.6), I_{sp} and q/m. Here we note that the efficiency parameterization has been conducted only for low hydraulic resistance indium systems. We are not aware of any other such work although it is possible that the ESA plume database may have the necessary data to extend the model to other propellants and regimes [*Reissner, et al.*, 2013].

While the thrust shows a near linear voltage relationship, we see that the mass efficiency and I_{sp} drop rapidly with increasing voltage and current above ~6,620 V. FEEPs are known to lose mass efficiency at currents above ~10 μA [*Papadopoulos*, 1987; *Tajmar*, 2011]. As seen in Figure 3.7, the current is 10 μA at ~6,630 V. Figure 3.8 also plots the average q/m of the FEEP spray. The efficiency at a current of 100 μA (6,820 V) is only ~4%. This is slightly lower than experimental data for a similarly sized Taylor cone, where an efficiency of ~6% was reported[*Tajmar*, 2005]. Note that this is the work that was used to parameterize the ESPET efficiency formula.

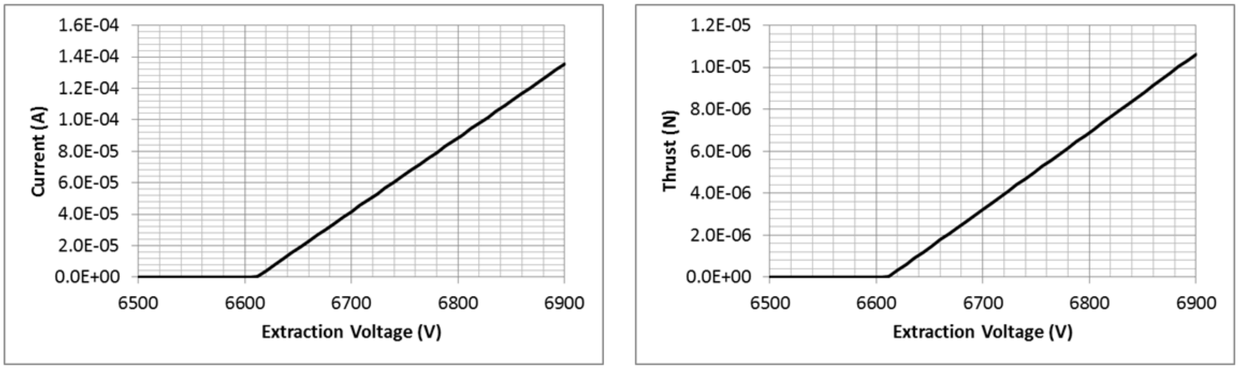

Figure 3.7. ESPET QuickSolver current and thrust estimates for low R_{hyd} emitter reported by Tajmar [*Tajmar*, 2004].

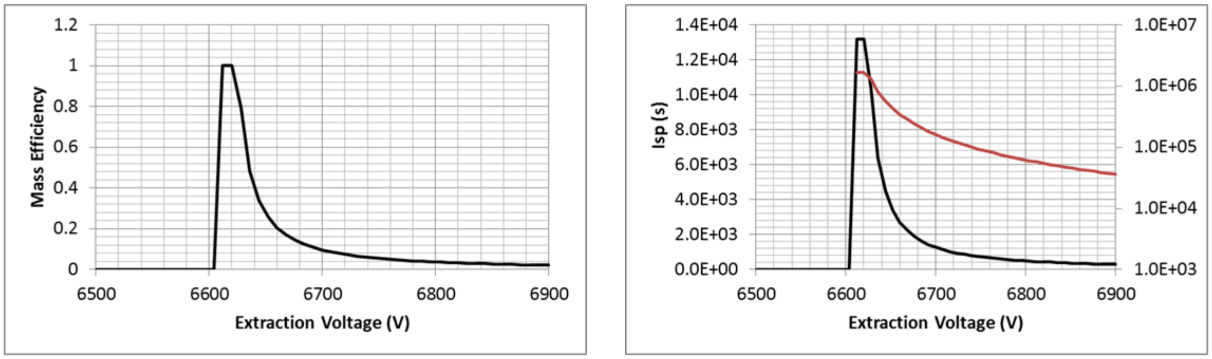

Figure 3.8. Mass efficiency, I_{sp}, and q/m versus extraction voltage computed for low R_{hyd} emitter reported by Tajmar [*Tajmar*, 2004].

3.4 Externally Wetted Emitter, Ionic Liquid Propellant

Here we use data recorded by Busek on a 6 μm radius of curvature conical tungsten tip wetted with EMI-TFSI. The tip had a narrow half angle of 15° and a roughened surface. The present externally wetted emitter model requires a definition of the surface roughness as an average arithmetic mean roughness, R_a, with a standard deviation to define the emission sites and their respective curvatures, and specification of a number of feed grooves with channel radius or width (rectangular groove). Table 3.6 lists the input parameters chosen for the experimental emitters. The roughness is chosen from a visual estimate of the tip image. Similarly, the groove diameter is chosen from a groove seen in a microscope image. The number of emission sites can be estimated from the ratio of the total tip surface area ($\sim 2\pi r_{tip}^2$) to the average cross section of an emission site protrusion (πr_{site}^2). With r_{tip} = 6 μm and r_{site} = 2.8 μm, we get slightly more than 9 emission sites, which we have rounded to 10.

Given the significant standard deviations, we have attempted to obtain average performances for computational runs on 1,000 emitters. Even for that number of emitters, the variance in the outputs was still significant. We, therefore, have to assume that a model without detailed surface property information on the experimental tip will have substantial uncertainties when comparing to a single tip. Figure 3.9 compares the positive polarity data to four ESPET runs consisting of emitter averages. The experimental and model data compare favorably at low extraction voltages until ~1,500 V, where the ESPET runs diverge from each other, and where the Busek data appears to make a jump to higher currents. The latter jump coincides with the voltage at which Busek observes pairs of beamlets from a single emission site, thus indicating that the system is in a high-field stressed mode, where efficiencies drop. Note that for the four ESPET runs, non-dimensional hydraulic resistance values, C_R, exceed 100, and the system is predicted to be in pure ionic mode. We do not have time-of-flight data to verify this. The C_R mode switching limit for EMI-TFSI was set at 20, which is significantly higher than that used for EMI-BF4 (~3).

Table 3.6. List of input parameters for externally wetted tungsten emitter test. Full input deck can be found in Appendix A.

Parameter	Value
Cone radius of curvature (μm)	6
Roughness (μm)	2.8±1.0
Number of emission sites	10
Tip height (m)	2.0×10^{-3}
Number of grooves	4
Groove radius (μm)	2.0±0.4
Feed length (m)	2.06×10^{-3}
Extractor-tip distance (μm)	200
C_R limit	20
ξ (Ω^{-1})	3.8×10^{-8}

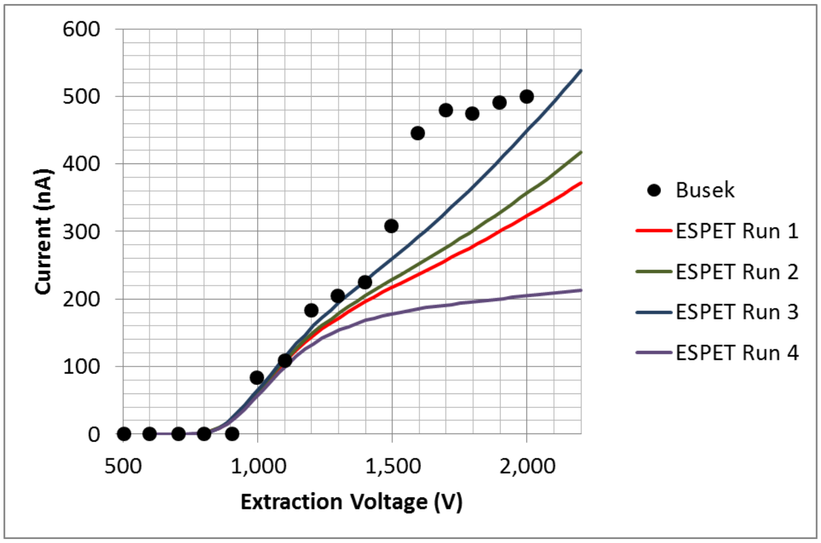

Figure 3.9. Comparison of positive polarity VI data between Busek experiment and four ESPET runs consisting of a 1,000-emitter average.

Figure 3.10 compares the observed number of emission sites for negative and positive polarity as a function of extraction voltage to the ESPET predictions. Curiously, the negative polarity exhibits almost twice as many emission sites. Since the onset voltage only depends on the surface morphology and propellant surface tension, it is not clear why the differences are so substantial, except for possible surface modification during the study of the first polarity. The VI curves are very similar for both polarities. Both the experiments and the models reach a maximum number of sites around 1,500 V. The simulation data is highly random, and we show in Figure 3.10 just one example. The present example shows that for externally wetted emitters, rough estimates of surface roughness and groove properties can lead to reasonable comparisons. However, uncertainties with respect to the precise hydraulic resistance are high.

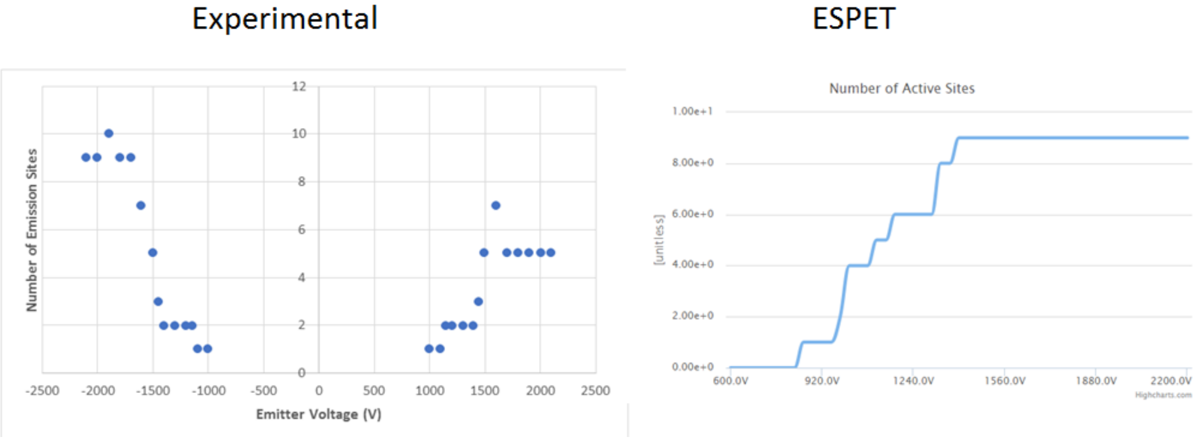

Figure 3.10. Number of emission sites observed experimentally (left) for both positive and negative polarities and predicted (right) with the ESPET QuickSolver (positive polarity only).

3.5 Externally Wetted Emitter, Liquid Metal Propellant

We tested the externally wetted liquid metal emitter model on the data reported by Tajmar [*Tajmar*, 2005] on an indium wetted tungsten needle. Figure 3.11 shows a microscopic image of the needle tip region of an emitter for which voltage-current data was reported. The latter is shown to the right of the image along with the ESPET results. Table 3.7 lists the parameters used for the simulation, several of which were obtained from the work reported by Tajmar [*Tajmar*, 2005].

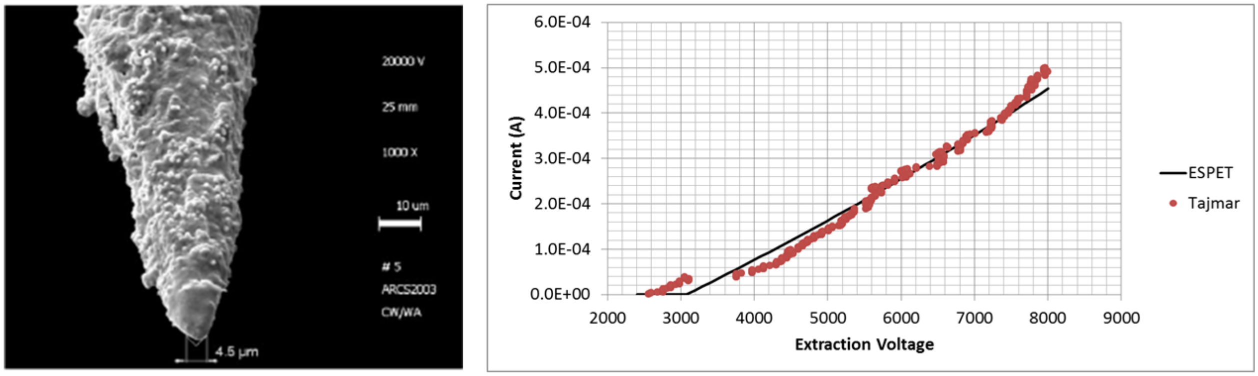

Figure 3.11. Microscopic image (left frame) of tip for which VI data in plot (right frame) was obtained for an indium wetted emitter (taken from Tajmar [*Tajmar*, 2005]). Plot shows results for parameters listed in Table 3.7.

Table 3.7. Parameters used to obtain QuickSolver results shown in Figure 3.11. Full input deck can be found in the Appendix A.

Parameter	Value
Curvature, R_c (μm)	2.25
Half Angle, ϑ (°)	15
Tip Height, L (mm)	5
Tip-Extractor Distance, D (mm)	2
Film Thickness, δ (μm)	0.5
Temperature, T (K)	453

The only parameter with high uncertainty, and for which no measurement was provided, is the film thickness, δ. We found that the VI results were insensitive to this parameter above 0.3 μm. Below this value, the VI slope drops with declining film thickness and the agreement with experiment becomes poorer. This suggests that the needle operated in a low Z regime where the feed hydraulic resistance is immaterial in the VI relationship. For this needle, Tajmar reports a mass efficiency of 52.5% at a current of 100 μA, which is in good agreement with the ESPET prediction of 50%. The ESPET mass efficiency voltage curve is shown in Figure 3.12. The good agreement is further evidence of this needle operating in a low Z regime.

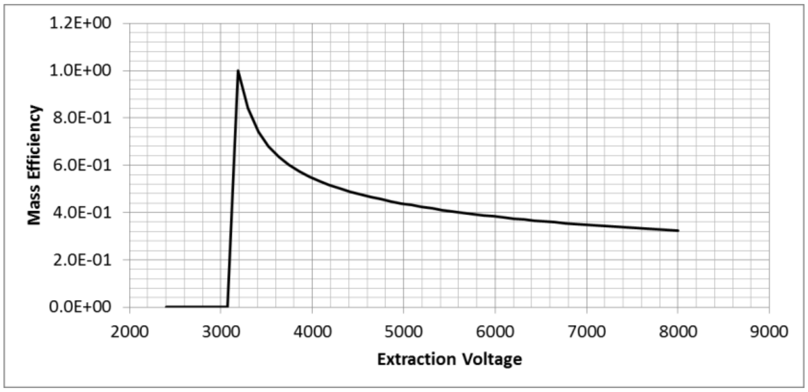

Figure 3.12. Mass efficiency versus extraction voltage computed by QuickSolver for needle shown in Figure 3.11.

3.6 Porous Cone, Ionic Liquid Propellant

Given the high activity in developing porous IL emitter systems, and the higher complexity of the emission properties of these systems, similarly to our experimental work, we have devoted significant resources to benchmarking the Porous Cone IL model. We start with the single borosilicate emitters characterized at Busek and then we apply the model to the single xerogel emitters studied by Lozano and Perez-Martinez [*Perez-Martinez and Lozano*, 2015; *Perez-Martinez*, 2016].

3.6.1 Single Porous Borosilicate Emitter

In this Section we benchmark ESPET against the experimental results acquired by Busek on single conical porous borosilicate emitters. The goal of the experimental work was to improve our understanding of the effect of extraction voltage beyond onset. Of particular interest was the onset of secondary emission sites, and the IV curves of individual sites as well as the overall charge-to-mass distributions. Furthermore, we were interested in understanding the onset of unstable behavior, such as the splitting of Taylor cones into multiple Taylor cones at one emission site, and the associated efficiency changes at this transition. Unlike the externally wetted tungsten emitters discussed above, for the porous borosilicate emitters with IL propellants we did not discover an onset into an unstable multi-jet regime within the extraction voltage range that could be safely operated. Meanwhile, TOF data was also acquired at Busek, making this system optimally characterized for benchmarking emitters with multiple emission sites.

Two tips were characterized with properties listed in Table 3.8. The main difference is the general emitter shape. Tip 1 has a wedge-type geometry between a conical and edge type emitter, where the radius of curvature is smaller in one direction, and significantly broader in the orthogonal direction. Nevertheless, we cannot identify within experimental uncertainties a difference in the onset voltage. This suggests that the narrow curvature in a wedge or edge emitter is sufficient to estimate the onset voltage. Tip 2 is closer to a conical ideal and has a curvature of 16 μm.

Table 3.8. Emitter setup for benchmarking Busek porous borosilicate emitter tips. Two properties are given when there are differences between Tip 1 and Tip 2.

Property	Value
Propellant:	EMI-TFSI
Feed:	Cylindrical porous
Material:	Borosilicate P3
Diameter (m):	4×10^{-4}
Length (m):	2.5×10^{-4}
Emitter:	
Material:	Borosilicate P5
Height (m):	3.5×10^{-4}
Cone half angle (deg):	30
Radius of curvature (m):	17×10^{-6}, 16×10^{-6}
Pore size (m):	$(0.8 \pm 0.4)\times10^{-6}$
Extractor-tip distance (D, m):	1.5×10^{-4}, 1.2×10^{-4}
Polarity	Positive

If we assume that the average pore size listed in Table 3.8 represents the base radius of the Taylor cones that lead to current emission, we estimate an onset voltage of V_0 = ~2,300 V, which is significantly higher than the observed values between 1,000 and 1,100 V. We considered three reasons for this discrepancy:

a. The liquid pools outside of the pore orifice on the emitter surface, leading to larger base radii of the Taylor cones

b. The pores flare near the surface leading to a larger effective pore radius at the surface

c. The largest pores turn on first because they have the lowest onset voltages. We find that a Taylor cone base radius of 10 µm reduces the onset voltage below 1,000 V, close to the observations.

Further clues on the mechanism can be obtained from the data recorded at Busek, which reveals nicely the voltage intervals between new emission site onsets. The ESPET porous emitter model applies tolerances to the tip dimensions and pore radii. A normal distribution random number generator selects the pore radii for each tip, and sorts them in decreasing order, the largest one being the first to turn on. Assuming a large pore radius and standard deviation of 0.8±0.4 µm, and assuming that each emission site is associated with one or more pores, we find that the variance in pore radius alone cannot explain the variance in onset voltages from emission site to emission site (mechanism *c* above). The origin of the significant variance must, therefore, be a result of changes induced by the emission onset of a new site to the remaining emission sites and their propellant pooling. Here, we postulate that the onset of a Taylor cone and the subsequent flow result in a negative pressure within the propellant which causes the propellant to be drawn into the porous medium. This would reduce the effective Taylor cone base in mechanisms *a* and *b* above. For mechanism *a*, the pooling radius is reduced and the onset voltage of the next emission site is raised. For mechanism *ii)* the propellant recedes into the porous manifold, and the effective emission radius is reduced. The combination of reduced Taylor cone base radius and some shielding due to the surrounding material leads to a higher onset voltage.

Figure 3.13 compares the number of emitting sites versus extraction voltage of the present model (ESPET, blue line) to the experimental data for Tips 1 and 2 in positive emission mode. The growth was matched using Eq. (2.53) for the evolution of the pooling or base radius. N_{max} was set to 35 and 20 for Tips 1 and 2, respectively, to get the best correspondence with the data. We note that when this work was accomplished, we had not introduced the ESPET estimate for N_{max} yet. The present work was used to benchmark the ESPET estimate. The sample QuickSolver configuration in the Appendix A, however, is set up for the latest version of the QuickSolver.

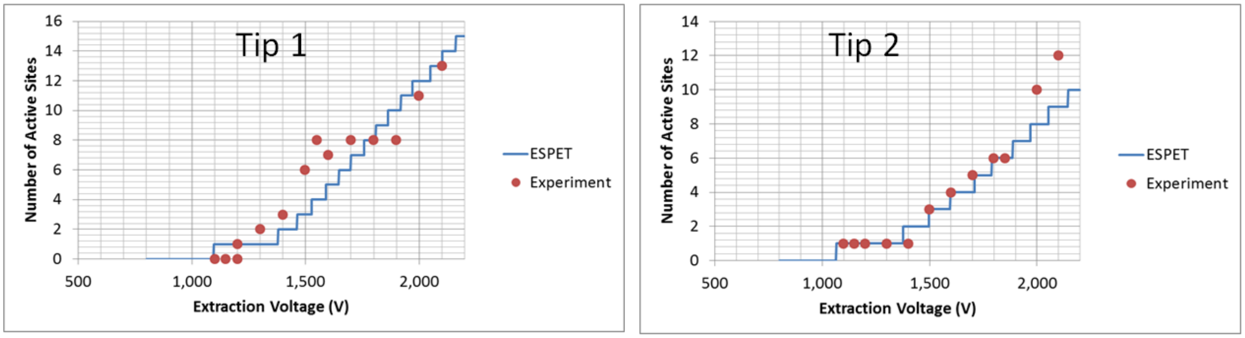

Figure 3.13. Modeled versus observed active number of emission sites versus extraction voltage for porous glass tips 1 and 2 (positive mode).

We next attempted to reproduce the VI curves using a model that accounts for multiple sites per tip. We considered two limiting cases for the hydraulic resistance of individual emission sties: in the first (Model 1) we assume that the total hydraulic resistance is given by Eq. (2.3) and consists of the sum of the resistances associated with each emission site. Thus, the hydraulic resistance of an individual site, $R_{hyd,i}$ is NR_{hyd}, where N is the number of active sites. This can be rationalized with the microfluidic path involving a smaller volume feeding the tip, and thus a higher hydraulic resistance. In the second case, we assume that the hydraulic resistance given by Eq. (2.3) applies to all emission sites (Model 2), i.e., the overall tip hydraulic resistance dictates the Taylor cone physics of each emission site.

Figure 3.14. compares the VI curves of tips 1 and 2 (positive mode) to the two model outputs just discussed. As is seen, the models both do a reasonable job in reproducing the behavior near onset. At higher voltages, Model 1 provides a significantly better agreement with experiment. The benchmarking parameters used for the models are listed in Table 3.9. The only differences, apart from the tip geometry, are in the number of sites and the initial base radius. The larger number of sites for Tip 1 is consistent with the broader emission area of the wedge emitter tip. We attempted to improve the data-model comparison with the pressure scaling parameter, p_{scale}, however, this had a minor effect as the rapid IV growth appears to indicate a strong ionic component.

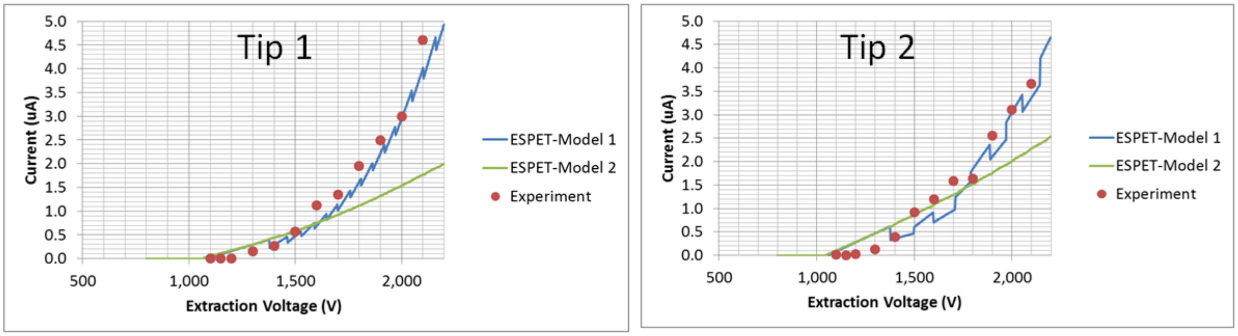

Figure 3.14. ESPET model comparison to experimental VI curves for porous glass tips 1 and 2 (positive mode).

Table 3.9. Benchmarking parameters applied in ESPET models for positive emissions

Parameter	**Tip 1**	**Tip 2**
C_R Limit	20	20
p_{scale}	0.023	0.023
b_0 (μm)	10	8
N_{max}	35	20
ξ (Ω^{-1})	5.2×10^{-8}	5.2×10^{-8}
Spray divergence (°)	30	30

Note that the pure-ionic regime (PIR) current-voltage slope, ξ, is higher than the optimal value determined for the externally wetted emitters ($3.8\times10^{-8}\ \Omega^{-1}$). As the VI slopes in Figure 3.14 suggest, the two hydraulic resistance models follow different mechanisms. The "zig-zag" behavior of Model 1 is a consequence of the increased emission site hydraulic resistance with every new onset of such a site. The decrease in current following an onset is then governed by the slope given by ξ/C_R, where C_R is given by Eq. (2.38). The system is postulated to enter the PIR above the C_R limit, which we believe to be a propellant dependent property. Eq. (2.38) shows that as $R_{hyd,i}$ grows with the number of active emission sites on an emitter, this is counteracted by a decreasing Taylor cone base radius, which has a cubic dependence. For Model 2, on the other hand, C_R steadily declines with increasing field due to the declining b. Meanwhile, the growing field steadily increases the flow rate which forces the system into the cone-jet regime.

Here we have to add that our approach to determine the PIR only by C_R is inaccurate. Coffman [*Coffman*, 2016] demonstrates complex relationships between C_R, the surface electric field, E_n^{v}, and the base radius, *b*, in order to identify regions in phase space that are stable. A more accurate model of PIR would incorporate this physics. This would be a significant upgrade of ESPET from its current state.

The emission regime can be identified by the derived I_{sp} of the emitters. Figure 3.15 compares the computed I_{sp} for the two models and tips. Model 1 indeed predicts that the system is in the PIR throughout the voltage range for Tip 1, as evidenced by the high I_{sp} throughout the extraction voltage regime. Model 2 is predicted to be in the PIR for the first few emission sites, but eventually most sites enter a cone-jet regime where the I_{sp} drops with increasing flow rate and decreasing charge-to-mass ratio of the droplets. For Tip 2, Model 1 exhibits sporadic drops in I_{sp} at higher voltages indicating that some sites are in a mixed cone-jet mode at higher voltages.

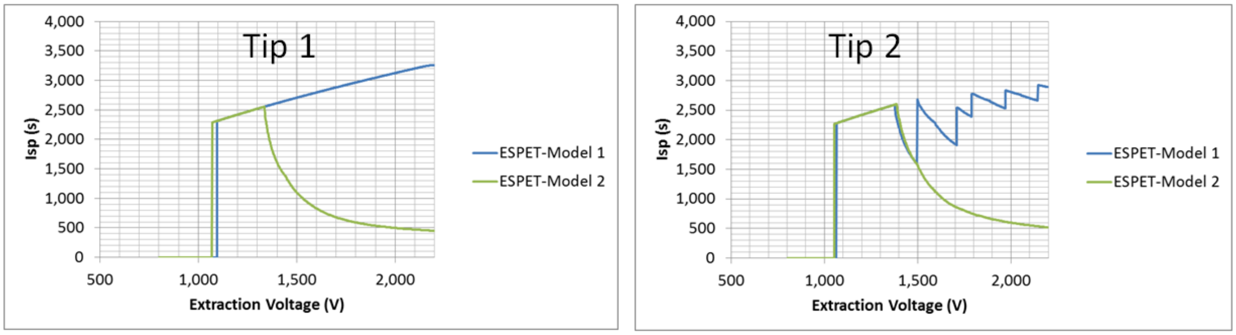

Figure 3.15. I_{sp} versus extraction voltage computed for Models 1 and 2 and the two porous glass tips.

The TOF data recorded by Busek provides further support for Model 1. When focused, the beam consisting of the combined Tip 1 and 2 currents exhibits a very low droplet percentage (~1 %) in positive mode and slightly higher in negative mode. Figure 3.16 compares the average of the Tip 1 and 2 results obtained from the present positive polarity estimates to the average *m*/*q* ($\langle m/q\rangle$) of the experiments. The modeled mass-to-charge ratio in atomic mass units (amu) is obtained from:

$$\langle m/q\rangle = \left(I_{sp} g\right)^2 / 2V \,. \tag{3.1}$$

The agreement between the Model 1 results and the experimental data is very satisfactory. ESPET assumes that half of the ion beam is composed of monomers and the other of dimers, resulting in a $\langle m/q\rangle$ value of 409 amu in PIR. The experimental data is at or above this value. Once in cone-jet mode, Model 2 predicts a steady growth of $\langle m/q\rangle$ with extraction field to values exceeding 10,000 amu. Clearly, the experimental data is in better agreement with Model 1, which correctly predicts that the tips emit nearly in PIR, and that this mode is promoted due to the increasing per-emission site hydraulic resistance, thus preventing field-induced flow to increase and promote a cone-jet mode. Interestingly, the model also predicts that the wedge-like Tip 1 is in the PIR over the entire extraction voltage range most likely due to the higher number of emission sites. This is counter-intuitive given the larger flow volume of Tip 2 in the porous medium. This is further evidence that the effective hydraulic resistance is not given by the entire volume of the porous emitter. Due to these results we have chosen Model 1 as the initial baseline model for porous borosilicate IL systems in ESPET. As shown below, this does not necessarily apply to all porous materials.

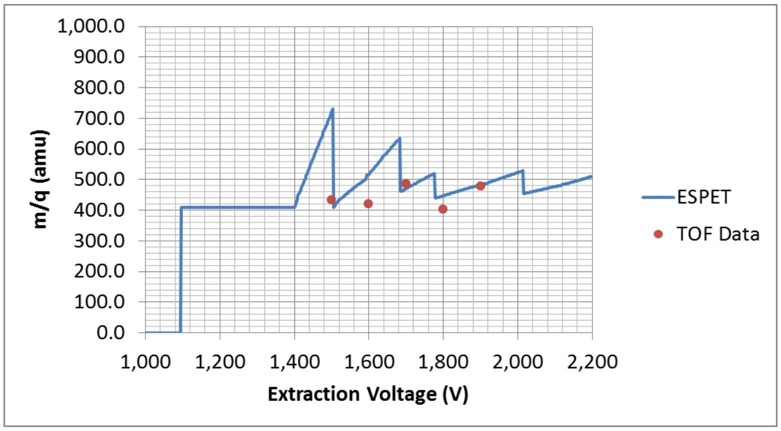

Figure 3.16. Comparison of computed (ESPET, Model 1) and measured $\langle m/q \rangle$ versus extraction voltage for positive bias. The calculations and measurements represent the average of Tips 1 and 2.

Our borosilicate benchmarking was concluded with testing against predictions for a negative bias, i.e., when the system is set up to emit negative currents. We used as a starting point the parameters obtained from benchmarking the results for a positive bias. The main difference from a modeling perspective is the significantly higher m/q values of the emitted ions in negative mode due to the substantially greater molecular mass of the TFSI anion compared to the EMI cation. Since the dimensionless hydraulic resistance is proportional to m/q, we would anticipate a higher propensity to emit in the PIR because the negative emission mode is associated with a higher C_R switching limit. The TOF data, however, show that the droplet content is greater in the negative mode. Consequently, we concluded that two parameters had to be adjusted for a good match to the VI and TOF data, the C_R switching limit, and possibly the activation energy, ΔG. We found the latter to be relatively insensitive suggesting that ion currents are predominantly from emission sites in the PIR and less from cone-jets. Interestingly, switching to the higher pure ionic m/q of the negative ions (633 versus 409 amu) lowered the output current by a fraction comparable to what was observed experimentally. However, it was necessary to raise the C_R switching limit to 30 to improve the agreement with the average m/q of the two tips. The results are shown in Figures 3.17 and 3.18 for I vs. V and $\langle m/q \rangle$ vs. V, respectively. The current magnitudes are slightly underpredicted and the $\langle m/q \rangle$ estimates fall within the experimental range. Interestingly, the hopping between essentially pure ionic and mixed cone-jet mode as predicted by ESPET is clearly also present in the data.

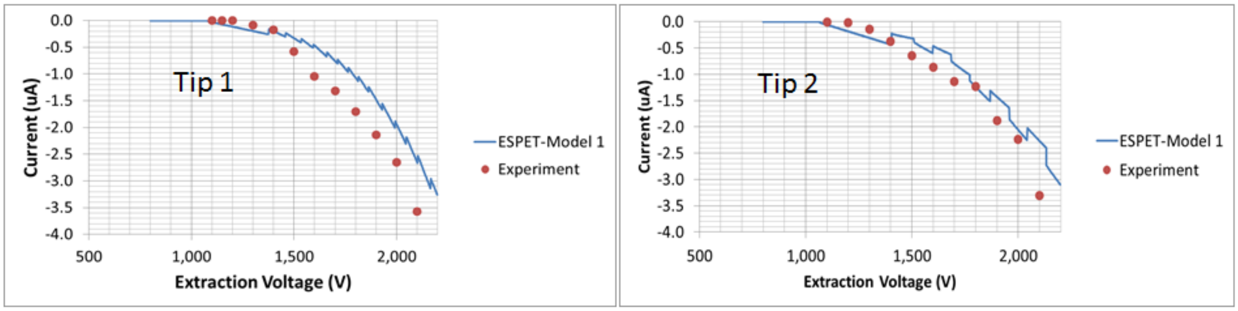

Figure 3.17. ESPET model comparison to experimental VI curves for negatively biased porous glass tips 1 (left frame) and 2 (right frame).

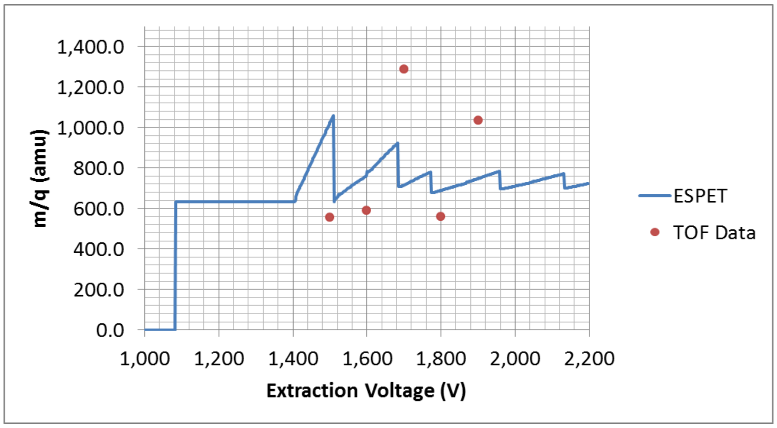

Figure 3.18. Comparison of computed (ESPET, Model 1) and measured $\langle m/q \rangle$ for negative bias. The $\langle m/q \rangle$ values represent the average of Tips 1 and 2.

3.6.2 Single Porous Xerogel Emitter

Here we benchmark ESPET against the carbon xerogel emitters developed in the group of Lozano at MIT [*Perez-Martinez and Lozano*, 2015; *Perez-Martinez*, 2016]. The group has introduced the use of resorcinol-formaldehyde xerogels, or carbon xerogels, as a new porous substrate for electrospray propulsion emitters [*Perez-Martinez and Lozano*, 2015]. The xerogels are produced from organic chemical synthesis of gels that are conventionally dried and processed to carbon structures which have lower porosities than aerogels. The synthesis of the materials can be controlled to produce nanometer size pores (meso or microporous materials). Of particular interest is the very high uniformity in pore sizes, and the ability to both mold and machine the material. The paper by Perez-Martinez *et al.* reports work on a single emitter with a pore size of only ~1.2 µm. We have entered the quoted properties into the database. We benchmarked ESPET against work detailed in the paper and in the thesis of Perez-Martinez for EMI-BF_4 and EMI-TFSI propellants [*Perez-Martinez,* 2016].

3.6.2.1 EMI-BF_4 Propellant

Figure 3.19 shows V-I curves recorded for a xerogel emitter with properties listed in Table 3.10. Time-of-flight data show that the emitter is essentially in the pure-ionic regime. The data in Figure 3.19 shows that for both polarities, the onset is near 1,600 V, and a discontinuity is observed at ~2,000 V which is attributed to the onset of a second emission site. Given the small pore size of ~1 µm an onset voltage closer to 3,000 V would be expected. The much lower onset voltage is evidence for a substantially larger Taylor cone base radius than the average pore size due to propellant pooling or larger pore sizes at the surface. A better match of the onset voltage is obtained with a pooling radius of 2.6 µm and a tip-to-extractor distance of 500 µm. Perez-Martinez made a similar conclusion [*Perez-Martinez*, 2016].

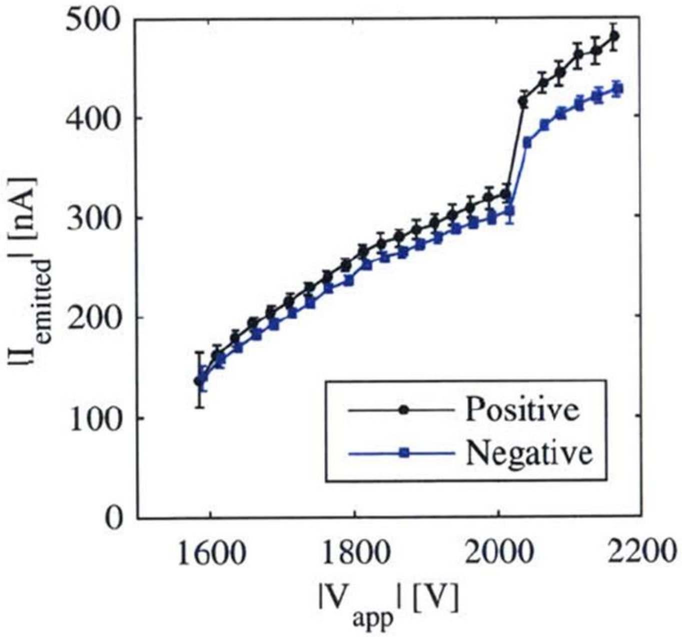

Figure 3.19. Current versus extraction voltage of a single porous xerogel emitter using EMI-BF4 in both positive and negative polarity modes.

Table 3.10. Xerogel emitter properties entered into the QuickSolver to simulate the system that produce currents shown in Figure 3.20 using an EMI-BF4 propellant.

Property	**Value**
Feed	
High Z (Pa s/m^3)	6.5×10^{17}
Emitter	
Material	Carbon Xerogel
Height (m)	1×10^{-3}
Cone half angle (deg)	25
Radius of curvature (m)	7 ×10^{-6}
Pore size (m)	(0.5 ± 0.15) ×10^{-6}
Porosity	0.6
Extractor-tip distance (D, m)	5×10^{-4}
Polarity	Positive

Figure 3.20 compares ESPET QuickSolver results for a positive polarity to the experimental data. Additional parameters set in the simulation are shown in Table 3.11. We show two output models. The model applied in the previous section for the porous borosilicate emitters is referred to as coupled (Model 1) in terms of the flow between the individual emission site channels. In the coupled limiting case, the hydraulic resistance of individual sites is proportional to the number of active sites. This worked well to reproduce the Busek borosilicate experimental results. The second model is referred to as independent, i.e., each individual emission site is associated with an independent channel with no cross flow. In this case, the hydraulic resistance associated with an emission site is independent of the number of active sites. Note that this is comparable to Model 2 tested for the borosilicate system, however, there we assumed each site was associated with the full hydraulic resistance of the porous cone. Currently, we have benchmarked the independent model with manual setting of a feed resistor.

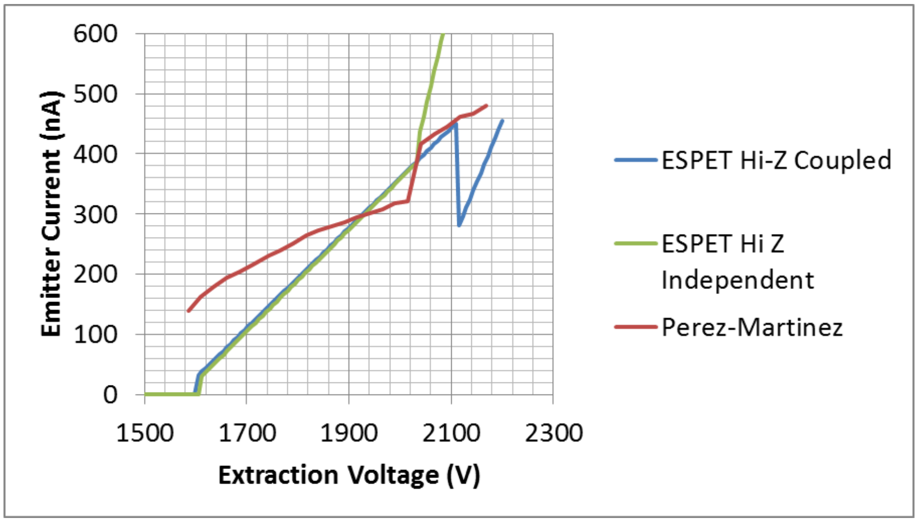

Figure 3.20. ESPET comparison to data reported by Perez-Martinez [*Perez-Martinez*, 2016].

Table 3.11 QuickSolver parameters that led to the most satisfactory comparison to the experimental data of Perez-Martinez [*Perez-Martinez*, 2016].

Property	Value
Pooling radius, b_0, (m)	2.6×10^{-6}
Number of emission sites (N_{max})	10
Divergence (°)	30
C_R Limit	3
ξ (Ω^{-1})	3.8×10^{-8}

The simulations show a step close to where the experiments exhibit a step. The fact that the two models show different step voltages can be associated with the tolerance of the pore size (see Table 3.10). The step of the coupled model, however, leads to a lower current, while for the independent model, it jumps to a higher current as seen in the experimental data. Clearly, the agreement of the first emission site is not optimal, where we observe significant discrepancy in the minimum current and the slope of the curve. Critical in getting the current in the ballpark of the observation was adding a high impedance feed. The emitter itself has a resistance of ~9×10^{16} Pas/m^3. A low-Z feed where the hydraulic resistance is given by the conical emitter resistance would result in much higher currents. The estimated hydraulic resistance using ESPET is lower than the estimate by Perez-Martinez[*Perez-Martinez*, 2016] of 5×10^{19} Pa s/m^3.

Due to this benchmarking, we introduced the option between choosing a coupled (consider active sites per emitter = T) and independent (consider active sites per emitter = F) hydraulic resistance model.

The significantly higher minimum current in the experimental data suggests a model revision is necessary. Currently, ESPET computes the minimum current from the minimum field evaporation current at the minimum cone-jet flow rate.

3.6.2.2 EMI-TFSI Propellant

Figure 3.21 shows V-I curves obtained with the same emitter impregnated with EMI-TFSI. The current shown is both for up and down ramping of an extraction voltage and both positive and negative polarities (see top chart for time evolution of the experiment).

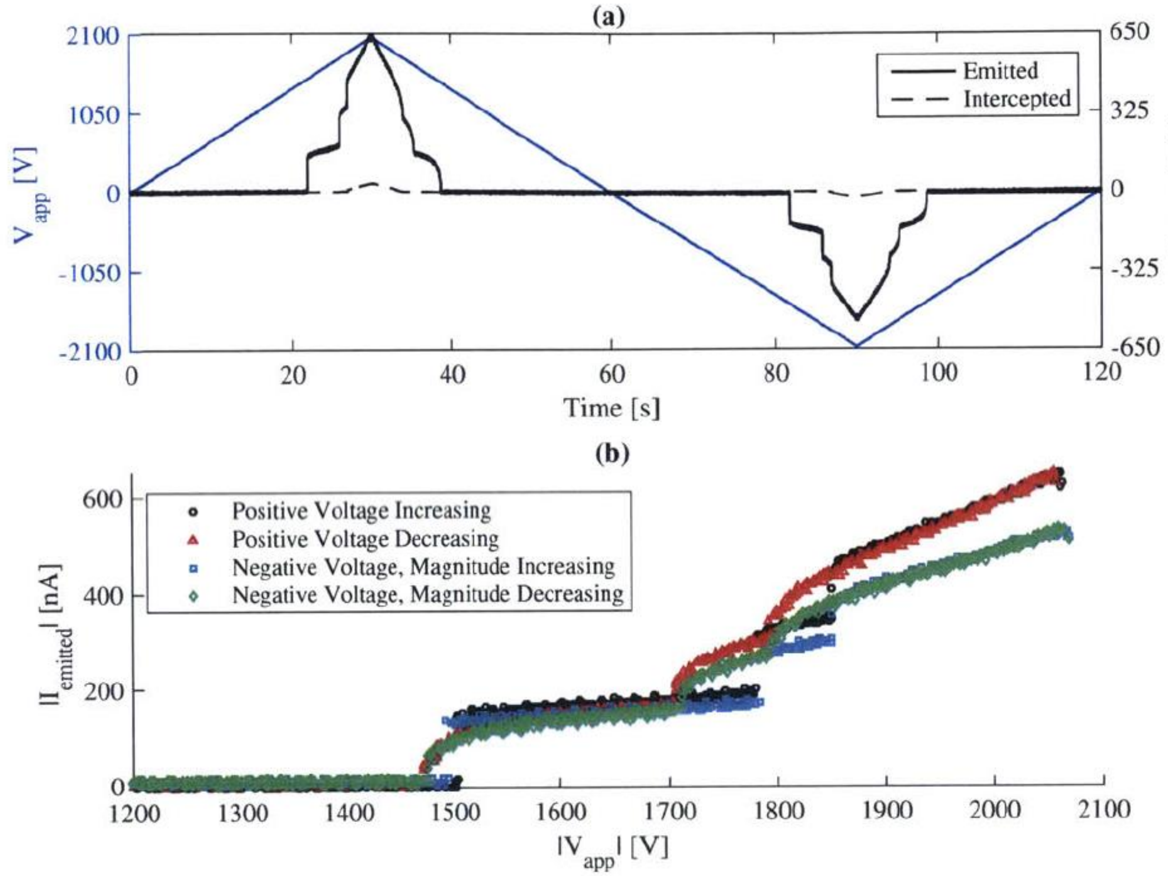

Figure 3.21. Current versus extraction voltage (bottom chart) of a single porous xerogel emitter using EMI-TFSI in both positive and negative polarity modes. Top chart shows the time evolution of the extraction voltage and observed currents (both emitted and intercepted on the extractor electrode). Taken from Martinez-Perez [*Perez-Martinez*, 2016].

Figure 3.22 compares the experimental data for a positive polarity to the QuickSolver results. The emitter properties are the same as listed in Table 3.10 except that the feed resistance was set to zero (low Z) in a first case and to 3.8×10^{17} Pa s/m^3 for a hi Z case. In comparison, the emitter hydraulic resistances computed with Eq. 2.3 are 1.4×10^{17} and 1.7×10^{17} for EMI-BF$_4$ and EMI-TFSI, respectively. Thus, the full cone, total hydraulic resistance is by a factor of 5 to 2 smaller than that associated with the individual emission sites in the Hi Z case. Both results are compared to the experimental data in Figure 3.22 and are seen to underpredict the observation. All of the emission sites are in cone-jet mode. The QuickSolver properties are listed in Table 3.12, where most notable is the pressure scaling parameter, p_{scale}, being equal to 1, significantly greater than the value of 0.023 applied to all other benchmarking efforts. Without this correction, the simulations would have greatly underpredicted the current. The hi Z case hydraulic resistance is comparable to the value applied in the EMI-BF4 simulations (see Table 3.10). The growth of the current takes on the same form as the data, but is about half that of the experiment. The low Z case provides an improved comparison with the absolute currents of the experiment, but the growth rate is higher. Note, that the onset agrees better with the VI curves measured for a descending voltage (see Figure 3.21).

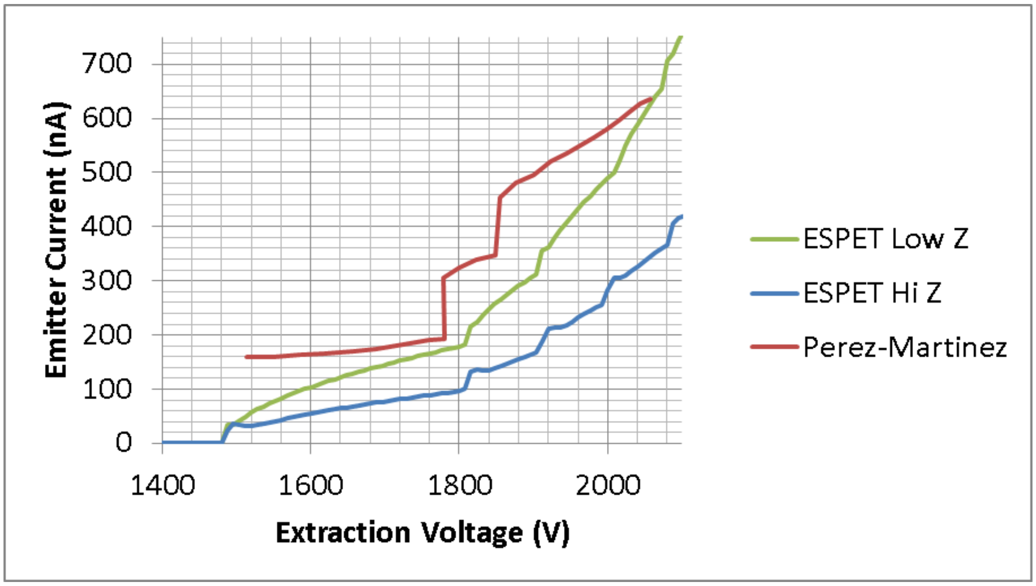

Figure 3.22. ESPET comparison to laboratory data of Perez-Martinez [Perez-Martinez, 2016] for Hi and Low Z QuickSolver models.

Table 3.12 QuickSolver parameters that led to the most satisfactory comparison to the experimental data of Perez-Martinez [*Perez-Martinez*, 2016].

Property	Value
Pooling radius, b_0 (m)	2.0×10^{-6}
Number of emission sites (N_{max})	14
Divergence (°)	30
p_{scale}	1
C_R Limit	20
ξ (Ω^{-1})	3.8×10^{-8}

The TOF data by Perez-Martinez confirm the mixed ion-droplet cone-jet mode and the much higher-pressure scaling parameter. Figure 3.23 shows the TOF spectra for the EMI-TFSI propellant in a positive polarity. The data consists of a time-integrated current received at the detector after opening the beam gate. The data shows a growing droplet fraction as evidenced by the broad growth region centered between 100 and 250 µs. The sharp inclines at ~15 and 30 µs are due to monomer (EMI^+) and dimer (EMI^+[EMI-TFSI]) ions, respectively. This is fully consistent with an increasing droplet volume flow rate with electric field, leading to lower cone-jet surface electric fields and thus lower ion evaporation fractions.

Table 3.13 lists the extracted data from the measurements in Figure 3.23. We list current fractions for monomer (f_0), dimer (f_1), trimer (f_2) and droplets (f_d), the current retrieved from the I-V curve, the volume flow rate derived from the current and m/q fractions, the pressure drop (ΔP) assuming a quoted hydraulic resistance of 3×10^{17} Pas/m^3, and a computed value assuming p_{scale} = 1. The comparison seen in the rightmost columns is very favorable in the first ~150 V above onset. The curves nicely demonstrate the growth in droplet fraction with voltage, which is consistent with our passive field-induced flow mode, where the flow rate increases with increasing field strength. At this point, we do not have an explanation for the substantially higher p_{scale} parameter, which may be yet another xerogel anomaly.

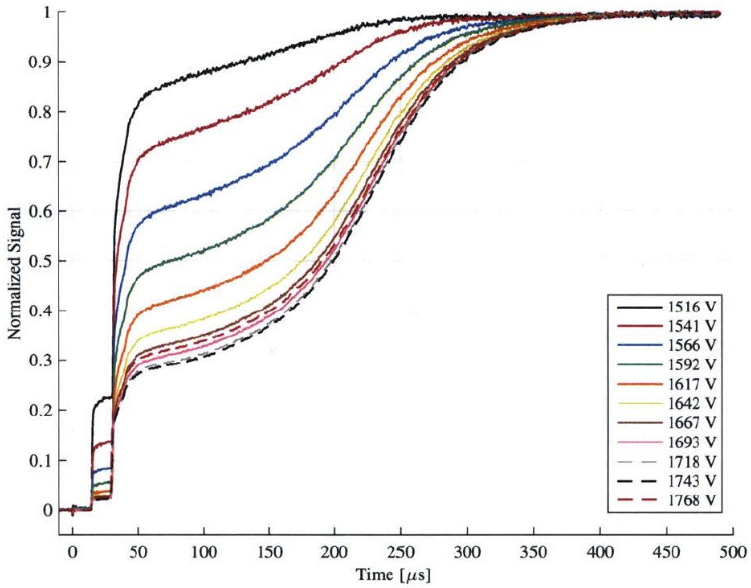

Figure 3.23. Time-of-flight spectra recorded by Perez-Martinez [*Perez-Martinez*, 2016] as a function of extraction voltage for a single carbon xerogel emitter infused with EMI-TFSI propellant (Positive polarity).

Table 3.13. Time-of-flight data extracted from [*Perez-Martinez*, 2016] for a xerogel emitter in positive mode infused with an EMI-TFSI propellant.

V_{ex}(V)	f_0	f_1	f_2	f_d	I(A)	Q(m^{-3})	ΔP	ΔP(model)
1516	0.227	0.589	0.000	0.184	1.56E-07	2.98E-15	894	267
1541	0.138	0.475	0.127	0.260	1.59E-07	4.56E-15	1369	1392
1566	0.085	0.364	0.153	0.398	1.62E-07	8.65E-15	2596	2544
1591	0.053	0.314	0.111	0.522	1.65E-07	1.26E-14	3765	3715
1617	0.037	0.230	0.140	0.593	1.69E-07	1.59E-14	4773	4904
1642	0.029	0.214	0.101	0.656	1.72E-07	1.87E-14	5600	6112
1667	0.022	0.193	0.103	0.683	1.75E-07	2.05E-14	6141	7339
1692	0.022	0.180	0.087	0.712	1.78E-07	2.27E-14	6799	8585
1717	0.022	0.180	0.077	0.722	1.82E-07	2.4E-14	7187	9849
1743	0.022	0.180	0.077	0.722	1.85E-07	2.47E-14	7423	11132
1768	0.022	0.180	0.095	0.704	1.88E-07	2.52E-14	7549	12434

3.7 Porous Cone, Liquid Metal Propellant

In this section we benchmark the LM porous cone model in the QuickSolver against the 28 emitter porous Tungsten crown emitter operating on liquid indium reported by Reissner *et al.* [*Reissner, et al.*, 2015] and shown in Figure 3.24. Table 3.14 shows the parameters used to compute the emission characteristics of the array partially based on information obtained from the paper by Reissner and coworkers. We compare the experimental and ESPET QuickSolver VI curves in Figure 3.25. The primary adjustable parameter that affected the VI curve was the pooling radius and the cone radius of curvature. The best agreement was obtained when setting the pooling radius equal to the pore radius. The primary source of statistics was the standard deviation of the tip radius of curvature and the pore radius. Since we assume a single site per emitter, the onset voltage will be comparable for all emitters.

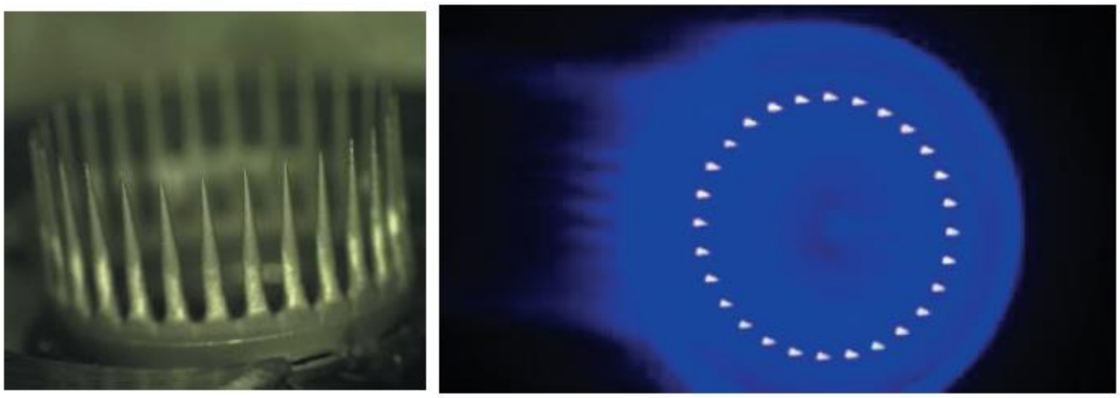

Figure 3.24. 28 crown emitter manufactured from sintered porous tungsten [*Reissner, et al.*, 2015]. Right image shows the array in operation, producing a blue micro-crown discharge at every emitting tip.

Table 3.14. Parameters used to obtain QuickSolver results in Figure 3.25. See Appendix A for full inputs.

Parameter	Value
Curvature, R_c (μm)	2.0±0.3
Half Angle, ϑ (°)	6±1
Tip Height, L (mm)	2
Tip-Extractor Distance, D (mm)	3
Number of Sites per emitter	1
Pore Radius (μm)	0.4±0.1
Pooling Radius (μm)	0.4
Porosity	0.3
Temperature, T (K)	453

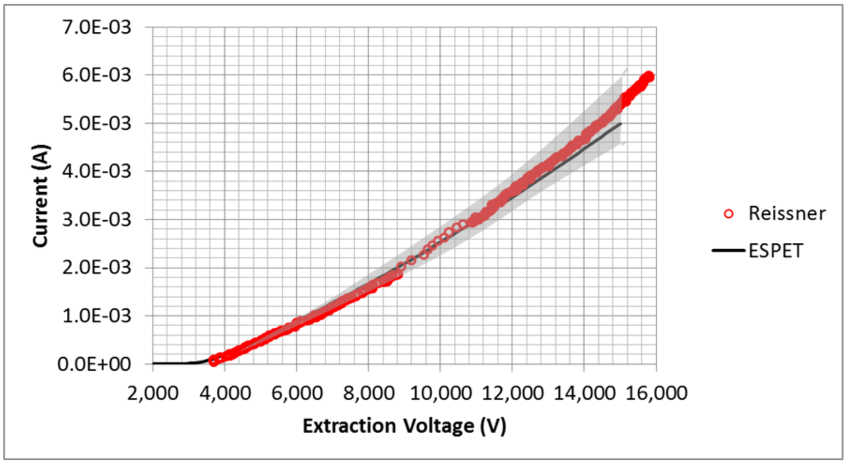

Figure 3.25. Comparison between ESPET QuickSolver outputs and data from 28 porous tungsten crown emitters reported by Reissner *et al.* [*Reissner, et al.*, 2015]. Grey-shaded area reflects approximate statistical distribution of outputs given by the standard deviations of parameters listed in Table 3.14.

As is seen in Figure 3.25, the agreement between the ESPET QuickSolver model and the experimental VI current data is excellent. Figure 3.26 shows the number of active sites versus extraction voltage and the corresponding thruster efficiency. In case of the former we see a discrepancy with the experimental data as Reissner *et al.* report that even at 20 kV, not all emitters are firing. Vasiljevich *et al.* [*Vasiljevich, et al.*, 2011] interpret non-uniformity of emission with retracted liquid metal propellant in pores, i.e., a condition that exists prior to start-up. Thus, the ESPET per emitter intensity may be underestimated. This discrepancy could potentially be reconciled with the notion that for those emitters, where the wetting of the propellant is optimal, multiple emission sites exist. As mentioned earlier, for LM porous systems, ESPET currently assumes a single emission site. Another explanation for underestimation may be the neglect of the effect of the crown discharge, seen in Figure 3.24.

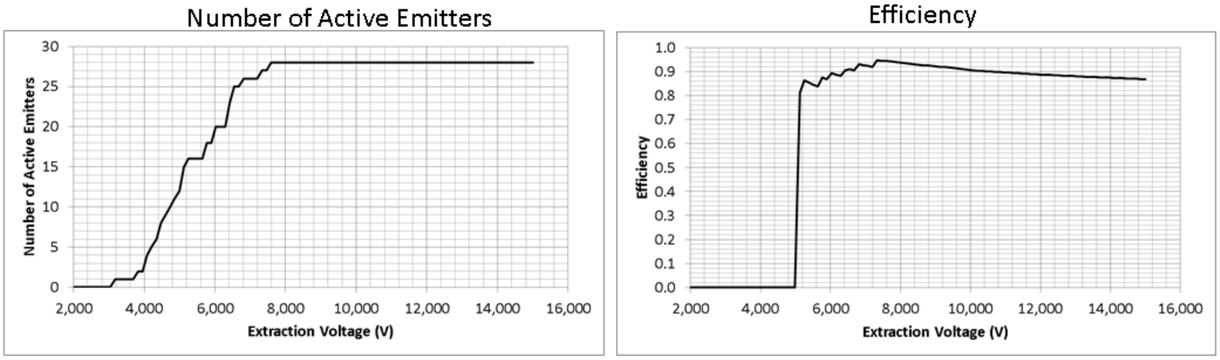

Figure 3.26. Extraction voltage dependence of number of active emitters and efficiency.

The efficiency is close to 90% and declines with voltage due to the increase in droplet formation. The efficiency remains very high for this system due to the small Taylor cone base radius of only ~0.8μm (pooling radius plus pore radius).

3.8 Porous Edge Emitter, Ionic Liquid Propellant

In this section we benchmark the edge emitter model against Busek measurements of porous borosilicate edge emitters. We compare the performance to the EMI-TFSI impregnated thruster consisting of 9 7 mm long porous edges made of P5 porous borosilicate coupled with a P2 borosilicate reservoir. The latter was treated as a low-Z feed system given its low hydraulic resistance. Table 3.15 lists the parameters used for the simulation and Figure 3.27 shows the computed VI curve for both positive and negative emission and curves for the number of active and pure ion sites versus voltage. The parameters are consistent with the parameters used for the single P5 borosilicate porous cone emitters (see Section 3.6.1).

Table 3.15. Parameters used to obtain QuickSolver results in Figure 3.25 (Appendix A for full inputs).

Parameter	Value
Edge Curvature, R_c (μm)	15.0±1.5
Edge Length (mm)	7
Half Angle (°)	30±2
Divergence (°)	30
Edge Height (μm)	350
Edge-Extractor Distance	0.5
Number of Sites per emitter (ESPET estimate)	1097
Number of emitters	9
Pore Radius (μm)	0.8±0.2
Pooling Radius (μm)	8
Porosity	0.5
Temperature, T (K)	300
p_{scale}	0.023
C_R Limit	20
ξ (Ω^{-1})	5.2×10^{-8}
Droplet energy loss (V)	150

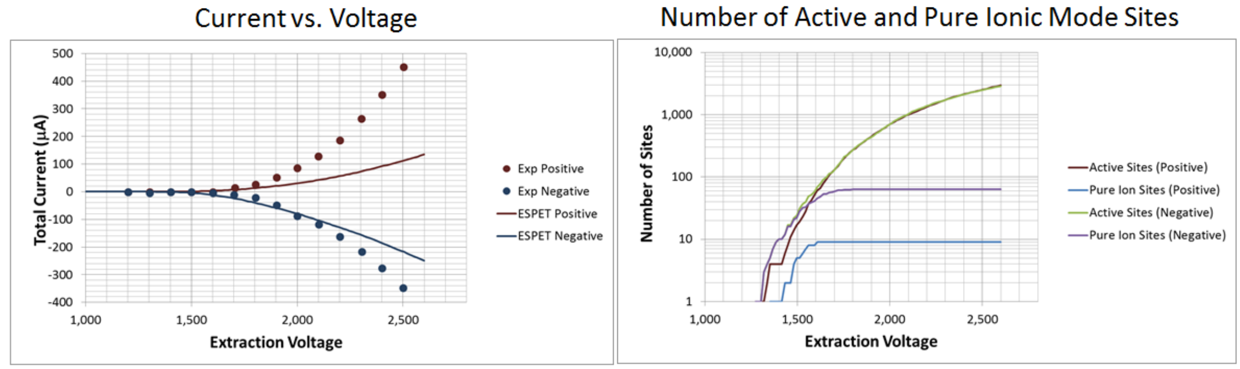

Figure 3.27. ESPET comparison to experimental data for P5 borosilicate porous edge emitters. Left: Voltage-current curves. Right: Active sites and pure ionic sites versus extraction voltage.

ESPET underpredicts the current for both polarities. Interestingly, unlike the single cone emitters, here ESPET predicts a higher current in the negative polarity. This, however, is also in contrast with the experimental measurements. Nevertheless, the general shape of the VI curve agrees well with the experimental observation. The shape can be mainly attributed to the growth in emission sites along the emitter edge. The right-hand side of Figure 3.27 shows the growth in active emission sites, as well as the growth in sites in pure ionic mode. Note that only a small fraction of the emitting sites are in pure ionic mode, and that the negative polarity has a significantly higher propensity to operate in the pure-ionic regime (PIR). Also note that even at 2,600 V, only ~30% of the ~9,000 total emission sites included in the calculation are active.

Figure 3.28 compares ESPET estimates for thrust and I_{sp} to an experimental derivation by Busek. Here, the agreement has significantly improved in comparison to the VI curves in Figure 3.27. Given this satisfactory agreement, this calls for an explanation why the VI curves so poorly reproduce the experimental data. The substantially higher current in the negative polarity, and the marked difference in the number of sites in PIR, suggest that inaccuracies in the ESPET PIR model may be the source of the discrepancy. From the expression for the dimensionless hydraulic resistance, C_R, we see that this parameter is proportional to m/q. Thus, the average C_R will be higher in negative mode due to the significantly higher negative ion mass of EMI-TFSI. Consequently, given our model for a C_R switching limit, more sites are predicted to be in PIR. The fact that the experiments do not predict a higher current in negative polarity, in fact, the opposite, suggests that the present PIR switching model is inaccurate. We knew from its inception, however, that this was just a stand-in model until a more comprehensive area of the complicated field, C_R, p_{int}, and b phase space has been computed in search of stable PIR regimes.

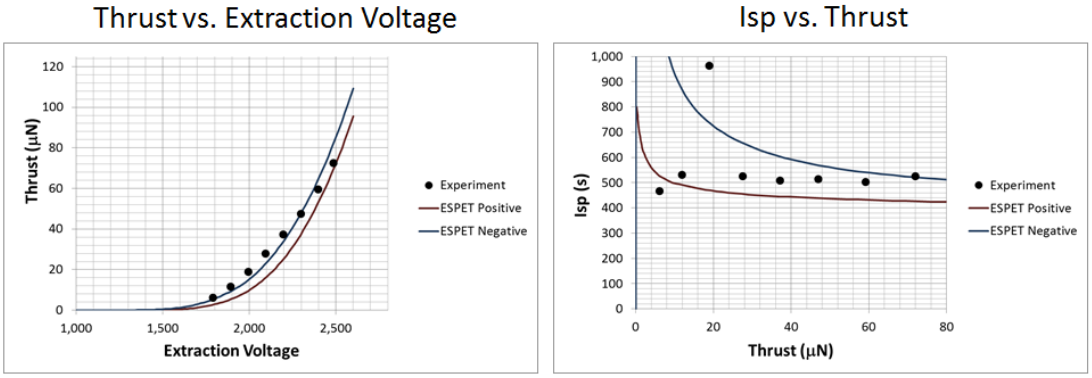

Figure 3.28. Experimental and ESPET estimates of thrust versus extraction voltage (left) and I_{sp} versus thrust for a porous borosilicate edge emitter (see Table 3.15).

The combination of a small percentage of PIR sites, and the very broad extraction voltage regime, which leads to substantial current scaling in the PIR, results in a significant current percentage contributed by the PIR sites. For a C_R value of 20 (switching limit), the current-voltage slope is 2.6 nA/V (see slope parameter in Tab. 3.15). Thus, from the onset at ~1600 V to an extraction voltage of 2600 V, the current grows to ~2.6 μA for a PIR site. Since we have approximately 50 more PIR sites in negative mode, this corresponds to about a 130 μA difference in PIR current, which is very consistent with the polarity current difference seen in Figure 3.27.

REFERENCES

Bruus, H. (2007), "Theoretical Microfluidics", Oxford University Press.

Chiu, Y., B. L. Austin, R. A. Dressler, D. Levandier, P. T. Murray, P. Lozano, and M. Martinez-Sanchez (2005), "Mass spectrometric analysis of colloid thruster ion emission from selected propellants", *J. Prop. Power*, *21*, 3, 416-423.

Coffman, C. (2016), "Charge emission from electrified ionic liquid menisci: fundamental phenomena and applications to micropropulsion", Ph.D. Dissertation thesis, Massachusetts Institute of Technology, Cambridge, MA.

Coffman, C., M. Martínez-Sánchez, F. Higuera, and P. C. Lozano (2016), "Structure of the menisci of leaky dielectric liquids during electrically-assisted evaporation of ions", *Appl. Phys. Lett.*, *109*, 23, 231602.

Courtney, D. G. (2006), "On the identification and mitigation of life-limiting mechanisms of ionic liquid ion sources envisaged for propulsion of microspacecraft", Ph.D. Dissertation thesis, Massachusetts Institute of Technology, Cambridge, MA.

Cusack, N. E. (1963), "The electronic properties of liquid metals", *Reports on Progress in Physics*, *26*, 1, 361.

Dandavino, S., C. Ataman, C. N. Ryan, S. Chakraborty, D. Courtney, J. P. W. Stark, and H. Shea (2014), "Microfabricated electrospray emitter arrays with integrated extractor and accelerator electrodes for the propulsion of small spacecraft", *J. of Micromechanics and Microengineering*, *24*, 7, 075011.

Dandavino, S., C. Ataman, H. Shea, C. Ryan, and J. Stark (2011), Microfabrication of Capillary Electrospray Emitters and ToF Characterization of the Emitted Beam, IEPC-2011-131, in *32nd International Electric Propulsion Conference,* edited, Wiesbaden, Germany.

Fernández de la Mora, J., and I. G. Loscertales (1994), "The current emitted by highly conducting Taylor cones", *J. Fluid Mech.*, *260*, 155-184.

Fröba, A. P., H. Kremer, and A. Leipertz (2008), "Density, Refractive Index, Interfacial Tension, and Viscosity of Ionic Liquids [EMIM][EtSO4], [EMIM][NTf2], [EMIM][N(CN)2], and [OMA][NTf2] in Dependence on Temperature at Atmospheric Pressure", *J. Phys. Chem. B*, *112*, 39, 12420-12430.

Gamero-Castano, M. (2010), "Energy dissipation in electrosprays and the geometric scaling of the transition region of cone-jets", *J. Fluid Mech.*, *662*, 493-513.

Gamero-Castaño, M. (2004), "Characterization of a Six-Emitter Colloid Thruster Using a Torsional Balance", *J. of Propulsion and Power*, *20*, 4, 736-741.

Gamero-Castaño, M., and V. Hruby (2001), "Electrospray as a Source of Nanoparticles for Efficient Colloid Thrusters", *J. of Propulsion and Power*, *17*, 5, 977-987.

Ganan-Calvo, A., J. Davila, and A. Barrero (1997), "Current and droplet size in the electrospraying of liquids. Scaling laws", *J. of Aerosol Science*, *28*, 2, 249-275.

Guerra-Garcia, C., D. Krejci, and P. Lozano (2016), "Spatial uniformity of the current emitted by an array of passively fed electrospray porous emitters", *J. of Phys. D: Applied Physics*, *49*, 11, 115503.

Hardy, S. C. (1985), "The surface tension of liquid gallium", *J. Crystal Growth*, *71*, 3, 602-606.

Higuera, F. J. (2008), "Model of the meniscus of an ionic-liquid ion source", *Phys. Rev. E*, *77*, 2, 026308.

Keene, B. (1993), "Review of data for the surface tension of pure metals", *International Materials Reviews*, *38*, 4, 157-192.

Kolbeck, C., J. Lehmann, K. Lovelock, T. Cremer, N. Paape, P. Wasserscheid, A. Froba, F. Maier, and H.-P. Steinruck (2010), "Density and surface tension of ionic liquids", *J. Phys. Chem. B*, *114*, 51, 17025-17036.

LTspice(2017),http://www.linear.com/solutions/ltspice",http://www.linear.com/solutions/ltspice.

Lu, H., and Q. Jiang (2005), "Surface tension and its temperature coefficient for liquid metals", *J. Phys. Chem. B*, *109*, 32, 15463-15468.

Luedtke, W. D., U. Landman, Y. H. Chiu, D. J. Levandier, R. A. Dressler, S. Sok, and M. S. Gordon (2008), "Nanojets, Electrospray, and Ion Field Evaporation: Molecular Dynamics Simulations and Laboratory Experiments", *J. Phys. Chem. A*, *112*, 40, 9628-9649.

Mair, G. (1997), "The effects of flow impedance on the current-voltage characteristics of liquid-metal ion sources", *J. of Phys. D: Appl. Phys.*, *30*, 13, 1945.

Martinez-Sanchez, M. (2007), 16.522 lecture notes, MIT Spring 2007., edited.

McEwen, A. B., H. L. Ngo, K. LeCompte, and J. L. Goldman (1999), "Electrochemical properties of imidazolium salt electrolytes for electrochemical capacitor applications", *Journal of the Electrochemical Society*, *146*, 5, 1687-1695.

Papadopoulos, S. (1987), "The average mass-to-charge ratio of species emitted from liquid In ion sources", *J. of Phys. D: Appl. Phys.*, *20*, 4, 530.

Perez-Martinez, C., and P. Lozano (2015), "Ion field-evaporation from ionic liquids infusing carbon xerogel microtips", *Appl. Phys. Lett.*, *107*, 4, 043501.

Perez-Martinez, C. S. (2016), "Engineering ionic liquid ion sources for ion beam applications", Ph. D. Dissertation thesis, Massachusetts Institute of Technology, Cambridge, MA.

Reissner, A., N. Buldrini, B. Seifert, T. Hörbe, F. Plesescu, J. G. del Amo, and L. Massotti (2015), Testing and Modelling of the mN-FEEP Start-Up Performance, IEPC-2015-123, in *34th International Electric Propulsion Conference and 6th Nano-satellite Symposium*, edited, Hyogo-Kobe, Japan.

Reissner, A., S. Hummel, and E. Gengembre (2013), Development Status and Future of the European Electric Propulsion Plume Database, IEPC-2013-206, in *The 33st International Electric Propulsion Conference*, edited, The George Washington University, USA.

Strauss, S. (1962), "The Temperature Dependence of the Viscosity of Liquid Metals", *Nuclear Sci. and Eng.*, *12*.

Tajmar, M. (2004), "Indium capillary liquid-metal-ion-source operation in the flow resistance regime", *J. of Phys. D: Appl.Phys.*, *37*, 21, 3056.

Tajmar, M. (2005), "Influence of Taylor cone size on droplet generation in an indium liquid metal ion source", *Appl. Phys. A*, *81*, 7, 1447-1450.

Tajmar, M. (2011), "Overview of indium LMIS for the NASA-MMS mission and its suitability for an In-FEEP thruster on LISA", paper presented at Proceedings of the International Electric Propulsion Conference, IEPC-2011-009.

Tajmar, M., and A. Genovese (2003), "Experimental validation of a mass-efficiency model for an indium liquid-metal ion source", *Appl. Phys. A*, *76*, 6, 1003-1006.

Taylor, G. I. (1964), "Disintegration of water drops in an electric field", *Proc. Royal Soc. A*, *280*, 383-397.

Umecky, T., Y. Saito, and H. Matsumoto (2009), "Direct Measurements of Ionic Mobility of Ionic Liquids Using the Electric Field Applying Pulsed Gradient Spinâˆ' Echo NMR", *J. Phys. Chem. B*, *113*, 25, 8466-8468.

Vasiljevich, I., N. Buldrini, F. Plesescu, M. Tajmar, M. Betto, and J. del Amo (2011), "Consolidation of milli-Newton FEEP thruster technology based on porous tungsten multiemitters", paper presented at 47th AIAA/ASME/SAE/ASEE Joint Propulsion Conference & Exhibit.

Wakai, C., A. Oleinikova, M. Ott, and H. Weingärtner (2005), "How Polar Are Ionic Liquids? Determination of the Static Dielectric Constant of an Imidazolium-based Ionic Liquid by Microwave Dielectric Spectroscopy", *J. Phys. Chem. B*, *109*, 36, 17028-17030.

Williams, D. D., and R. R. Miller (1950), "Densities of Liquid and Solid Indium", *Journal of the American Chemical Society*, *72*, 8, 3821-3821.

Xu, W.-G., L. Li, X.-X. Ma, J. Wei, W.-B. Duan, W. Guan, and J.-Z. Yang (2012), "Density, surface tension, and refractive index of ionic liquids homologue of 1-alkyl-3-methylimidazolium tetrafluoroborate [C n mim][BF4](n= 2, 3, 4, 5, 6)", *Journal of Chemical & Engineering Data*, *57*, 8, 2177-2184.

Yang, J.-Z., Q.-G. Zhang, and F. Xue (2006), "Studies on the properties of EMIGaCl4", *Journal of Molecular Liquids*, *128*, 1–3, 81-84.

Zaitsau, D. H., G. J. Kabo, A. A. Strechan, Y. U. Paulechka, A. Tschersich, S. P. Verevkin, and A. Heintz (2006), "Experimental Vapor Pressures of 1-Alkyl-3-methylimidazolium Bis(trifluoromethylsulfonyl)imides and a Correlation Scheme for Estimation of Vaporization Enthalpies of Ionic Liquids", *J. Phys. Chem. A*, *110*, 22, 7303-7306.

Zhang, S., N. Sun, X. He, X. Lu, and X. Zhang (2006), "Physical properties of ionic liquids: database and evaluation", *J. of Phys. and Chem. Ref. Data*, *35*, 4, 1475-1517.

APPENDIX A

A. QuickSolver Configurations

The configurations below represent the benchmarking inputs used in the present report and can be copied and pasted into the QuickSolver.

a. Actively Pressurized Capillary, Ionic Liquid Propellant

```
{
    “Feed: Cylindrical Radius_std”: “0,”
    “CR_m”: “3.806e-08,”
    “Vmin”: “1828,”
    “Capillary Radius”: “11.e-06,”
    “V”: “1828,”
    “emitter”: “Capillary_IL,”
    “Seed_Feed”: “1924418762,”
    “Seed_Emitter”: “2105865363,”
    “Feed: Length”: “1.,”
    “T”: “300,”
    “substrate_emitter”: “Platinum,Channel,”
    “Capillary Radius_std”: “0e-07,”
    “Vmax”: “1900,”
    “CR Limit”: “20.0000,”
    “P-Scale”: “0.023,”
    “independentVariable”: “V,”
    “Tmax”: “350,”
    “Seed_Feed”: “336239948,”
    “Pmax”: “30000,”
    “substrate_feed”: “Silicon,Channel,”
    “feed”: “Cylindrical_Channel,”
    “field”: “Mass Flow,”
    “Boost Voltage”: “0.0,”
    “Pmin”: “1000,”
    “Divergence”: “30.0,”
    “Capillary Length”: “1e-2,”
    “Droplet Energy Loss”: “150,”
    “Tip-to-Extractor Distance”: “5e-3,”
    “P”: “21200,”
    “Ne”: “1,”
    “Feed: Cylindrical Radius”: “50e-6,”
    “Tmin”: “250,”
    “Seed_Emitter”: “1466004254,”
    “propellant”: “EMI-TFSI,Ionic Liquid”
}
```

b. Passively Fed Capillary Array, Ionic Liquid Propellant

```
{
    “Pmax”: “2000,”
    “propellant”: “EMI-BF4,Ionic Liquid,”
    “Vmax”: “850,”
    “Droplet Energy Loss”: “150,”
    “feed”: “Cylindrical_Channel,”
    “Feed: Cylindrical Radius_std”: “0,”
    “Seed_Feed”: “1377741584,”
    “CR_m”: “1.806e-08,”
    “Divergence”: “30.0,”
```

```
    “P-Scale”: “0.023,”
    “Feed: Cylindrical Radius”: “3.95e-06,”
    “Capillary Radius”: “3.95e-06,”
    “P”: “0,”
    “CR Limit”: “3.25,”
    “substrate_feed”: “Silicon,Channel,”
    “Ne”: “127,”
    “emitter”: “Capillary_IL,”
    “Vmin”: “700,”
    “Tmax”: “350,”
    “substrate_emitter”: “Silicon,Channel,”
    “Pmin”: “1000,”
    “Boost Voltage”: “0.0,”
    “Tmin”: “250,”
    “Capillary Length”: “1e-05,”
    “Feed: Length”: “0.0001,”
    “independentVariable”: “V,”
    “field”: “Electric Current,”
    “Capillary Radius_std”: “2.5e-07,”
    “Seed_Emitter”: “976982101,”
    “V”: “1700,”
    “Tip-to-Extractor Distance”: “0.000175,”
    “T”: “300”
}
```

c. Passively Fed Capillary, Liquid Metal Propellant (low Z)

```
{
    “Pmax”: “2000,”
    “Vmax”: “7500,”
    “T”: “450,”
    “feed”: “Cylindrical_Channel,”
    “V”: “1700,”
    “Pmin”: “1000,”
    “Tmin”: “250,”
    “Seed_Emitter”: “1130784501,”
    “Capillary Length”: “0.0001,”
    “field”: “Electric Current,”
    “substrate_emitter”: “Silicon,Channel,”
    “propellant”: “Indium,Liquid Metal,”
    “Ne”: “1,”
    “Boost Voltage”: “0.0,”
    “Capillary Radius_std”: “0.0,”
    “Vmin”: “6500,”
    “emitter”: “Capillary_LM,”
    “substrate_feed”: “Silicon,Channel,”
    “Seed_Feed”: “1919965699,”
    “Tmax”: “350,”
    “Capillary Radius”: “40e-6,”
    “Feed: Cylindrical Radius_std”: “0,”
    “Feed: Length”: “0.0034,”
    “P”: “0,”
    “Feed: Cylindrical Radius”: “35e-6,”
    “Divergence”: “30.0,”
    “independentVariable”: “V,”
    “Tip-to-Extractor Distance”: “0.0007”
}
```

d. Externally Wetted Emitter, Ionic Liquid Propellant

```
{
    “Tmin”: “250,”
    “Droplet Energy Loss”: “0.0,”
    “Polarity”: “Positive,”
    “field”: “Electric Current,”
    “independentVariable”: “V,”
    “Cone Half-Angle”: “14.0,”
    “Pmax”: “2000,”
    “Tip Height_std”: “0.0,”
    “Vmax”: “2200,”
    “Vmin”: “600,”
    “Boost Voltage”: “0.0,”
    “Pmin”: “1000,”
    “Seed_Emitter”: “1130784501,”
    “Seed_Feed”: “1919965699,”
    “emitter”: “External_Cone_IL,”
    “Tip Height”: “0.002,”
    “Feed: Cylindrical Radius_std”: “25e-06,”
    “Cone Base Radius”: “2.8e-6,”
    “Feed: Film Thickness”: “1.e-7,”
    “feed”: “Cylindrical_External,”
    “T”: “300,”
    “P”: “0,”
    “Feed: Groove Radius”: “2e-6,”
    “V”: “1700,”
    “substrate_feed”: “Silicon,Channel,”
    “Feed: Groove Radius_std”: “0.4e-6,”
    “Nspe”: “10,”
    “CR Limit”: “20.0,”
    “substrate_emitter”: “Silicon,Channel,”
    “Cone Radius of Curvature_std”: “0.0,”
    “P-Scale”: “0.023,”
    “CR_m”: “3.806e-08,”
    “Tip-to-Extractor Distance”: “0.0002,”
    “Feed: Cylindrical Radius”: “0.5e-3,”
    “Feed: Number of Grooves”: “4,”
    “Pool Radius”: “0e-06,”
    “propellant”: “EMI-TFSI,Ionic Liquid,”
    “Divergence”: “30.0,”
    “Cone Radius of Curvature”: “0.6e-05,”
    “Feed: Length”: “2.06e-3,”
    “Tmax”: “350,”
    “Cone Base Radius_std”: “1.e-6,”
    “Cone Half-Angle_std”: “0.0,”
    “Ne”: “1000”
}
```

e. Externally Wetted Emitter, Liquid Metal Propellant

```
{
    “Nspe”: “1,”
    “Feed: Length”: “0.00206,”
    “Polarity”: “Positive,”
    “Tip Height_std”: “0.0,”
    “feed”: “Cylindrical_External,”
    “Ne”: “1,”
    “Tip Height”: “0.002,”
```

```
        “Cone Radius of Curvature_std”: “0.0,”
        “T”: “300,”
        “Vmax”: “8000,”
        “Tip-to-Extractor Distance”: “0.001,”
        “Film Thickness”: “0.5e-6,”
        “Cone Half-Angle_std”: “0.0,”
        “Groove Radius_std”: “2e-05,”
        “Boost Voltage”: “0.0,”
        “Droplet Energy Loss”: “0.0,”
        “Divergence”: “30.0,”
        “Cone Half-Angle”: “15.0,”
        “Feed: Film Thickness”: “5e-07,”
        “Tmin”: “250,”
        “propellant”: “Indium,Liquid Metal,”
        “Pmin”: “1000,”
        “Vmin”: “1000,”
        “Number of Grooves”: “1,”
        “substrate_feed”: “Tungsten,Channel,”
        “independentVariable”: “V,”
        “field”: “Efficiency,”
        “P”: “0,”
        “Feed: Cylindrical Radius_std”: “2.5e-05,”
        “substrate_emitter”: “Tungsten,Channel,”
        “Groove Radius”: “2e-05,”
        “Feed: Groove Radius_std”: “4e-07,”
        “Pmax”: “2000,”
        “V”: “1700,”
        “Feed: Groove Radius”: “2e-06,”
        “Cone Radius of Curvature”: “2.25e-6,”
        “Seed_Feed”: “741869103,”
        “Seed_Emitter”: “1646632896,”
        “Tmax”: “350,”
        “Feed: Number of Grooves”: “0,”
        “Feed: Cylindrical Radius”: “0.0005,”
        “emitter”: “External_Cone_LM”
}
```

f. Porous Cone, Ionic Liquid Propellant

```
{
        “emitter”: “Porous_Cone_IL,”
        “Boost Voltage”: “0.0,”
        “V”: “1700,”
        “Seed_Feed”: “50768131,”
        “Cone Half-Angle”: “30.0,”
        “Porosity”: “0.5,”
        “Cone Radius of Curvature”: “1.7e-05,”
        “CR_m”: “5.2e-08,”
        “Pool Radius”: “8e-6,”
        “field”: “Electric Current,”
        “Cone Half-Angle_std”: “0.0,”
        “Divergence”: “30,”
        “Vmin”: “500,”
        “Pmin”: “1000,”
        “substrate_feed”: “Borosilicate Glass P4,Porous,”
        “Tmax”: “350,”
        “Tip-to-Extractor Distance”: “0.00015,”
        “P-Scale”: “0.023,”
        “Pmax”: “2000,”
```

```
        “Cone Radius of Curvature_std”: “0.0,”
        “Seed_Emitter”: “1047404386,”
        “CR Limit”: “20.0,”
        “Pore Radius_std”: “4e-07,”
        “T”: “300,”
        “P”: “0,”
        “Tip Height_std”: “0.0,”
        “Pore Radius”: “0.8e-6,”
        “propellant”: “EMI-TFSI,Ionic Liquid,”
        “Nspe Scale”: “1,”
        “Consider actspe”: “T,”
        “Ne”: “1,”
        “Vmax”: “2200,”
        “substrate_emitter”: “Borosilicate Glass P5,Porous,”
        “Droplet Energy Loss”: “150.0,”
        “Tmin”: “250,”
        “feed”: “Low_Z,”
        “independentVariable”: “V,”
        “Tip Height”: “0.00035,”
        “Polarity”: “Positive”
    }
```

g. Porous Cone, Xerogel, Ionic Liquid Propellant

```
    {
        “Cone Radius of Curvature”: “7e-6,”
        “Tmax”: “350,”
        “Pmax”: “2000,”
        “substrate_feed”: “Xerogel 1,Porous,”
        “Tip Height”: “0.001,”
        “Nspe Scale”: “0.5,”
        “Feed: Cylindrical Radius”: “0.0005,”
        “Vmin”: “1400,”
        “Porosity”: “0.6,”
        “Vmax”: “2200,”
        “P”: “0,”
        “Pore Radius_std”: “1.5e-07,”
        “Seed_Emitter”: “224229373,”
        “feed”: “Cylindrical_Porous,”
        “Pore Radius”: “0.5e-06,”
        “P-Scale”: “1,”
        “Cone Half-Angle_std”: “0.0,”
        “Boost Voltage”: “0.0,”
        “T”: “300,”
        “field”: “Electric Current,”
        “V”: “1700,”
        “emitter”: “Porous_Cone_IL,”
        “Cone Radius of Curvature_std”: “0.0,”
        “Consider actspe”: “F,”
        “Ne”: “1,”
        “Feed: Cylindrical Radius_std”: “1e-06,”
        “Feed: Length”: “0.2,”
        “Tip Height_std”: “0.0,”
        “Pmin”: “1000,”
        “substrate_emitter”: “Xerogel 1,Porous,”
        “Feed: Porosity”: “0.6,”
        “Tmin”: “250,”
        “Tip-to-Extractor Distance”: “0.0005,”
        “independentVariable”: “V,”
```

```
    “Pool Radius”: “2.e-6,”
    “Cone Half-Angle”: “25.0,”
    “Polarity”: “Positive,”
    “Feed: Pore Radius”: “0.5e-6,”
    “CR_m”: “3.806e-08,”
    “Seed_Feed”: “1436393658,”
    “propellant”: “EMI-TFSI,Ionic Liquid,”
    “Droplet Energy Loss”: “150.0,”
    “Divergence”: “30.0,”
    “CR Limit”: “20.”
}
```

h. Porous Cone, Liquid Metal Propellant

```
{
    “V”: “1700,”
    “Vmin”: “2000,”
    “Ne”: “28,”
    “Pmax”: “2000,”
    “Cone Half-Angle_std”: “0.0,”
    “field”: “Efficiency,”
    “Tip Height”: “0.002,”
    “Tmax”: “350,”
    “Cone Radius of Curvature_std”: “0.3e-6,”
    “Nspe”: “1,”
    “Pore Radius”: “0.4e-6,”
    “propellant”: “Indium,Liquid Metal,”
    “Pore Radius_std”: “0.2e-6,”
    “Polarity”: “Positive,”
    “Porosity”: “0.3,”
    “emitter”: “Porous_Cone_LM,”
    “independentVariable”: “V,”
    “Divergence”: “30.0,”
    “Tip-to-Extractor Distance”: “0.003,”
    “T”: “453,”
    “P”: “0,”
    “substrate_feed”: “Tungsten Porous 1,Porous,”
    “Seed_Emitter”: “550832223,”
    “Boost Voltage”: “0.0,”
    “Tmin”: “250,”
    “Pmin”: “1000,”
    “substrate_emitter”: “Tungsten Porous 1,Porous,”
    “Cone Half-Angle”: “6.0,”
    “Tip Height_std”: “0.0,”
    “feed”: “Low_Z,”
    “Vmax”: “15000,”
    “Cone Radius of Curvature”: “2e-06,”
    “Pool Radius”: “.4e-6,”
    “Seed_Feed”: “1567713585”
}
```

i. Porous Edge, Ionic Liquid Propellant

```
{
    “Droplet Energy Loss”: “150,”
    “P-Scale”: “0.023,”
    “Tip-to-Extractor Distance”: “5e-4,”
    “Divergence”: “30.0,”
    “Boost Voltage”: “0.0,”
    “Vmin”: “1000,”
```

```
    “Pmin”: “1000,”
    “Seed_Emitter”: “1007976011,”
    “V”: “1700,”
    “Radius of Curvature_std”: “1.5e-6,”
    “Tip Height”: “0.00035,”
    “Pore Radius”: “0.8e-06,”
    “Radius of Curvature”: “1.5e-05,”
    “Polarity”: “Positive,”
    “feed”: “Low_Z,”
    “Vmax”: “2600,”
    “Porosity”: “0.5,”
    “CR_m”: “5.206e-08,”
    “propellant”: “EMI-TFSI,Ionic Liquid,”
    “Half-Angle_std”: “2,”
    “Ne”: “9,”
    “Edge Length”: “0.007,”
    “Half-Angle”: “30.0,”
    “field”: “Thrust,”
    “substrate_feed”: “Borosilicate Glass P4,Porous,”
    “Pmax”: “2000,”
    “substrate_emitter”: “Borosilicate Glass P5,Porous,”
    “Nspe Scale”: “1,”
    “emitter”: “Porous_Edge_IL,”
    “Tip Height_std”: “0.0,”
    “CR Limit”: “20,”
    “Tmax”: “350,”
    “Pool Radius”: “0.8e-5,”
    “Seed_Feed”: “919996105,”
    “T”: “300,”
    “Tmin”: “250,”
    “Pore Radius_std”: “0.2e-6,”
    “independentVariable”: “V,”
    “P”: “0”
}
```